UC Berkeley
UC Berkeley Electronic Theses and Dissertations

Title
Mechanical regulation of cell shape by actomyosin stress fibers

Permalink
https://escholarship.org/uc/item/2js5n19q

Author
Lee, Stacey

Publication Date
2019

Peer reviewed|Thesis/dissertation

Mechanical regulation of cell shape by actomyosin stress fibers

by

Stacey Lee

A dissertation submitted in partial satisfaction of the

requirements for the degree of

Joint Doctor of Philosophy

with University of California, San Francisco

in

Bioengineering

in the

Graduate Division

of the

University of California, Berkeley

Committee in charge:

Professor Sanjay Kumar, Chair

Professor Lani Wu

Professor David G. Drubin

Spring 2019

Mechanical regulation of cell shape by actomyosin stress fibers

Copyright © 2019

By: Stacey Lee

Abstract

Mechanical regulation of cell shape by actomyosin stress fibers

by

Stacey Lee

Joint Doctor of Philosophy in Bioengineering
with University of California, San Francisco

University of California, Berkeley

Professor Sanjay Kumar, Chair

Cell migration is a key process underlying embryogenesis, wound healing, and cancer progression. The actomyosin stress fiber (SF) network enables mechanosensing of the extracellular matrix (ECM) environment by generating forces to probe substrate stiffness, topography, and adhesive properties, which in turn, collectively influence SF organization. Migrating cells actively rearrange three SF subtypes—dorsal SFs, transverse arcs, and ventral SFs (including apical SFs and basal SFs)—to maintain a polarized shape needed for directional movement. There have been several efforts to dissect contributions of specific SF subtypes in generating and maintaining tension, which have produced important new insights into the field's understanding of SF subtype function. However, they remain indirect measures of SF mechanical properties. Furthermore, many of these studies were conducted on cells cultured on flat, rigid substrates which do not recapitulate many of the salient features of the complex microenvironments found in vivo.

In this dissertation, we seek to understand how cells regulate tension in their SF network during polarization and migration, and how substrate geometry influences SF organization. Using laser nanosurgery, we systematically sever single SFs belonging to each subtype in order to measure their retraction kinetics. We find that SF subtypes are arranged in a mechanically integrated network and that SF subtypes have distinct mechanical properties that are dependent on intrinsic structure, external connections to other SFs, and formation history. Next, we examine the role of cofilin in remodeling the SF network during polarization, the first step in directed cell migration. We find that cofilin remodels SF tension by facilitating the fusion of thin, weakly contractile SFs into thicker, more contractile structures that break tensional symmetry and enable front-back polarization. Finally, we explore the influence of substrate curvature on SF network organization and mechanics. Apical and basal SFs are oriented perpendicular to one another, and bear different amounts of prestress, suggesting that they each have distinct roles in shaping the cell.

In summary, this dissertation systematically examines the mechanical contributions of SF subtypes to determining cell shape and establishing tensional asymmetry in the cell. We also examine the influence of substrate topography and adhesive patterns on cell shape and SF tension, which are important in understanding how cells interact with ECMs that vary in topography and adhesion. These findings enhance our understanding of how cells mechanically organize their SF network to build a contractile, integrated network for migration.

Table of Contents

Acknowledgements

There are numerous people whose support was invaluable in maintaining my excitement for science, but more importantly, for keeping me grounded as I spent the better part of the past six years immersed in the lab.

First, I would like to thank my advisor, Professor Sanjay Kumar, for his patience and guidance throughout the past six years. He always remained optimistic, provided general advice, and also very specific troubleshooting help, all of which gave me enough momentum to make it over the rough patches and complete my projects. In addition to technical lab advice, Sanjay was also instrumental in my training as a scientist: he spent untold hours critically reviewing and editing my fellowship applications and manuscripts, which not only improved my technical writing, but also developed my abilities to ask and subsequently answer pointed questions.

Additionally, the other members of my dissertation committee, Professor Lani Wu and Professor David Drubin, and the members of my qualifying exam committee, Professor Mohammad Mofrad, Professor Gerard Marriott, Professor Bo Huang, and Professor Ahmet Yildiz, graciously provided their expertise and time. Their feedback helped to improve the quality and impact of my work.

My colleagues, the postdocs and graduate students in the lab whom I worked with and around on a day-to-day basis, provided scientific feedback and camaraderie. Elena Kassianidou mentored me when I was a rotation student and gave very helpful guidance over the next three years in the lab where we commiserated over our ablation and micropatterning woes and celebrated the small victories. I would also like to thank Ching-Wei Chang for his advice early on in my PhD. Other colleagues, including Jess Lee, Mike Kang, George Lin, Jasmine Hughes, Joe Chen, Kayla Wolf, Phil Kang, Ruoxing Lei, Andy Lopez, Kelsey Springer, Carmela Rianna, Jason Coombes, Badri Ananthanarayanan, Sophie Wong and Yushan Kim, gave helpful feedback and provided much-needed distractions from the rigors of the lab, through countless lunches, happy hours, and social outings.

Throughout my PhD, I also had the opportunity to work with a number of scientists outside of the lab. I would like to thank Professor Carlos Ortiz de Solorzano, Professor Manos Mavrakis, and Professor Tilman Schaeffer for their technical advice and time spent discussing my projects. I would also like to thank Professor Richard Assoian, Professor Kathleen Stebe, and Caroline Cameron for their help in the development and execution of my project working on substrate curvature and cell shape. I also worked with Professor Nicole King and Ben Larson, whose work studying choanoflagellate development provided me with a different perspective on biophysics. Finally, I had the opportunity to train junior scientists: Bioengineering rotation students Erin Akins and Maria Diaz de Leon Derby, and undergraduate Preethi Bhat, who all diligently and patiently carried out their experiments as I was trying to figure out how to be an effective mentor.

Past mentors, Professor Ge Yang, Dr. Darryl Sasaki, Minhua Qiu, and Yiyi Yu, were instrumental in training me as a young scientist. Professor Yang and Dr. Sasaki took a chance by inviting me to work in their labs as an undergraduate research student, encouraged me to pursue

Chapter 1. Actomyosin stress fiber mechanosensing in 2D and 3D

1.1 Abstract

Mechanotransduction is the process through which cells survey the mechanical properties of their environment, convert these mechanical inputs into biochemical signals, and modulate their phenotype in response. These mechanical inputs, which may be encoded in the form of extracellular matrix stiffness, dimensionality, and adhesion, all strongly influence cell morphology, migration, and fate decisions. One mechanism through which cells on planar or pseudo-planar matrices exert tensile forces and interrogate microenvironmental mechanics is through stress fibers, which are bundles composed of actin filaments and, in most cases, non-muscle myosin II filaments. Stress fibers form a continuous structural network that is mechanically coupled to the extracellular matrix through focal adhesions. Furthermore, myosin-driven contractility plays a central role in the ability of stress fibers to sense matrix mechanics and generate tension. Here, we review the distinct roles that non-muscle myosin II plays in driving mechanosensing and focus specifically on motility. In a closely related discussion, we also describe stress fiber classification schemes and the differing roles of various myosin isoforms in each category. Finally, we briefly highlight recent studies exploring mechanosensing in three-dimensional environments, in which matrix content, structure, and mechanics are often tightly interrelated. Stress fibers and the myosin motors therein represent an intriguing and functionally important biological system in which mechanics, biochemistry, and architecture all converge.

1.2 Introduction

The extracellular matrix (ECM) is a critical regulator of cell and tissue function. Properties of the ECM, including stiffness, topography, and ligand type and density, have all been shown to regulate cell shape, migration, and fate (1,2). For example, matrix stiffness influences the differentiation of mesenchymal and neural stem cells into different lineages (3–5). Substrate topography and stiffness can both direct cell migration and growth (6–8). To effectively probe the properties of the ECM, the cell exerts forces on the environment and gauges the response in a controlled feedback loop that is broadly termed "mechanosensing".

The cell has specialized machinery for ECM mechanosensing, including motor proteins, cytoskeletal proteins, and force-sensitive proteins that change conformation or activity (or both) in response to applied forces at focal adhesions (FAs), which are protein complexes that directly bind to ECM proteins through integrins and other ECM adhesion receptors (9–11). In one important mode of mechanosensing, the cell uses stress fibers (SFs), which are bundles of 10 to 30 actin filaments (12) (although some thicker SFs may contain up to ten times as many filaments) cross-linked by proteins, including α-actinin. Some SFs also contain non-muscle

myosin II (hereafter referred to as MII), which lends contractile properties to the SF and enables the cell to survey ECM physical properties, define cell shape, and facilitate migration. This review will focus on recent advances in SF-based mechanosensing in both two-dimensional (2D) and three-dimensional (3D) environments.

1.3 Myosin structure and regulation

MII has two important roles in SFs: (1) cross-linking antiparallel actin filaments and (2) generating the power stroke to translocate these filaments to contract the SF. MII is a hexameric protein complex composed of two myosin heavy chains, two essential light chains, and two regulatory light chains (RLCs) (Fig. 1.1a). The heavy chains contain a helical tail domain and a globular head domain, which can bind to actin filaments and ATP (13). Myosin complexes can further organize into bipolar filaments, with the tails in an antiparallel orientation and the actin-bound heads in opposing directions (Fig. 1.1b). Polarized actin filaments are composed of actin monomers, which are polymerized onto the barbed (plus) end of an existing filament. To contract the filament, myosin heads hydrolyze ATP to generate rotation of the myosin head toward the plus end of actin, leading to the subsequent translocation of antiparallel actin filaments (14).
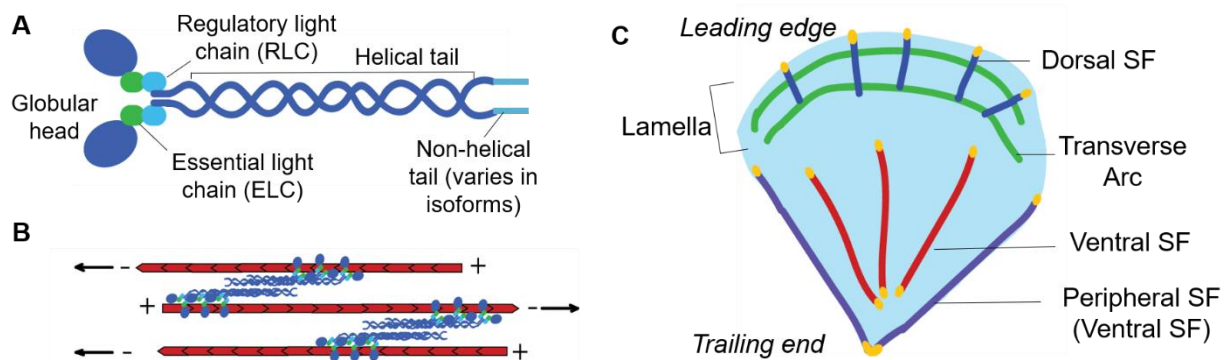
Figure 1.1. Actomyosin SFs in cells. (a) Myosin is composed of two heavy chains, each consisting of a globular head and a tail, two essential light chains, and two regulatory light chains. The non-helical tail region varies in the three isoforms. (b) Myosin heads bind to actin filaments. ATP hydrolysis leads to a conformational change in the head and neck region, which results in mechanical movement of the myosin head toward the plus end of actin and in movement of the actin filament in the opposite direction (indicated by arrows). (c) SFs can be divided into three populations as defined by their anteroposterior position within a migrating cell and connection to focal adhesions.

Actomyosin contractility is strongly regulated by phosphorylation of the RLC at Ser19 and Thr18. Ca^{2+}-activated myosin light chain kinase (MLCK) and zipper-interacting protein kinase both phosphorylate the RLCs (15–18). Additionally, Rho-GTPase effectors, including RhoA-activated Rho-associated kinase (ROCK) and p21-associated kinase (PAK), phosphorylate the RLCs(14,18,19). ROCK can also reduce RLC dephosphorylation via inhibition of myosin light chain phosphatase activity (14). Phosphorylation of Ser19 leads to an increase in Mg^{2+}-ATPase activity that powers the MII head sliding along actin filaments and FA maturation (15,17,20). Additional phosphorylation at Thr18 increases this activity and results in the clustering of

actomyosin filaments into thick SFs (16,20,21). The differential mechanical consequences of mono- versus di-phosphorylation remain an area of active study.

Three myosin isoforms—MIIA, MIIB, and MIIC—have been identified in mammalian cells, differing in their heavy chains. Expression of the three isoforms is not universal in cells. MIIA and MIIB are the predominant isoforms expressed in cultured cells, whereas MIIC is found in a more restricted subset of cells, including neural cells and breast and lung cancer cells(14,22). In recently spread cells that have not yet established polarity, MIIA and MIIB uniformly co-assemble on the same SF (23,24). Over time, as the cell becomes increasingly polarized, the leading edge becomes enriched in MIIA and the trailing end in MIIB (25–27). Although SFs throughout the cell typically contain both MII isoforms, the ratio of MIIA to MIIB is higher in SFs near the leading edge but decreases as SFs undergo retrograde flow during cytoskeletal remodeling (23,28,29). This is likely due to a sorting mechanism driven by the different kinetics and heavy chains of the isoforms (23). MIIA has a higher turnover rate and spends less time bound to actin compared with MIIB(30,31). As SFs move in a retrograde manner, a higher proportion of MIIA unbinds from the fiber, which in turn enriches the SF in MIIB. Myosin chimeras consisting of swapped C-terminal tails reversed the localization of the isoforms (32). These findings are consistent with the presumed differential functions of MIIA and MIIB. Rac1 promotes leading edge formation by generating a flat lamella and recruiting MIIA to the leading edge, where it quickly hydrolyzes ATP to form new, short-lived SFs (30,33). MIIA also stabilizes adhesions and facilitates traction force generation at the leading edge (34). On the other hand, MIIB has a slower ATP hydrolysis rate but a higher duty ratio, meaning that it spends more time bound to actin in its force-generating state, thereby generating higher force per ATP hydrolyzed (31). This is important in stabilizing SFs, generating traction forces at the trailing edge, and maintaining the front-back polarity needed for directed migration (23–26,35,36). Furthermore, MIIB is enriched in the perinuclear SFs where it compresses the cell nucleus to enable efficient cell migration and invasion through confined spaces(37,38). MIIC is less well characterized; it is present in tumor cells and neural cells where it contributes to cytokinesis and neurite growth, respectively (22,39,40).

1.4 Formation of contractile actomyosin bundles

To determine the minimal requirements for forming SFs, some have employed well-defined reconstituted systems consisting of purified filamentous actin and myosin to study the organization of actin and myosin into contractile bundles. Protein-level cues, including myosin concentration and actin polarity, guide the self-assembly and organization of myosin and actin filaments into contractile bundles which are the building blocks of the tensed, interconnected SF network (41–44). Analogous to the actomyosin bundles of differing actin polarities that form in reconstituted systems, SFs that vary in actin polarity have been observed in mammalian cells. Three populations of SFs—uniform polarity, graded polarity, and alternating polarity bundles, correlating with the intracellular location of the bundles—were first documented in migrating primary chick fibroblasts (12). Uniform polarity bundles were observed near the cell front, and alternating polarity bundles were observed at the cell rear. Graded polarity bundles, in which the degree of polarity depended on the distance from the bundle ends, were located in the center of the cell (12).

Recently, careful observation of SF dynamics in migrating U2OS osteosarcoma cells has given rise to a more general classification system for SFs on the basis of their different formation pathways, molecular composition, and connection to FAs (Fig. 1.1c) (45,46). Dorsal SFs are found at the lamella and have uniform actin polarity which is due to inverted formin 2 or vasodilator-stimulated phosphoprotein (VASP) (or both) promoting actin polymerization at the barbed end (closest to the FA) of dorsal SFs (45–48). Furthermore, they are often found to lack MII, implying that dorsal SFs are not contractile (28,46,49). This subpopulation is connected at one end to an FA, and the other end rises toward the dorsal membrane surface. Dorsal SFs are mechanically coupled to the second subpopulation, transverse arcs. Transverse arcs are curved SFs exhibiting alternating actin polarity and are found near the dorsal membrane surface of the lamella (45). They are formed by the end-to-end annealing of Arp2/3-nucleated actin filaments and are not connected directly to FAs (46,50). Transverse arc contraction, largely driven by MIIA activity, exerts a force on dorsal SFs in the retrograde direction. As dorsal SFs are anchored to the ECM via a stable FA, transverse arc contraction pulls dorsal SFs and the lamella membrane down (28). The third subpopulation, ventral SFs, run along the matrix-bound face of the cell, become increasingly prominent toward the cell rear, and are connected at both ends to FAs. A subset of ventral SFs is produced from the myosin-mediated fusion of a transverse arc with two dorsal SFs(46,48). Yet another classification system for SFs distinguishes between peripherally located SFs and centrally located SFs (29,51–54). This scheme is motivated in part by the recognition that peripheral SFs (sometimes called peripheral arcs) can drive or reflect (or both) cortical surface tension and that peripheral and central SFs can bear different mechanical loads (54–56).

The primary chick fibroblast SF classification system can perhaps be reconciled with the U2OS SF classification system. The uniform polarity bundles and alternating polarity bundles correspond to dorsal and ventral SFs, respectively. The graded polarity bundles correspond to the transverse arcs fusing with dorsal SFs on either side during retrograde flow (46). The degree of polarity corresponds to the location of the SF within a migrating cell. At the lamella, SFs undergoing active and directed polymerization have uniform polarity in order to stabilize the protrusion of the leading edge. As the SFs move toward the trailing edge of the cell, SFs adopt an alternating polarity, indicating that their primary role is to generate contractile forces to maintain cell shape and traction. Peripheral SFs can be classified as ventral SFs (or multiple ventral SFs bundled together), and central SFs can broadly encompass dorsal SFs, transverse arcs, and ventral SFs.

It is important to note that the dorsal/transverse arc/ventral SF was originally developed for mesenchymally migrating cells and that the uniform/graded/alternating polarity system was based on observations in primary chick fibroblasts. The peripheral/central SF classification scheme is the most general and is applicable to many cells. Not all cell types exhibit the dorsal/transverse arc/ventral SF subpopulations, and even within the same population of cells, there may be variability in the representation of each of the SF subpopulations (28,45,46). Stationary cells often exhibit only ventral SFs, indicating that one of the primary roles of dorsal SFs and transverse arcs is to drive leading edge protrusion during migration. The varying degrees of SF representation raises the question of how different ECM cues, including stiffness, ligand presentation, and dimensionality, collectively influence SF subpopulation formation and organization. Furthermore, there are other questions pertaining to the how SF subpopulations

interact to form an interconnected network. For example, transverse arc-dorsal SF junctions are not well characterized at the molecular scale but are likely enriched in actin cross-linking proteins that promote force transmission by tightly coupling dorsal SFs to transverse arcs. These areas are currently under active investigation.

1.5 Stress fiber-based mechanosensing

It is widely appreciated that MII tenses SFs to different degrees in cells. Measurements of the tensile properties of actomyosin bundles have been carried out on reconstituted actomyosin systems or isolated SF networks where all other cell components are removed (57). In these simplified systems, SFs can be manipulated to measure their biophysical properties by using tools, including microcantilevers (58). However, these methods are not amenable to live cells. Thus, to study SFs in live cells, some have used outside-in perturbations to measure mechanical properties of SFs, including nanoindentation and whole-cell stretching (59,60). Others have used inside-out methods such as pharmacological treatment or genetic perturbations to manipulate SF architecture and tension and measure the resulting changes in the ability of the cell to exert traction on the ECM (50,51,61,62). However, with these methods, it is not possible to tease out the mechanical contributions of individual SFs and to examine how they contribute to the overall contractility of the cell.

Thus, our group (52,63) and others (52,63) have used femtosecond laser nanosurgery to sever single SFs to directly measure the mechanical properties, including contractility, of SFs within living cells and confirmed the presumed cross-linking and contractility roles of MII. When ventral SFs are severed, the cut ends retract in a viscoelastic manner which is largely mediated by MII (52,53). MII cross-linking imparts viscous resistance to retraction of a severed SF, as deletion of the actin-binding myosin head speeds SF retraction (29). At the same time, MII activity contributes to SF elasticity by tensing actin filaments. The retraction kinetics of SFs differ based on the location of the SF: peripheral SFs retract a longer distance and a lower effective elasticity (longer time constant) compared with centrally located SFs, indicating that peripheral SFs are tensed to a greater degree (53). These differences may be associated with the spatially compartmentalized control of myosin RLC kinases. Peripheral SFs are preferentially regulated by MLCK, and central SFs by ROCK, as pharmacological inhibition of the kinases using ML-7 (MLCK) or Y-27623 (ROCK) affected the retraction kinetics and morphology of the respective populations (51,64). Some studies suggest that the ratio of MIIA to MIIB isoforms on a particular SF can affect its mechanical properties and that ROCK preferentially regulates MIIA activity whereas MLCK preferentially regulates MIIB (29,32,65). These findings may be placed in the context of the different mechanochemical properties of MIIA and MIIB. In particular, ROCK-controlled SFs may be enriched in fast ATP-hydrolyzing MIIA, which facilitates the rapid and dynamic SF contraction and evolution in the lamella. MLCK-controlled peripheral SFs may be enriched in high-duty ratio MIIB to support the stable SFs found at stable cell edges. However, additional studies are needed to test these hypothetical associations in a clear and direct way and to examine the differential mechanics of the various SF subpopulations. It would be particularly interesting and important to relate the changes in SF composition and regulation in specific cellular compartments to mechanical functions.

Traction force generation by stress fibers

MII plays a critical role in sensing mechanical properties of the ECM, including stiffness, by exerting traction stresses on the substrate (1,9,66,67). On softer substrates, FAs are smaller and SFs are less abundant as cells are unable to generate sufficient traction that would otherwise reinforce adhesions (66,68,69). The diminished traction forces can restrict cell spreading and migration and in some cases are associated with reduced proliferation (7,8,68,69). In contrast, cells are able to generate large traction stresses on stiff substrates, which enable them to spread and form mature FAs (66,67). The differences in morphology between cells cultured on compliant and non-compliant substrates are understood to be MII-mediated, because cells lose their characteristic stiffness-dependent differences with abrogation of myosin-based contractility (8,70). Although this review focuses on MII, there are also several other classes of myosin motors whose roles in mechanosensing are under investigation. These myosin motors typically bridge actin filaments to other proteins. For example, myosin X, which links actin to membrane proteins, is critical in the formation of filopodia, thin actin protrusions that participate in ECM remodeling (71–73). In turn, filopodia may contribute to the formation of dorsal SFs (74). Future experiments should uncover the roles of other myosin motors in mechanosensing.

Within a given cell, different pools of SFs appear to exert different levels of traction. Although this idea is still being systematically explored, computational analysis of experimental data offers important clues. For example, model-based traction force microscopy infers tension held in SFs by iteratively matching traction maps and images of SFs and FAs with cable network models of the actin cytoskeleton (75). These measurements reveal that individual ventral SFs exert the highest traction forces and dorsal SFs the lowest (75). More conventional TFM studies suggest that dorsal SFs are more important for templating the location of adhesions and rely upon MII activity in the cortical actin cytoskeleton (for example, transverse arcs) to drive force-dependent FA growth(61). Interestingly, although the traction force per dorsal SF is relatively low, the lamellipodium, which lacks defined SFs, can generate very high traction forces that seem to be largely driven by cortical MII activity (76,77). SF-generated traction likely becomes more important in generating traction forces and defining cell shape in areas further away from the lamellipodium. Dorsal SFs, which are found behind the lamellipodium, directly interact with FAs but can neither generate contractile forces nor exert traction on their own since they lack MII. Instead, they exert low traction forces indirectly through transverse arc contractility. Ventral SFs, are the predominant SF type in non-migrating cells, which by definition lack front-back polarity. They are under higher tension and generate higher traction forces than either dorsal SFs or transverse arcs (75). Peripherally located ventral SFs collectively exert higher traction stresses compared with centrally located ventral SFs (52,54).

Individual tensed SFs are networked together to form a dynamic system that can readily redistribute tension (54). Femtosecond laser nanosurgery is a powerful tool that can be used to obtain mechanical properties of selected SFs and their role in maintaining tension redistribution. For example, a single SF can be severed to elucidate its structural role in the cytoskeleton by examining changes in SF morphology in the surrounding network. Combining this technique with molecular readouts, such as Förster resonance energy transfer (FRET) tension sensors (for example, based on vinculin (78), talin (79), or α-actinin (80)), may provide insight into how tension released from a single SF is balanced by the surrounding cytoskeletal network.

Mechanosensing through a molecular clutch

Mechanosensing by MII pulling on FA-anchored SFs has been described by the motor-clutch model. In this model, MII and FAs respectively act as a cellular motor and clutch mechanism that can probe substrate stiffness and direct actin polymerization (9). Spreading cells initiate stiffness sensing by locally tensing the substrate through sarcomeric units consisting of a myosin minifilament (comprised of about 28 myosins arranged in a bipolar fashion) cross-linked to two actin filaments which in turn are connected to nascent focal complexes (81). The ECM stiffness value correlates with the number of steps the MII motors take (roughly 2.5 nm per step) before the actin filaments reach a force threshold required to recruit proteins to reinforce and stabilize the adhesion (81). Stiff substrates require fewer myosin minifilament steps to recruit and promote nascent adhesions into stable FAs (81). These adhesions then associate with SFs and are integrated into the cytoskeletal network, which results in increased tension on the adhesion. These forces unfold mechanically sensitive FA proteins (including talin and vinculin) and, in a positive feedback loop, initiate signaling cascades that produce thicker and highly tensile SFs (10,82–84). During this process, frictional slippage occurs, whereby actin moves relative to the stationary FA (9). Conversely, on more compliant substrates, the myosin minifilaments within a sarcomeric unit are required to take a larger number of steps to reach a force threshold. Load-and-fail dynamics, where the ECM-coupled nascent adhesion moves with the actin filament until a failure point is reached and the adhesion detaches from the ECM, may also be observed (9,11,85–88). In this regime, the rate of integrin disengagement from fibronectin, an ECM ligand, is faster than the rate of talin unfolding, which precludes vinculin binding and FA reinforcement (10). This results in cells with thinner SFs (or no SFs at all) and cells with smaller projected areas (68,89,90).

The cytoskeleton undergoes continuous remodeling in response to changes in the environment. When an SF is under tension, VASP is phosphorylated along the SF, leading to increased contractility and a cessation of actin polymerization at the FAs (48). It is conceivable that a sarcomeric force-sensing mechanism similar to the one described above at the cell-ECM interface also exists along the length of SFs. That is, on stiff substrates, MII minifilaments would need to take a small number of steps along filaments to reach a threshold force. Increasingly stiff substrates favor the addition of sarcomeric units along the length of the fiber which incrementally lengthens the SF. This suggests that longer SFs with more sarcomeric units bear more tension. On the other hand, when an SF is no longer under a threshold tension, VASP is not phosphorylated and the SF is targeted for disassembly by cofilin (48). These two mechanosensitive mechanisms provide a mechanism for stiffness sensing and durotaxis at the FA and SF: nascent adhesions or SFs that are not under a threshold tension are disassembled, leaving behind stable SFs and adhesions.

MII activity and the ability to sense stiffness cues in the environment mediate various aspects of tumor progression, including dysplasia, tissue invasion, and metastasis (19). When manipulated in culture, matrix stiffness and ligand density both affect the ability of cells to migrate, and migration speed is maximized at intermediate levels of both (91). These biphasic relationships have been successfully explained by using models that involve myosin-based mechanosensing (92,93). Furthermore, the orientation of matrix proteins, including collagen and fibronectin, determines the ability of cells to effectively engage with the ECM during mechanosensing (94–96). Aberrant mechanosensing has been implicated in the pathogenesis of diseases involving cell

migration through tissue, including the invasive brain tumor glioblastoma (GBM). Whereas soft matrices reduce the migration of GBM cell lines in a MII-dependent fashion (8), primary GBM tumor-initiating cells spread, migrate, and proliferate even on very compliant matrices (97). Increasing myosin contractility through pharmacological or genetic manipulation restores the expected loss of motility, spreading, and proliferation on compliant substrates and dramatically reduces invasion *in vivo* (97). Interestingly, myosin activation has also been observed to facilitate GBM cell translocation through tight intercellular spaces within the brain (37). Future studies should uncover how the reported *in vitro* roles of MII can be translated into disease microenvironments.

1.6 Actomyosin contractility in three dimensions

Most studies of myosin-mediated SF regulation of cell shape have been conducted in cells cultured on idealized 2D substrates with the basal side interacting with the ECM-coated surface and the dorsal side free. Many of these studies highlighted above focused on one aspect of the microenvironment, such as adhesivity or stiffness, whereas the *in vivo* microenvironment, which is often 3D, can vary in pore/mesh size, degradability, geometry, stiffness, and protein composition. Recent efforts have focused on better understanding the role of complex matrices that are more representative of the *in vivo* conditions such as interfacial 2D and fully 3D environments. For example, during invasive migration along a blood vessel-ECM interface, tumor cells interact with blood vessels on the basal surface and ECM proteins on their dorsal surface (98,99). In fully 3D environments, cells are often embedded in a meshwork of ECM proteins (for example, collagen) and may interact with several fibers in different planes. The additional dimension introduces another degree of freedom that can significantly alter migration and cell shape from a slowly migrating, lamellipodial shape to a fast migrating, elongated shape (100). The role and existence of SFs *in vivo* have been controversial, as they are sometimes assumed to be an artifact of 2D culture (101,102). However, recent publications indicate that contractile SFs are important *in vivo* in processes as varied as wound closure, embryonic epithelial sheet closure, and duct contraction(103). Cells also form SFs in 3D matrices consisting of thick collagen bundles (62,104). It is unclear whether 3D SFs, which are often thinner and more difficult to visualize using conventional confocal microscopy techniques, can also be described by the dorsal/transverse arc/ventral SF classification scheme for 2D cultures. Super-resolution imaging and femtosecond laser ablation may be used to better understand the structure, composition, and mechanical properties of these 3D SFs.

Engineered microenvironments to study mechanotransduction in three-dimensions
To better understand the roles of actomyosin contractility and migration in complex systems and to compare the roles in 2D environments, researchers have used different culture systems to replicate *in vivo* conditions. To mimic interfacial migration, we (98,105) and others (98,105) have developed 2.5D sandwich systems that confine cells between a planar base substrate and an ECM or hydrogel layer. In these systems, cell migration is slower and morphology becomes elongated with no lamellipodia, in the case of GBM cells (98). This is attributed to the ECM overlay, which promotes the formation of additional adhesions on the dorsal surface. MII inhibition prevents the formation of strong adhesions to both surfaces and thus enables the cell to migrate faster (98).

Others have also embedded cells in collagen matrices to mimic 3D ECM environments. At the macroscale, collagen forms a soft gel with a 1kPa Young's modulus which is very different from the microscale structure consisting of long fibers with megapascal-scale Young's modulus (measured from the long axis) that single cells effectively sense (104). As in the sandwich cultures, cells adopt an elongated spindle morphology in these matrices and align their adhesions and SFs along collagen fibers (94,98,104). The local fiber architecture is critical in determining adhesion size and ultimately the magnitude of traction forces that the cell can exert (Fig. 1.2) (94). Collagen has a megapascal-scale tensile strength along the long axis but a much smaller stiffness if measured in the normal direction. Thus, FA area is larger if cell-generated forces are applied parallel to the fiber and smaller if applied normally (94,106).
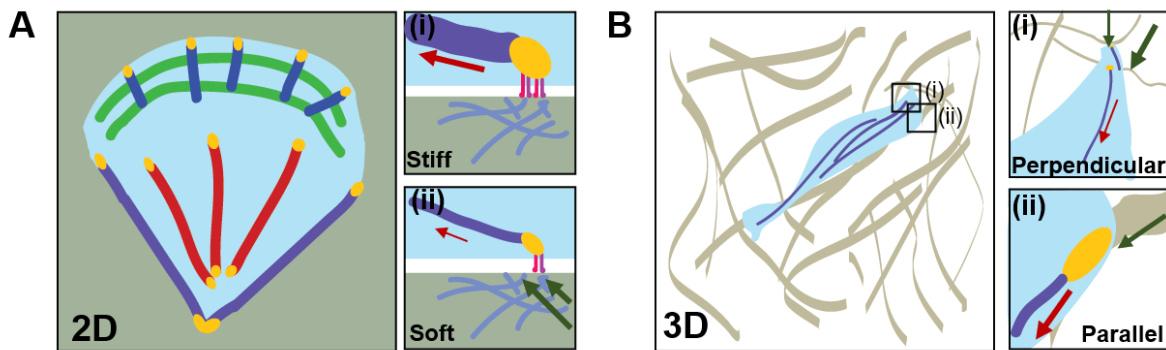

Figure 1.2. SF architecture and cell morphology differ in two-dimensional and three-dimensional matrices. (a) Migrating cells on two-dimensional matrices have a broad, flat leading edge and a pointed trailing end. Dorsal SFs are in blue, transverse arcs in green, ventral SFs in red, and peripheral SFs in purple. Focal adhesions are in yellow. (i) Stiff substrates are able to resist deformation by cell-generated forces (red arrow). This results in focal adhesion maturation and reinforcement of SFs. (ii) Soft substrates deform (green arrows) under cell-generated forces and move with the applied force. Focal adhesions are smaller and SFs are thinner. (b) In three-dimensional collagen matrices, cells adopt an elongated morphology. Collagen fibers have high tensile strength but low resistance to bending. (i) Fibers oriented normally to the cell-generated force (red arrow) readily deform (green arrows). (ii) Fibers oriented parallel to the applied force (red arrow) are tensed (green arrow) and support the formation of mature adhesions and SFs.

Given that collagen microarchitecture varies in stiffness and pore size, we (93,107) and others (38,108) have engineered well-defined matrices to decouple these two parameters (109). We developed a polyacrylamide microchannel platform in which substrate stiffness and confinement can be independently varied. In these environments, cells in stiff, thin-width microchannels form SFs along the channel walls and migrate faster compared with those in soft, wider channels (93,107). The effects of stiff, thin-width channels on cell morphology and migration speed are consistent with those observed in collagen matrices. Others have also fabricated microfluidic devices featuring constrictions of varying widths and found that MIIB is responsible for squeezing the rigid nucleus through these environments (38,108). Others used thin-width, high-aspect ratio patterned fibronectin strips to examine the effects of topography and ligand density on migration and morphology. These "1D" photopatterned strips are reminiscent of the thin fibrillar collagen tracks that cells migrate along in the 3D collagen matrices. In contrast to cells on 2D substrates, cells cultured on the 1D systems have elongated spindle morphologies and fast migration speeds similar to those observed in fibrillar 3D matrices (100). Furthermore, unlike in 2D, where the correlation between migration speed and ligand density is biphasic, migration speed is independent of ligand density in 1D (100).

Efforts to understand the differential roles of MII isoforms in non-2D systems have also yielded surprising results. MIIA is required to stabilize adhesions and form a flat lamella in 2D and is also required for FA maturation at the leading edge of cells in 1D photopatterned ECMs (28,34,110). MIIB is required to stabilize mature adhesions further back from the leading edge (25,27,110). However, inhibition of MII activity has different effects on cells in 2D and 3D. In 2D, genetic ablation of MIIA or pharmacological inhibition of MII activity increases mesenchymal migration speeds, whereas in 3D, migration is abrogated (34,104,110,111). This effect is likely due to differences in migration modes: 2D mesenchymal migration is a slow process that is dependent on the formation and maturation of adhesions. Inhibition of MII increases migration speeds by increasing FA turnover and preventing their maturation which impedes efficient migration (98). There is also a possibility that MII inhibition increases the actin monomer pool (which would otherwise be incorporated into thick SFs) at the leading edge, allowing actin polymerization to promote leading edge protrusion for migration. In contrast, in 3D, MII inhibition effectively abrogates migration since actomyosin contractility is needed to break the high levels of integrin clustering that are found in 3D matrices (104). Migration by actin polymerization-driven leading edge protrusion is limited since the discontinuous fibers are much smaller in area compared with the 2D case.

1.7 Outlook

In vivo, the ECM is highly complex and variable in stiffness, dimensionality, and ligand presentation. These different combinations of matrix properties may influence cell behavior in complex and unpredictable ways that are challenging to deduce from studies in which single properties are varied in isolation. Although it seems clear that MII-mediated actomyosin contractility within SFs plays crucial roles in mechanosensing in 2D culture, the field is still grappling with the translation of these relationships to more complex microenvironments representative of tissue. Thus, an important objective going forward will be to characterize these relationships, which will surely be facilitated by developing more sophisticated culture paradigms.

1.8 Acknowledgments

Chapter 2. Actomyosin stress fiber subtypes have unique viscoelastic properties and roles in tension generation

Highlights: We use femtosecond laser ablation to examine the mechanical properties of stress fiber (SF) subtypes. By measuring the recoil of individual SFs in control cells or in cells depleted of a specific subtype, we find that each subtype has distinct retraction kinetics, which are in turn highly interdependent.

2.1 Abstract

Actomyosin stress fibers (SFs) support cell shape and migration by directing intracellular tension to the extracellular matrix (ECM) via focal adhesions. Migrating cells exhibit three SF subtypes (dorsal SFs, transverse arcs, and ventral SFs), which differ in their origin, location, and ECM connectivity. While each subtype is hypothesized to play unique structural roles, this idea has not been directly tested at the single-SF level. Here, we interrogate the mechanical properties of single SFs of each subtype based on their retraction kinetics following laser incision. While each SF subtype bears distinct mechanical properties, these properties are highly interdependent, with incision of dorsal fibers producing centripetal recoil of adjacent transverse arcs and the retraction of incised transverse arcs being limited by attachment points to dorsal SFs. These observations hold whether cells are allowed to spread freely or confined to crossbow ECM patterns. Consistent with this interdependence, subtype-specific knockdown of dorsal SFs (palladin) or transverse arcs (mDia2) influences ventral SF retraction. These altered mechanics are partially phenocopied in cells cultured on ECM microlines that preclude assembly of dorsal SFs and transverse arcs. Our findings directly demonstrate that different SF subtypes play distinct roles in generating tension and form a mechanically interdependent network.

2.2 Introduction

Cell migration is a critical process in embryogenesis, wound healing, and cancer progression (112,113). The actomyosin network plays important roles in maintaining a polarized cell shape during migration and mechanosensing by dynamically remodeling and by coordinating the generation and release of tension (114). Cells can generate these tensile forces by assembling stress fibers (SF), which are actin-based bundles that frequently contain non-muscle myosin II (NMII) and are held together by crosslinking proteins such as α-actinin and filamin (57,115). In addition to forming a three-dimensional network within the cell, many SFs terminate in cell-ECM focal adhesions (FAs), providing a mechanism to directly sense and transmit force between the cytoskeleton and ECM (101). While SFs have long been appreciated for their role in stabilizing shape and driving motility on rigid 2D ECMs, advances in imaging now reveal that SFs critically regulate migration in both fibrous 3D matrices (62,116) and tissue (117,118).

Observations that SFs within a single cell can differ in their location, protein composition, and connections to focal adhesions has led to the classification of SFs into three subtypes: dorsal SFs, transverse arcs, and ventral SFs (45,46). Dorsal SFs are oriented perpendicularly to the leading edge of the cell and are anchored at one end to an FA. The other end extends upward (dorsally) and interacts with transverse arcs, which are curved SFs that run parallel to the leading edge and are not anchored directly to FAs. Ventral SFs are located more posteriorly and are anchored at both ends to FAs (12,45). In addition to their varied spatial localization, the three subtypes also differ in their molecular composition and mechanism of formation. Dorsal SFs do not contain NMII and are formed by vectoral actin polymerization (46). On the other hand, transverse arcs and ventral SFs contain NMII clusters, which alternate with crosslinking proteins in a sarcomeric banding pattern. Transverse arcs form from the annealing of Arp2/3-nucleated filaments with mDia2-tropomyosin fragments (50). Ventral SFs may form de novo from the bundling of short actin filaments (102,119) or from the fusion of dorsal SF-flanked transverse arcs during retrograde flow of the SF network (46). During retrograde SF flow, dorsal SFs direct transverse arcs toward the bottom (ventral) surface of the cell, eventually fusing together and forming a ventral SF (46,48). Ventral SFs generate and transmit significant traction forces that detach the trailing end of the cell after protrusion of the leading edge, facilitating motility (75,120).

A core concept of prevailing models of cell mechanics is that cells establish shape homeostasis by actively rearranging a prestressed, mechanically interdependent network, with SFs and other contractile elements contributing tension (121). To this end, there have been several efforts to dissect contributions of specific SF subtypes in generating and maintaining tension, particularly in the context of motility. For example, live-cell imaging and traction force measurements have been elegantly combined to develop a model for the structure of the lamella in which transverse arcs collectively pull on dorsal SFs, which act as levers that flatten the lamella (28). Model-based traction force microscopy, in which cable network models are used to iteratively deduce SF tension values from SF and FA distributions, also hints that ventral SFs bear greater tension than the other two subtypes (75). While these studies have produced important new insights into the field's understanding of SF subtype function, they remain indirect measures of SF mechanical properties. Given the central roles that specific SF subtypes are hypothesized to play in cell structure and motility, there is a significant unmet need to directly and comparatively measure mechanical properties of individual SFs of each defined subtype.

We and others have used laser nanosurgery to selectively cut single ventral SFs in live cells and thereby quantify SF mechanical properties and contributions to cell shape and traction (52,54,63,122,123). Upon incision, SFs release their stored tension, which is experimentally observable through the retraction of the two severed ends of the SF. The retraction kinetics can be interpreted in terms of SF prestress and viscoelastic properties by modeling the SF as a Kelvin-Voigt (KV) material composed of parallel springs and dashpots (29,52,53). Using these tools, it has been found that peripherally-located ventral SFs are under higher prestress than centrally-located ventral SFs. Furthermore, compromise of a single peripheral (but not central) ventral SF substantially destabilizes cell morphology (52,53). More recently, we showed that the degree of myosin regulatory light chain phosphorylation along central and peripheral ventral SFs are preferentially regulated by Rho-associated kinase (ROCK) and myosin light chain kinase (53,123). The degree with which an SF is physically networked with other SFs can also influence the retraction, either slowing or enhancing retraction depending on network architecture and

geometry, and serving as repositories for the released tension that mitigate destabilization of adhesions (54,122).

In this study, we apply laser nanosurgery to directly and systematically measure the viscoelastic properties and structural contributions of dorsal SFs, transverse arcs, and ventral SFs. Each subtype exhibits distinct mechanical properties, with ventral SFs bearing the greatest prestress. Genetic depletion of transverse arcs and dorsal SFs further reveals that ventral SF mechanics depend on the presence of the other two subtypes, a finding that is reinforced by studies on patterned one-dimensional (1D) matrix substrates. Together our results support a model in which the three SF subtypes form a physically and mechanically integrated network in which the contractile properties of ventral SFs are related to and derived from dorsal SFs and transverse arcs.

2.3 Results

Dorsal SFs bear the least prestress and are mechanically coupled to transverse arcs
We focused our studies on U2OS osteosarcoma cells, which assemble robust SF networks and are widely employed as a model system for investigating SF function (28,46,48,62). Consistent with previous observations, we found that U2OS osteosarcoma cells displayed dorsal, transverse arc, and ventral SF subtypes, which we distinguished based on their connections to vinculin in FAs and their location within the cell (Fig. 2.1A, left). SF subtypes also had distinct patterns of di-phosphorylated myosin regulatory light chain (ppMLC) staining, the form of MLC typically associated with high SF contractility (16,20,21). Dorsal SFs were devoid of ppMLC, whereas transverse arcs and ventral SFs had punctate ppMLC staining.

Upon closer examination of dorsal SF and transverse arc retractions, we noticed that the retraction of one SF subtype was influenced by the other. When a transverse arc was severed, its retraction distance was influenced by the presence of orthogonally-networked dorsal SFs (Fig. 2.2A). Connected dorsal SFs halted the retraction of one of the severed ends of the transverse arc long before the other severed end plateaued, resulting in the asymmetric retraction of the two ablated ends (Fig. 2.2Ai, Fig 2.2B traces 1 and 2). In contrast, a transverse arc that was not locally intersected by a dorsal SF retracted unhindered, and both SF ends retracted at approximately the same rate and plateaued simultaneously (Fig. 2.2Aii, Fig. 2.2B traces 3 and 4). When a dorsal SF was severed, the posterior severed end located closer to the cell center centripetally translocated in concert with an orthogonally-associated transverse arc. The posterior fragment displaced a greater distance than the anterior fragment (p < 0.0001), suggesting that dorsal SFs are inherently non-contractile, and are instead secondarily tensed by networked transvers arcs (Fig. 2.2C-E). These results were also supported by experiments where we severed multiple SFs in a single cell. When we simultaneously severed two adjacent dorsal SFs, the posterior and anterior severed ends of both SFs retracted similarly as in the case when one dorsal SF was severed, with little translocation of the anterior end (Appendix I – Fig. S2A). However, when we first severed a transverse arc at two points straddling its intersection with a dorsal SF and then severed the dorsal SF, the release of tension in the transverse arc reduced both the extent and anterior/posterior asymmetry of the translocation of the dorsal SF segments (Appendix I – Fig. S2B). Taken together, these results indicate that the dorsal SF and transverse arc networks are mechanically integrated. These findings are also consistent with a model in which myosin-containing transverse arcs exert contractile forces that are collectively transmitted

to dorsal SFs, which in turn anchor to FAs and passively transmit tension from the center of the cell to anterior adhesions (28).
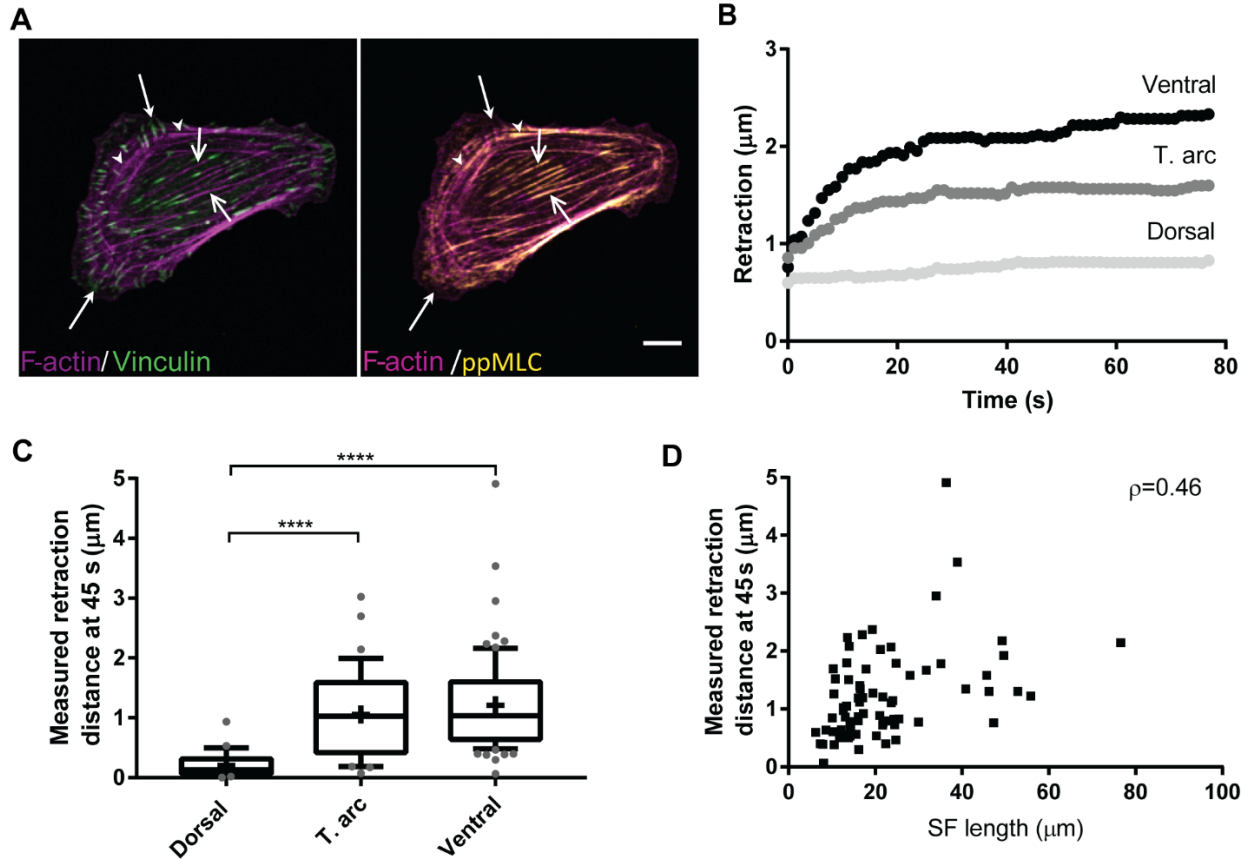

Figure 2.1. Dorsal SFs bear less prestress than transverse arcs and ventral SFs. (A) Dorsal SFs (filled arrows), transverse arcs (arrow heads), and ventral SFs (open arrows) in U2OS cells. SFs (magenta) are classified into subtypes based on their connections to vinculin clusters (green), their decoration with ppMLC (yellow), and their location in a migrating cell. Scale bar 10 µm. (B) Typical retraction traces of ablated SFs for each of the three subtypes. (C) Measured retraction distance 45 s after ablation. N = 29, 37, 74 dorsal SFs, transverse arcs, and ventral SFs, each from different cells, across 13-17 independent experiments. Kruskal-Wallis test, post-hoc Dunn's test, **** p < 0.0001. Cross indicates mean. Error bars show 10th and 90th percentiles. (D) Ventral SF retraction distance plotted against the SF length (Spearman's rank coefficient ρ = 0.46, N = 74 ventral SFs from (C)).

Genetic depletion of transverse arcs reduces prestress on ventral SFs

Given the mechanical interdependence between subtypes observed at the single-SF level, we asked what would happen to SF architecture and mechanics if we disrupted specific SF subtypes more globally. To do so, we used shRNAs to stably knock down (KD) palladin (90 and 140 kDa isoforms) or mDia2, which have respectively been shown to be critical in the formation of dorsal SFs and transverse arcs (50,62). To facilitate quantification of subtype targeting, cells were patterned onto fibronectin crossbow micropatterns to standardize cell shape and area (Fig. 2.3A, Appendix I – Fig. S3) (124). The crossbows compel the cell to adopt a polarized, migratory morphology, with dorsal SFs and transverse arcs preferentially at the curved region of the crossbow, and ventral SFs at the pointed end of the crossbow (61,62). After confirming protein depletion in our cell lines (Appendix I – Fig. S4A), we cultured these cells on crossbow

patterns and found that palladin and mDia2 KD respectively and selectively reduced dorsal SF and transverse arc density relative to both naïve cells (palladin KD dorsal SF reduction: $p < 0.05$; mDia2 KD transverse arc reduction: $p < 0.05$) and control cells transfected with a non-targeting (NT) shRNA sequence (palladin KD dorsal SF reduction: $p < 0.001$; mDia2 KD transverse arc reduction: $p < 0.05$) (Appendix I – Fig. S4B-C). On unpatterned matrices, both the mDia2 KD/transverse arc-depleted and palladin KD/dorsal SF-depleted cells displayed morphological differences (Appendix I – Fig. S4D). Specifically, mDia2 KD/transverse arc-depleted cells often adopted irregular shapes with multiple lamella-like projections that lacked clearly-defined transverse arcs. Palladin KD/dorsal SF-depleted cells were often rounded and had numerous small, punctate adhesions along the protrusive ends, consistent with an inability of the adhesions to mature (61,62).

We returned to crossbow-patterned substrates to quantify the effects the of dorsal SF and transverse arc depletion on the mechanics of the remaining SFs by laser nanosurgery. We began by repeating our sequential-severing experiments in patterned naïve cells, which revealed similar interdependences between dorsal SFs and transverse arcs (Appendix 1 – Fig. S5). Next, we considered our palladin and Dia2 KD cells; we focused on measuring retraction profiles of ventral SFs, since this was the most prominent subtype in our cell lines and because we did not observe changes in transverse arc and dorsal SF retraction upon depletion of the other subtypes (Fig. 2.3A, Appendix 1 – Fig. S6). To quantitatively compare retraction across cell lines, we fitted the retraction kinetics of ventral SFs to a KV model (52,53) (Fig. 2.3B). As discussed earlier, this model enables extraction of two parameters: L_o, the plateau retraction distance of the severed SF and a measure of stored elasticity, and τ, the exponential time constant of retraction, which represents the ratio of SF viscosity to elasticity. A third parameter, D_a, is the fitted length of the SF destroyed during the ablation. By comparing L_o values, we found that ventral SFs in the mDia2 KD/transverse arc-depleted cells had lower prestresses than in palladin KD/dorsal SF-depleted ($p < 0.05$), NT ($p < 0.05$), and naïve ($p < 0.05$) cells. Depletion of either protein/SF subtype did not significantly influence τ values (Fig. 2.3C). Consistent with this reduction in prestress, ventral SFs in the mDia2 KD/transverse arc-depleted cells also had lower levels of ppMLC staining (vs. palladin KD/dorsal SF-depleted: $p < 0.01$; vs. NT: $p < 0.0001$; vs. naïve: $p < 0.0001$) (Fig. 2.3D). Together, the altered retraction kinetics and ppMLC localization indicate that ventral SFs in transverse arc-depleted cells are less tensed due to lower levels of myosin activity.
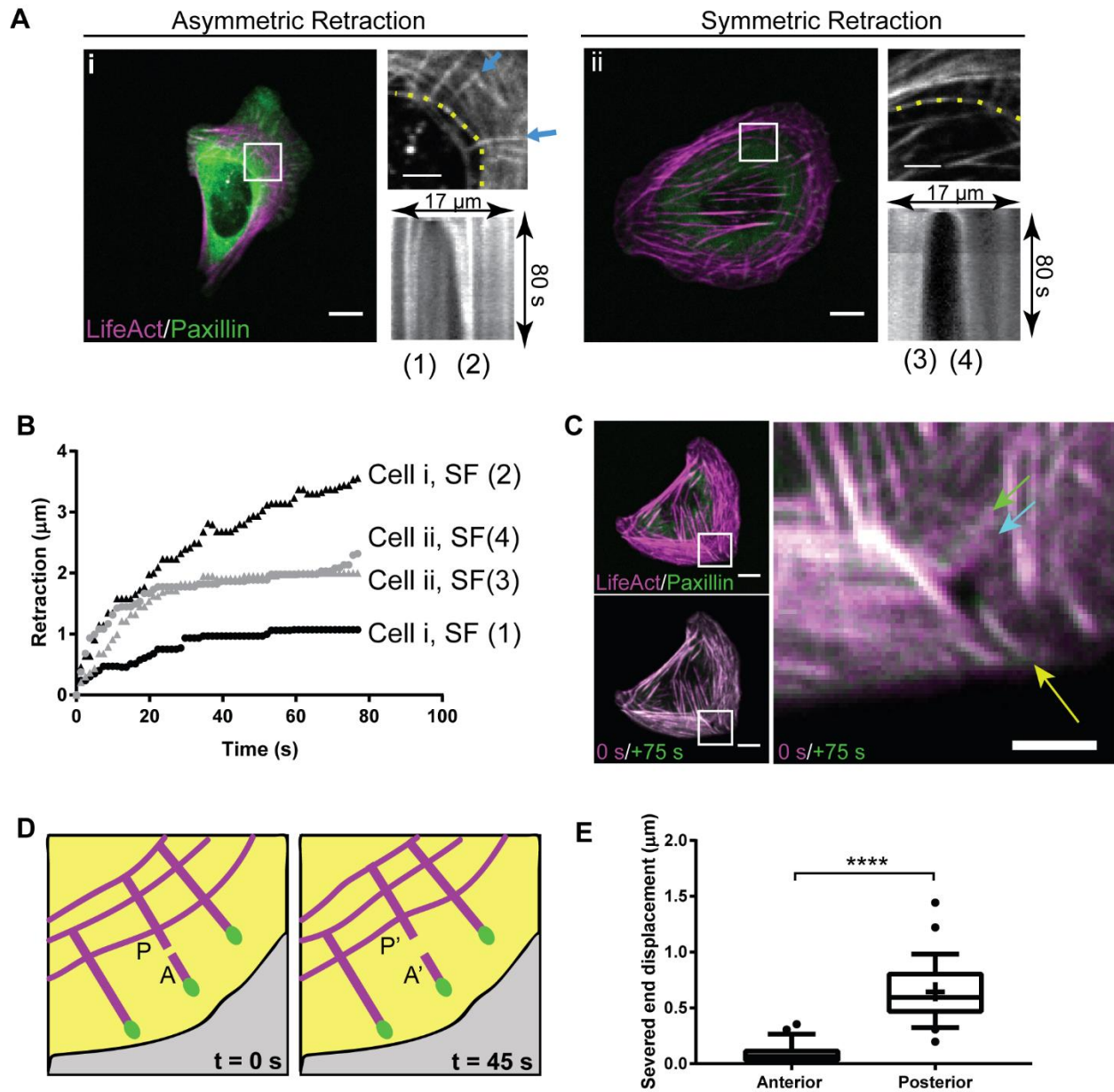
Figure 2.2. Transverse arcs are mechanically coupled to dorsal SFs. (A) Panel (i): Asymmetric retraction of severed transverse arc ends, or Panel (ii): Symmetric retraction of severed transverse arc ends due to the presence or absence of dorsal SFs in the immediate vicinity of the ablation site. Inset and kymograph show the region of interest and the retraction of the transverse arc. Dashed yellow lines indicate the severed transverse arc and blue arrows point to networked dorsal SFs. (B) Retraction traces of the severed transverse arc ends shown in (A). Black traces (1) and (2) correspond to panel (i). Gray traces (3) and (4) correspond to panel (ii). (C) After severing, the posterior fragment of a dorsal SF translocates with a connected transverse arc whereas the anterior severed end translocates a short distance. Top left panel shows cell before the dorsal SF (yellow arrow) is ablated. Bottom left shows a before/after overlay. Inset shows the region of interest. The cyan and green arrows indicate the location of the transverse arc before and after ablation of the dorsal SF, respectively. (D) The translocation of each severed dorsal SF end is tracked. A: anterior end closer to the leading edge of the cell; P: posterior end closer to the cell center. (E) Measured displacement of anterior and posterior severed dorsal SFs ends 45 s after severing. Wilcoxon matched-pairs rank test, **** $p < 0.0001$, N = 29 dorsal SFs, each from different cells across 13 independent experiments. Cross indicates mean. Error bars show 10th and 90th percentiles. Scale bar: 10 µm for main panel, 5 µm for insets.

Ventral SFs commonly fail to plateau in palladin KD/dorsal SF-depleted cells
During our analysis of ventral SF retraction, we noticed that there was a subset of fibers in the SF-depleted and control cells with fitted τ values that exceeded 60 s. These extended retraction events were excluded from the analysis of KV parameters (Fig. 2.3), as the large τ values suggested that the fiber did not fully plateau in the 77 s tracking window (Appendix I – Fig. S7). In the case of the palladin KD/dorsal SF-depleted cells, these fibers retracted with kinetics that were more linear than exponential. We verified that these non-plateauing retractions were not due to SF depolymerization; in separate experiments, we photobleached fiducial markers along the length of the SF and observed that these marks translocated in coordination with the severed ends following incision of the fiber (Appendix I – Fig. S8) (52).

In previous work, we had shown that internal and external crosslinking can serve as a brake that limits SF retraction (29,122). Thus, we initially hypothesized that the atypical SF retractions might be due to altered crosslinker morphology along SFs. Internal crosslinkers within an SF would include the components of non-contractile dense bodies, such as α-actinin and palladin, which stiffen the SF and limit retraction (29). External crosslinkers are structures outside of the ablated SF that might influence retraction of the severed ends, such as other networked SFs (122) and nascent cell-matrix adhesions (63). Given that palladin is an actin crosslinker and a key component of dense bodies (125–127), suppression of palladin might be expected to globally destabilize SF internal crosslinking. To assess dense body architecture, we stained for α-actinin-1, a crosslinking protein that interacts and colocalizes with palladin in dense bodies (128). Surprisingly, structured illumination microscopy (SIM) revealed that the crosslinking morphology was similar along the center of ventral SFs across both the palladin KD/dorsal SF-depleted cells and the NT cells, with α-actinin-1 localizing to SFs in regularly spaced puncta (Fig. 2.4A). Therefore, we concluded that palladin suppression does not broadly disrupt internal SF crosslinking, making altered crosslinking at the center of the SF an unlikely cause of non-plateauing retractions.

Since palladin KD/dorsal SF-depleted cells had SFs with linear retraction kinetics, and the crosslinker morphology along the center of ventral SFs did not appear to be different from control cells, we next hypothesized that the non-plateauing ventral SF retraction might be related to the absence of dorsal SFs. We arrived at this idea because ventral SFs can form through at least two routes: the fusion of two dorsal SFs flanking transverse arcs during retrograde SF flow or from the *de novo* annealing of short actomyosin fragments (46,48,102,119). In the former case, progenitor transverse arcs would be expected to confer elastic prestress to their ventral SF progeny through the contribution of myosin motors, which dorsal fibers lack.

Conversely, dorsal SFs, which are rich in crosslinkers (28,61,62) and passively transmit tension from transverse arcs to FAs, might facilitate SF braking during retraction. As we have shown, ventral SFs in mDia2 KD/transverse arc depleted cells are under lower prestress, and some ventral SFs in palladin KD/dorsal SF-depleted cells have altered retraction profiles. Consistent with this idea, α-actinin-1 continuously decorates dorsal SFs rather than assembling into the sarcomeric puncta seen in transverse arcs and ventral SFs (Fig. 2.4A). Furthermore, the termini of ventral SFs (corresponding to the location of FAs) in palladin KD/dorsal SF-depleted cells have shorter regions of continuous α-actinin staining than ventral SF termini in NT cells (Fig. 2.4B-E). Thus, the linear retraction kinetics of ventral SFs in the palladin KD/dorsal SF-depleted

cells could be a consequence of reduced SF braking. In the *de novo* ventral SF formation pathway, actomyosin bundles are annealed together without the participation of crosslinker-rich dorsal SFs, such that the resulting SFs would also be expected to have atypical retractions.

Cell shape and SF architecture can be controlled by patterning thin-width microlines
If the above hypothesis is true, then compelling cells to form ventral SFs through *de novo* assembly (rather than dorsal SF/transverse arc fusion) should strongly reduce braking during retraction and favor linear or atypical SF retractions. To achieve this regime, we constrained cells to patterned fibronectin microlines of widths ranging from 2-50 µm (Fig. 2.5A). The thinner microlines (e.g. 2 µm wide) laterally constrain cell spreading to an extent that precludes assembly of canonical lamella, with a corresponding absence of dorsal SFs and transverse arcs (Appendix I – Fig. S9). On such matrices, the SF network would be dominated by ventral SFs, which would necessarily have to arise from *de novo* actomyosin assembly rather than dorsal SF/transverse arc fusion. Indeed, when cultured on 2 µm microlines, all cell lines adopted a spindle-like morphology with two long ventral SFs running the length of the cell along the outer edge of the pattern (Fig. 2.5B). As expected, wider microlines were increasingly permissive to lamella formation and cells began to resemble those on unpatterned substrates. NT and naïve cells on 10 µm wide lines displayed short dorsal SFs near one end of the cell and, in some cases, short and slightly curved SFs reminiscent of transverse arcs. On the 50 µm microlines, the NT and naïve cells were able to form all three SF subtypes. mDia2 KD/transverse arc-depleted and palladin KD/dorsal SF-depleted cells similarly began to take on their respective morphologies on unpatterned matrices with increasing microline width.
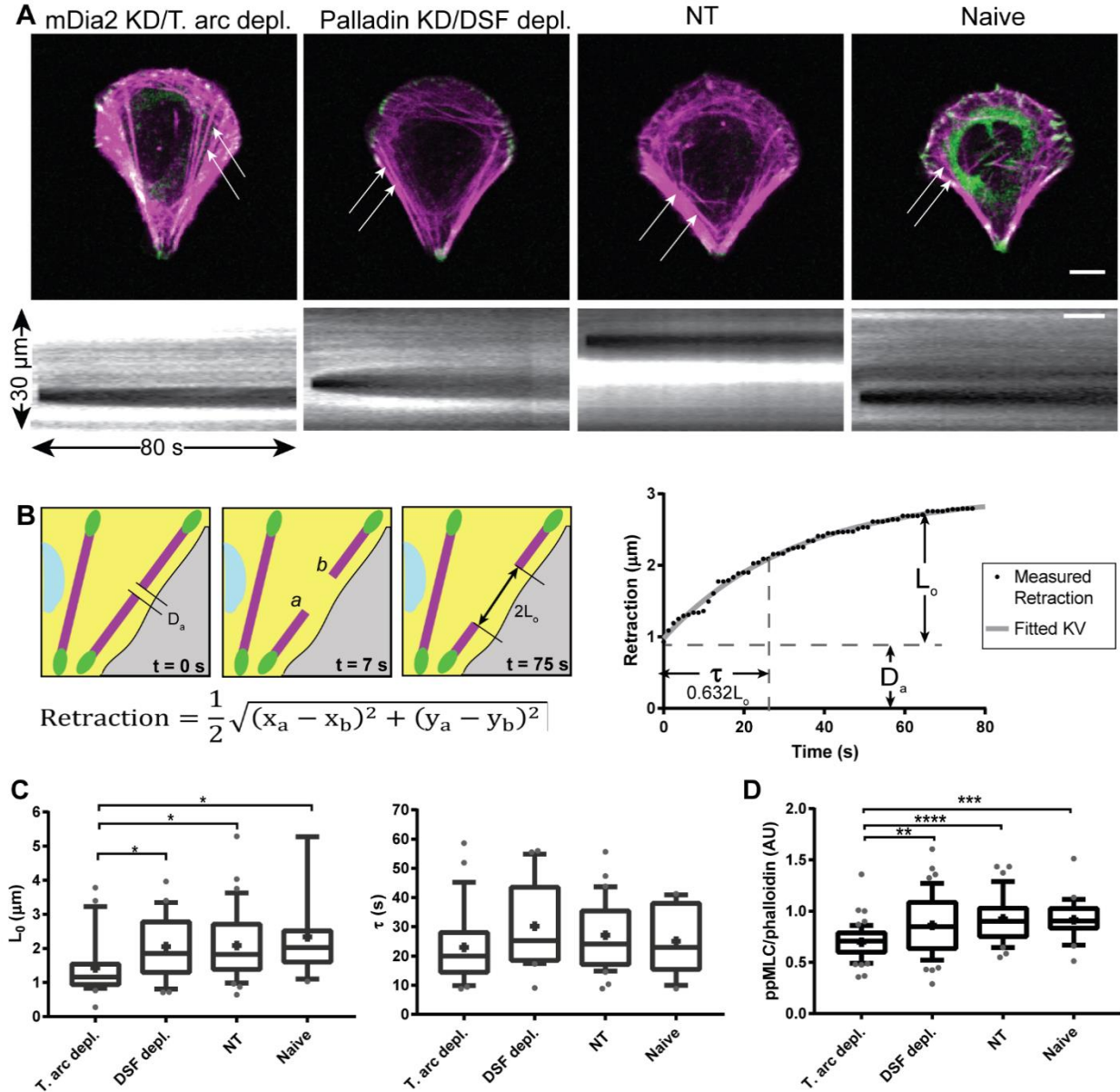
Figure 2.3. Ventral SFs in cells with depleted transverse arcs have altered retraction kinetics. (A) Top panel: Representative images of mDia2 KD/transverse arc-depleted, palladin KD/dorsal SF-depleted, NT control, or naïve control cells on crossbow micropatterns. Bottom panel: Kymographs of ablated ventral SF indicated by the white arrow in the top panel show retraction. Scale bar 10 µm. (B) Schematic of SF retraction measurement and analysis. The retraction of ventral SFs is measured by taking one-half of the distance between the severed ends. The resulting retraction vs. time profile can be fitted to the KV model for viscoelastic materials, with characteristic parameters L_o (elastic prestress), τ (viscoelastic time constant), and D_a (length of SF destroyed during ablation). (C) Fitted KV parameters for ventral SFs in each of the cell lines. (D) Analysis of ppMLC intensity in ventral SFs, normalized to phalloidin. mDia2 KD/transverse arc-depleted cells contain less ppMLC. N = 24, 21, 34, 13 SFs from different mDia2 KD/transverse arc-depleted, palladin KD/dorsal SF-depleted, NT, or naive cells across 7-9 independent experiments for (C). N = 56, 48, 37, 23 SFs from different mDia2 KD/transverse arc-depleted, palladin KD/dorsal SF-depleted, NT, or naive cells across 2 independent experiments for (D). * $p < 0.05$, ** $p < 0.01$, *** $p < 0.001$, **** $p < 0.0001$, Kruskal-Wallis test, post-hoc Dunn's Test. Cross indicates mean. Error bars extend to 10th and 90th percentiles.

19

A

NT | Palladin KD/DSF depl.

α-actinin-1
Phalloidin

Inset

B

NT | Palladin KD/DSF depl.

Inset

C

DSF depl./Palladin KD | NT

Phalloidin pPaxillin | α-actinin-1 | Phalloidin pPaxillin | α-actinin-1

D
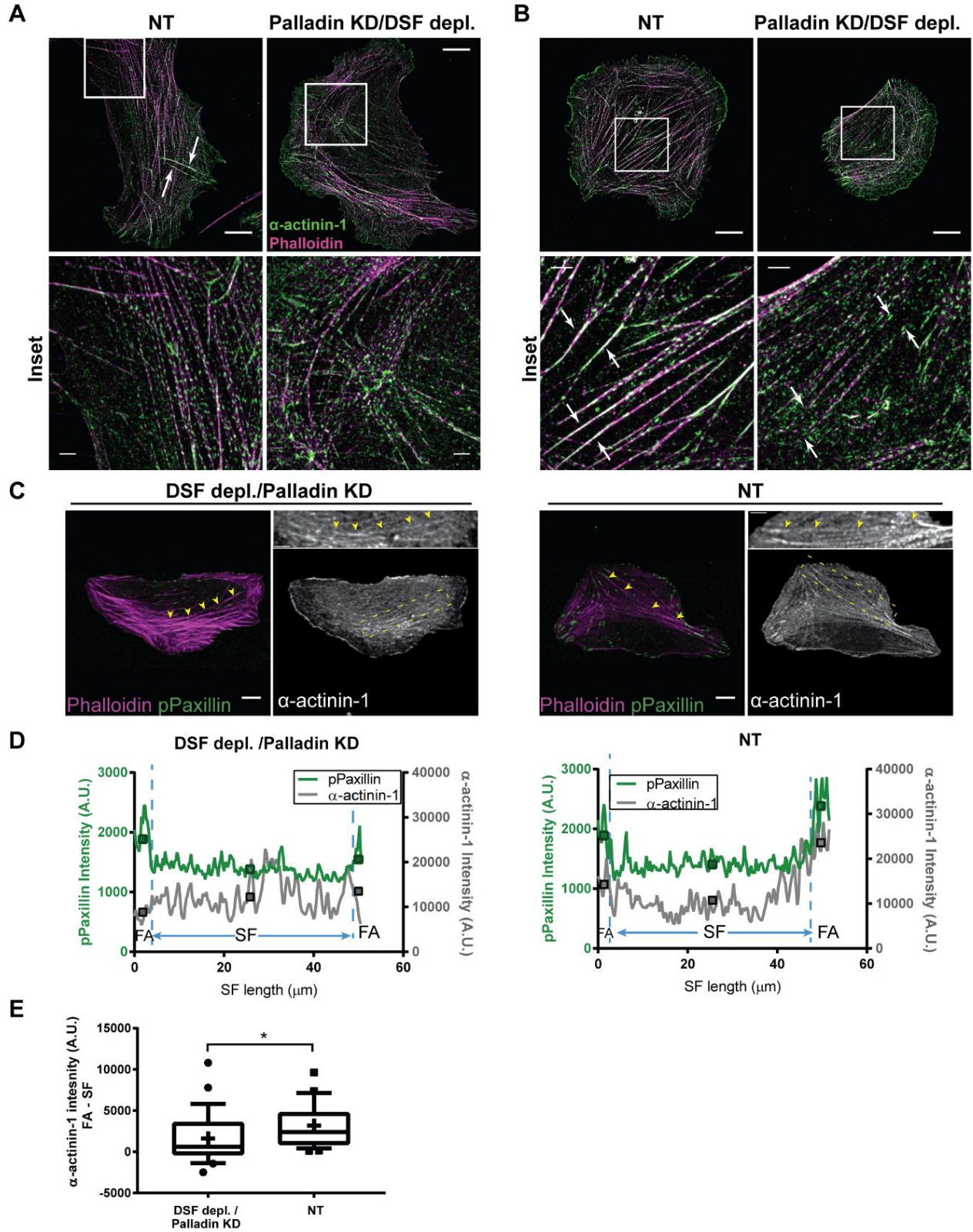
DSF depl. /Palladin KD | NT

E

Figure 2.4. Palladin KD-mediated depletion of dorsal SFs does not grossly destabilize ventral SF dense body organization at the SF center. (A) Periodic clusters of α-actinin-1 (green) crosslinkers along transverse arcs and ventral SFs in SIM images of NT or palladin KD/dorsal SF-depleted cells. SFs are stained using phalloidin (magenta). Arrows point to dorsal SFs, which have continuous α-actinin-1 staining. (B) α-actinin-1 enrichment at the ends (white arrows) of ventral SFs in NT cells. These regions are not present in palladin KD/dorsal SF-depleted cells. For (A) and (B), the bottom row depicts high-magnification images of the insets (white boxes). Scale bars: 10 µm (top row), 2 µm (bottom row). (C) Representative confocal images of palladin KD and NT cells stained for pPaxillin (green), F-actin (magenta), and α-actinin-1 (gray). Box indicates region of interest containing a ventral SF (yellow arrowheads) that is measured. Scale bar: 10 µm, inset: 5 µm. (D) Line scans of the indicated ventral SFs in the pPaxillin (green) and α-actinin channels (gray). Vertical dashed blue lines delineate the FA regions, as determined by pPaxillin fluorescence, from the rest of the SF. Squares indicate mean fluorescence intensity of the indicated region. Line scans were used to determine the difference in average α-actinin-1 fluorescence intensity at the FA-ends of SF and the center of the SF. (E) Difference in the average α-actinin-1 intensity at the FA-ends and at the center of the SF for 28 palladin KD/DSF-depleted or 24 NT cells (1-3 SFs measured per cell) from 3 independent experiments. * $p < 0.05$, Wilcoxon rank sum test.

Atypical/non-KV ventral SF retractions decrease in frequency with increasing microline width for all cells with the exception of palladin KD/dorsal SF depleted cells.

When we ablated ventral SFs in cells on the 2, 10, and 50 µm microlines we found that the 77 s imaging window that we used previously was often insufficient to fully capture the retraction profile of the severed SF ends, with many SFs failing to reach a plateau by that time (Fig. 2.6A, Movie S11). When we addressed this by extending our imaging window time to 155 s, we noticed that the retraction profiles fell within three categories: (1) negative exponential that fit a KV retraction (typical for ventral SFs in NT and naïve cells), (2) linear, or (3) retraction in two, or occasionally, more stages with some permutation of linear and exponential retractions (Fig. 2.6B, Appendix I – Fig. S10). There were instances of atypical/non-KV retractions in all cell lines on the 2 µm microlines (Fig. 2.6C-D, Appendix I – Fig. S10), which as described above, only permit assembly of ventral SFs. The proportion of atypical/non-KV retractions (i.e. retraction profiles 2 and 3) encompassed more than 50% of the ablated SFs in each cell line and was not significantly different between cell lines ($p = 0.63$) (Fig. 2.6E, left). This indicates that dorsal SFs and transverse arcs do not contribute appreciably to overall SF network assembly in these confined settings: ventral SFs in all cells on the 2 µm microlines, regardless of SF depletion status, are qualitatively similar in terms of SF architecture and prestress.

On wider 10 and 50 µm microlines, NT and naïve cells can increasingly form dorsal SFs and transverse arcs and, subsequently, a population of ventral SFs from these precursor fibers. Correspondingly, as the microline width increases, the proportion of ventral SFs displaying KV retractions in control cells also increases and consists of up to 88% of the ablated fibers in cells on the 50 µm microlines. We observed a similar trend in the mDia2 KD/transverse arc-depleted cells; however, only 60% of retraction events follow KV kinetics in palladin KD/dorsal SF-depleted cells on 50 µm microlines (Fig. 2.6E, middle and right), which is significantly lower than in all other cell lines ($p < 0.001$). These results suggest that dorsal SFs may influence ventral SF retraction by braking the retraction of SFs. Without this brake, SFs exhibit atypical, extended retraction profiles.
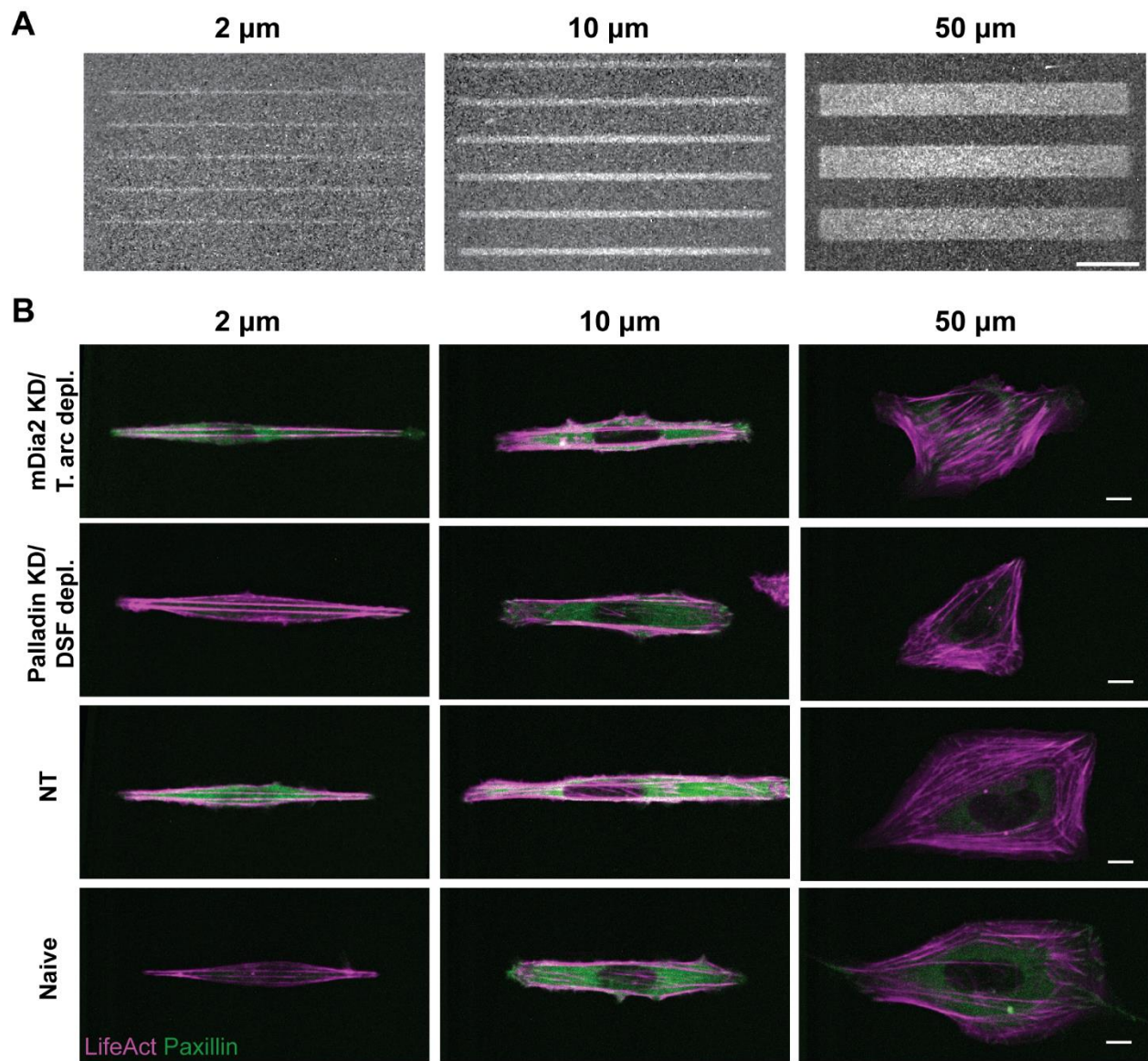
Figure 2.5. Ventral SFs on microline-patterned cells. (A) Patterning of fibronectin microlines onto glass coverslips, visualized with fluorescently labeled fibronectin. Scale bar: 100 µm. (B) Representative LifeAct (magenta)/paxillin (green) images of cells patterned on 2, 10, or 50 µm microlines. Scale bar: 10 µm.
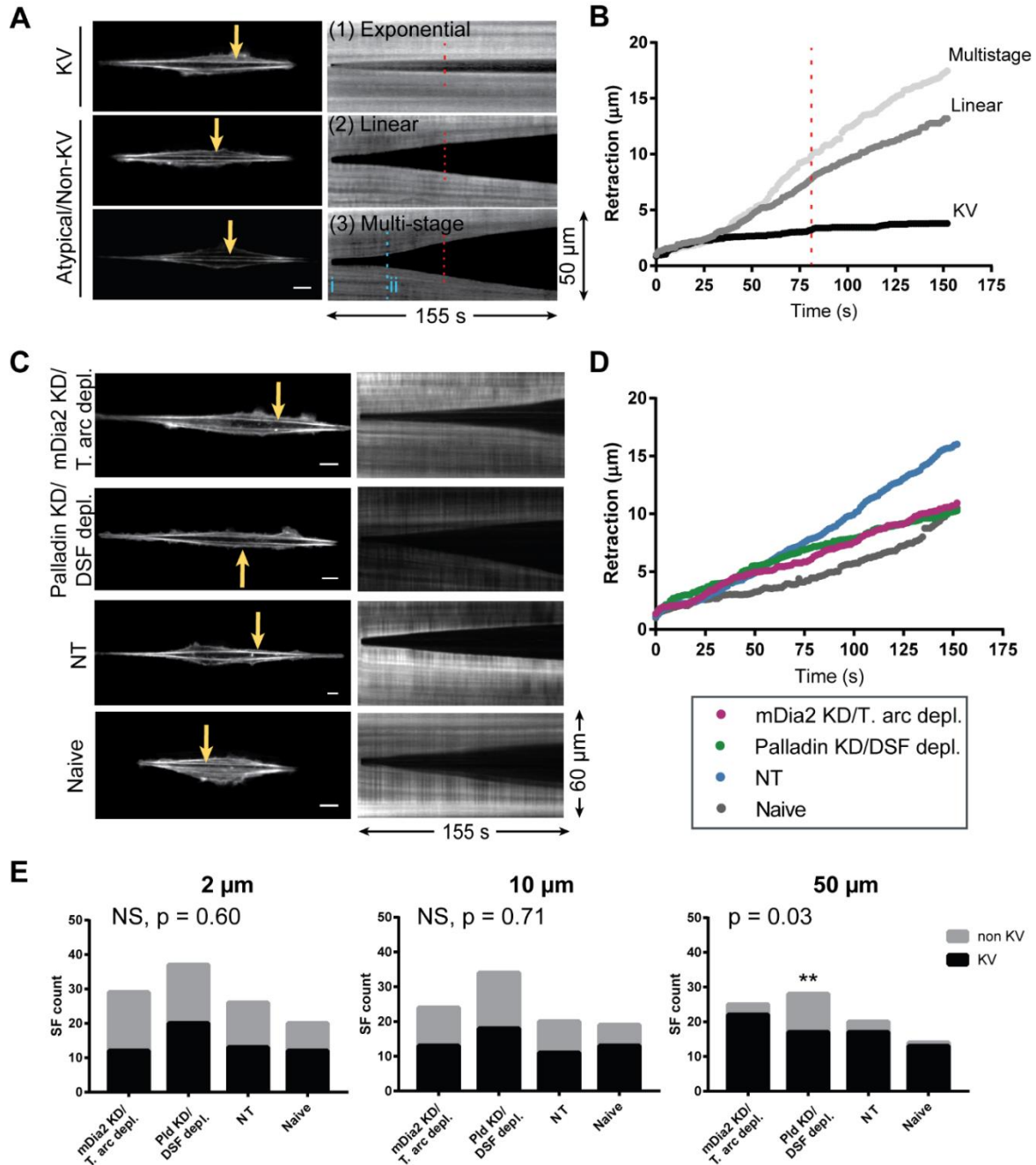
Figure 2.6. Microline-constrained cells exhibit atypical retraction profiles. (A) Typical kymographs and corresponding retraction traces of ablated SFs (yellow arrows) in NT cells on 2 µm microlines. Three categories of retraction profiles (1) exponential (KV), (2) linear (non-KV), or (3) multistage (non-KV, stages are demarcated by dashed blue line) are observed. The red dashed line is the halfway point, or 77 s. (B) Retraction traces of the kymographs from (A). (C) Example non-KV retractions of severed ventral SFs (yellow arrow) on 2 µm microlines. Kymographs show the retraction of the indicated fiber. Scale bar: 10 µm. (D) Retraction traces of the kymographs in (C). (E) Distribution of retraction profiles for ventral SFs in each of the cells on 2,10, or 50 µm microlines. 2 µm pattern: N = 29, 37, 26, 20 ventral SFs; 10 µm pattern: N = 24, 34, 20, 19 ventral SFs; 50 µm pattern: N = 24, 28, 20, 14 ventral SFs, each from different mDia2 KD/transverse arc-depleted, palladin KD/dorsal SF-depleted, NT, and naïve cells, respectively. Cells are from 5-9 independent experiments. p-values are from a Chi-square test for cells on 2 or 10 µm microlines or from the Fisher's Exact test for cells on 50 µm microlines. ** p < 0.01: comparison between palladin KD/DSF depleted cells and other cell lines. NS: not significant.

23

2.4 Discussion

SFs in migrating cells are canonically categorized into three subtypes based on their location, composition, and anchorage to FAs. By combining single-SF laser nanosurgery, subtype-specific depletion, and micropatterning, we have directly demonstrated that each subtype bears unique, non-overlapping mechanical properties and structural roles. These differences arise in turn from both intrinsic variations in composition across the subtypes and extrinsic variations in connectivity to other SFs and presumably other cytoskeletal elements. Specifically, our work reveals that dorsal SFs bear little intrinsic prestress and instead are externally tensed by mechanically-coupled contractile transverse arcs. Furthermore, ventral SFs, which may form from the fusion of dorsal SFs and transverse arcs, depend on the integrity of both of these progenitor SF pools, as depletion of either subtype influences ventral SF retraction kinetics (Fig. 2.7).

Our results represent the first direct, subtype-specific measurements of SF mechanical function, and as such, complement and directly test predictions of more indirect, cell-scale analyses of SF networks. In particular, a recently proposed model assigns dorsal SFs and transverse arcs different roles in shaping the flattened lamella of migrating cells (28). Specifically, transverse arcs are postulated to contract, thus pulling on rigid dorsal SFs, which lever against the ECM through FAs and produce a flattened lamella. This elegant model was deduced in part from loss-of-function studies in which transverse arcs were dissipated through the use of contractility inhibitors (e.g. blebbistatin, Y-27632) or myosin IIA KD (28). The influence of both interventions would be expected to extend beyond transverse arcs, as evidenced by the finding that contractility inhibition and myosin IIA KD also reduced the population of ventral SFs (28). As another example, model-based traction force microscopy has been used to deduce tension values borne by individual SFs by reconciling traction force maps against SF and FA distributions through an elastic cable network model (75). However, this approach is computationally intensive, depends on a specific mechanical model, and requires high-resolution imaging and traction force measurement. Our study addresses many of these gaps by applying laser nanosurgery to conduct direct loss-of-function studies on single SFs. These measurements enable us to disrupt single SFs in an isolated fashion and invoke simple KV models of viscoelasticity to infer prestress. In doing so, our results support and integrate predictions of both measurements into a unified picture of SF network mechanics: dorsal SFs are intrinsically non-contractile and are tensed by associated transverse arcs, which are reciprocally constrained by their connections to dorsal SFs. Additionally, ventral SFs bear the greatest prestress of any subtype, consistent with their role in detaching mature adhesions at the trailing edge of the cell (14,25,26).

Our results also offer new insights into how the mechanical properties of ventral SFs relate to their mechanism of formation. Ventral SFs have been observed to form from the fusion of dorsal SFs and transverse arcs during retrograde flow (12,46,48). However, it has been unclear how the structure and mechanics of progenitor SFs might affect the properties of the resulting progeny ventral SF. By selectively depleting dorsal SF or transverse arc SF subtypes and severing the remaining ventral SFs, we have gathered support for a model in which ventral SF retraction is driven by myosin derived from progenitor transverse arcs and braked by crosslinkers derived from dorsal SFs (Fig. 2.7). Specifically, contractile transverse arcs contribute NMII to newly formed ventral SFs during retrograde flow, with increased contractile loads leading to the incorporation of more NMII units to the fiber. Non-contractile dorsal SFs contribute additional

braking elements (i.e. SF crosslinkers), which continuously decorate, rather than sarcomerically organize, within dorsal SFs. We speculate that the positioning of the dorsal SFs at either end of the proto-ventral SF act as either internal braking regions that stop the progressive collapse of sarcomeric units along a SF when severed or as tethering points to matrix adhesions or cytoskeletal elements.
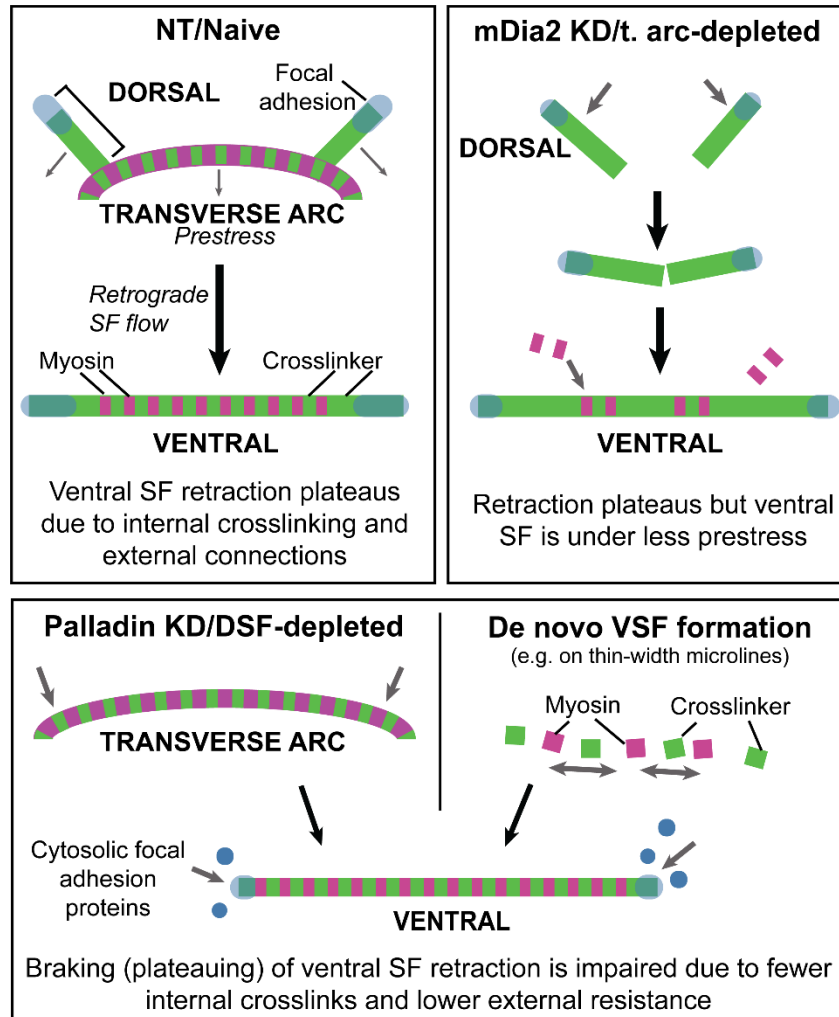
Figure 2.7. Model of ventral SF viscoelastic properties. Ventral SFs may form from the fusion of transverse arcs and dorsal SFs (e.g. in NT/naïve cells). Precursor transverse arcs contain NMII which contributes prestress and precursor dorsal SFs contribute braking elements that lead to the plateauing of the subsequently formed ventral SF. Ventral SFs in transverse arc-depleted cells are under less prestress because they are deficient in NMII introduced by transverse arcs. Ventral SFs that form in dorsal SF-depleted cells or de novo, lack the crosslinker regions that contribute to braking SF retraction.

Knockdown of mDia2 or palladin enabled us to examine the contributions of transverse arcs and dorsal SF subtypes to ventral SF mechanics. Selectively depleting transverse arcs by knocking down mDia2 results in weakly contractile ventral SFs, which can be attributed to the progenitor fibers lacking a contractile element. Some NMII from the cytoplasmic pool may be incorporated

along the length of this ventral SF; but overall, the fiber is under less prestress. On the other hand, reduction of dorsal SFs via palladin depletion results in ventral SFs with impaired braking during retraction. Specifically, dorsal SFs contribute crosslinkers which slow and eventually halt retraction as the tension released by the collapsing sarcomeres is eventually balanced by the load placed on the crosslinkers. In support of the braking role of crosslinkers, SIM images of the NT controls showed an enrichment in α-actinin-1 at the ends of ventral SFs where FAs are expected to be. These enriched regions were largely reduced in the palladin KD/dorsal SF-depleted cells (Fig. 2.4B-E). Similarly, ventral SFs that form de novo from the annealing of short actomyosin fragments (i.e. independent of dorsal SFs and transverse arcs, as in cells on 2 µm-wide microlines) also have impaired braking as they are presumably not enriched in crosslinkers at the ends. The crosslinkers at the ends and in dense bodies along the center length of the fiber may also act as brakes by physically inducing nascent adhesion formation as the cut ends of the fiber slide along the basal membrane, as others have proposed (63). Our images did not reveal the presence of canonical ECM adhesions or connections to other actin-based structures in these regions. However, both α-actinin and palladin crosslinkers are known to bind to FA proteins (129–131). Thus, dorsal SF depletion via palladin KD, or a reduction in crosslinker density anywhere along the length of the fiber, could reduce restoring forces and impair the arrest of SF retraction. Our findings and model are consistent with past studies of single SF mechanics, including our own past work showing that kinase-specific induction of myosin activation within an SF increases its prestress without dramatically changing the viscoelastic time constant (123). Similarly, our current study reveals that depletion of transverse arcs reduces the levels of active myosin in ventral SFs, concurrently lowering prestress without significantly affecting the viscoelastic time constant. Nevertheless, we fully acknowledge that myosin, internal crosslinks, and external connections are each likely to contribute to SF viscoelastic properties in complex ways and that additional studies are needed to directly and critically test specific aspects of our model.

While palladin and mDia2 KD have been previously used to deplete SF subtypes (50,62), we do note that a limitation of this approach is the likelihood of collateral effects on cell function, including FA dynamics and microtubule stability (127,132). We thus turned to the use of 1D ECM patterns as an independent way of manipulating SF subtypes. By varying the width of ECM patterns, we were able to control the formation of SF subtypes and examine the resulting effect on SF retraction behavior. On the narrowest (2 µm) microlines, we observed that a large proportion of ventral fibers in all of our cell lines had atypical/non-plateauing retractions, with this proportion falling for all cells, except for the palladin KD/dorsal SF-depleted cells, on the 50 µm microlines. The 2 µm microlines led to cells with mutually similar shapes and thus similar SF architectures and SF retraction profiles, since ventral SFs are forced to form from the de novo pathway. However, the abundance of atypical retractions on the 2 µm microlines could also be accounted for by the polarization of traction forces, which would be expected to increase the tension borne by a single fiber. The vast majority of the SFs in these constrained cells are oriented parallel to the pattern, meaning that there are few connections to other SFs that could absorb the released tension. Migration and traction force studies have shown that thin microlines readily polarize the cell, and concentrate forces at the front and back of the cell (100,133). Finally, the SFs that were ablated tended to be long (median lengths are about 60 µm, though some can exceed 100 µm), which may mean that a longer time window is needed to fully capture the full retraction profile of the SF, as others have shown that the viscoelastic time constant of the SF increases with length (122).

Our work demonstrates that the three canonical SF subtypes exhibit distinct structural roles and interconnect to form a physically integrated network. Because of this integration, compromise of one subpopulation influences the other, a conclusion supported by both our single-SF nanosurgery and subtype-specific knockdown studies. An important open question is how these relationships manifest themselves in more complex ECMs, including three-dimensional (3D) fibrous matrices representative of connective tissue. One-dimensional microlines have been shown to capture defining features of 3D motility (100), raising the intriguing possibility that the SF mechanics we observe on microlines may offer predictive insights into 3D matrices. Future studies exploring the mechanics of single SFs in these complex matrices should offer valuable insight into how the individual SFs tense the cytoskeleton and ultimately establish shape homeostasis and directional migration.

2.5 Materials and Methods

Cell culture and knockdowns

U2OS cells (ATCC HBT-96) were maintained in DMEM (Gibco) supplemented with 10% FBS (JR Scientific), 1% nonessential amino acids (Gibco), and 1% Penicillin/streptomycin (Gibco). Cells were tested for mycoplasma every three months and authenticated via short tandem repeat profiling.

Cloning and cell line generation

To create knockdown cells, we used shRNA constructs targeting all nine isoforms of palladin (5'- AATCACTACACCATTCAAAGA-3') or mDia2 (5'-AAGCAGAGCTACAAGCTTTTA-3'). A non-targeting sequence (NT: 5'-GCTTCTAGCCAGTTACGTACA-3') was also included as a control. Each oligonucleotide was inserted into the pLKO.1-TRC cloning vector (Addgene plasmid #10878) using AgeI and EcoRI (134) (verified by sequencing). pYFP-paxillin (Addgene plasmid #50543) was cloned into the pLVX-AcGFP vector using XhoI and EcoRI. RFP-LifeAct was cloned into the pFUG vector as described previously (96).

Lentiviral particles were packaged in HEK 293T cells. shRNA viral particles were used to transduce U2OS cells at a multiplicity of infection (MOI) of 1. Cells were selected using 2 µg/mL puromycin (Clontech). Following confirmation of KD via western blot and immunofluorescence characterization, cells were subsequently transfected with pFUG-RFP LifeAct (MOI 3) and pLVX-AcGFP-Paxillin (MOI 0.5) particles and sorted with a BD Bioscience Influx Flow Cytometer Sorter. U2OS cells are reported to express five palladin isoforms (62), although we were only able to verify the KD of the 140 kDa and 90 kDa isoforms.

Micropatterning

Micropatterns were made as described elsewhere (122,124,135,136). Briefly, plasma-treated coverslips were coated with 10 µg/mL poly-L-lysine grafted to polyethylene glycol (PLL-g-PEG; SuSoS) in 10 mM HEPES, pH 7.4 for 1 hour at room temperature before being illuminated under 180 nm UV (Jelight) light for 15 min though a quartz-chrome mask bearing the micropattern features (FineLine Imaging) designed using AutoCAD (Autodesk). Coverslips were then incubated with 20 µg/mL fibronectin (EMD Millipore) in 50 mM HEPES overnight at 4ºC and washed with PBS prior to cell seeding. To visualize micropatterns, AlexaFluor-647-conjugated fibronectin, at a final concentration of 5 µg/mL was added to the coverslip. To

conjugate AlexaFluor-647 to fibronectin, fibronectin stock solution (1 mg/mL; EMD Millipore) was mixed with AlexaFluor-647 NHS ester (reconstituted at 0.025 mg/mL in DMSO (Sigma), Life Technologies) in carbonate buffer, pH 9.3, overnight at 4ºC. The solution was then passed through a NAP-5 column (GE Healthcare) to separate the conjugated fibronectin.

Western Blot

Cells were lysed in RIPA buffer (Sigma) with phosphatase and protease inhibitors (EMD Millipore) and heated to 70ºC. Samples were run on a 4-12% Bis-Tris gel (Life Technologies) and transferred to a PVDF membrane (Life Technologies). The following primary antibodies were used: rabbit anti-palladin (1:1000; Sigma), rabbit anti-mDia2 (1:750; ProteinTech), mouse anti-GAPDH (1:10000, Sigma). The following secondary antibodies were used: goat anti-mouse HRP-conjugate, goat anti-rabbit HRP-conjugate (both from Life Technologies). HRP-conjugated bands were imaged using enhanced chemiluminescence reagent (ECL, Thermo Fisher).

Immunostaining

Cells were fixed in 4% (v/v) paraformaldehyde (Alfa-Aeser) for 10 min at room temperature and rinsed with PBS. Cells were permeabilized in PBS containing 5% (v/v) goat serum (Thermo Fisher) and 0.5% (v/v) triton-X (EMD Millipore) for 10 min. Cells were blocked in PBS containing 5% (v/v) goat serum for 1-16 h at room temperature or at 4ºC, respectively. Coverslips were incubated with primary antibodies for 2-3 h at room temperature, rinsed with 1% (v/v) goat serum in PBS, and then incubated with secondary antibodies and phalloidin (Life Technologies) for 1-2 h at room temperature in the dark. Cells were rinsed in PBS and mounted using Fluoromount-G (Southern Biotech).

The following primary antibodies were used for immunostaining: mouse anti-vinculin hVin-1 (1:200; Sigma), rabbit anti-di-phosphorylated myosin light chain Thr18/Ser19 (1:200; Cell Signaling Technologies), mouse anti-α-actinin-1 Clone BM 75.2 (1:200; Thermo Fisher), rabbit anti-phosphorylated paxillin Tyr188 (1:200; Cell Signaling Technologies). The following secondary antibodies were used: AlexaFluor 488 anti-rabbit (1:400), AlexaFluor 647 anti-mouse (1:400), phalloidin-AlexaFluor 546 (1:200), all from LifeTechnologies.

Imaging

Unpatterned or micropatterned coverslips were coated with 20 µg/mL fibronectin in 10 mM HEPES, pH 8.5 overnight at 4ºC and rinsed extensively. U2OS cells were seeded at 3000 cells/cm^2 and allowed to adhere for 4-6 h. Prior to imaging, the medium was changed to phenol red-free DMEM (Gibco) supplemented with 10% FBS, 1% nonessential amino acids, 1% penicillin/streptomycin, and 25 mM HEPES (imaging media).

Confocal imaging. For laser ablation and fixed cell studies, an upright Olympus BX51WI microscope (Olympus Corporation) equipped with Swept Field Confocal Technology (Bruker) and a Ti:Sapphire 2-photon Chameleon Ultra II laser (Coherent) was used. The 2-photon laser was set to 770 nm and single SF ablation was performed using three 20 ms pulses. Cells were imaged again at least 20 min after ablation to verify viability and membrane integrity. Live cell imaging was performed using an Olympus LUMPlanFL N 60x/1.0 water dipping objective or an Olympus UPlan FL N 10x/0.3 air objective. Cells were kept at 37ºC using a stage-top sample heater (Warner Instruments). Fixed cell imaging was performed using an Olympus UPlanSApo 60x/1.35 oil immersion objective. Images were captured using an EM-CCD camera

(Photometrics). The following emission filters were used: Quad FF-01-446/523/600/677-25 (Semrock) and 525/50 ET525/50 (Chroma). PrairieView Software (v. 5.3 U3, Bruker) was used to acquire images.

Epifluorescence imaging. For live cell spreading studies, a Nikon Ti-E inverted microscope was used with a 40x/0.75 Ph2 DLL objective and a xenon arc lamp (Lambda LS, Sutter Instrument). The microscope is equipped with a motorized, programmable stage (Applied Scientific Instrumentation) and a stage-top sample heater to maintain optimal humidity, CO_2 levels, and temperature (In Vivo Scientific). Images were acquired using a cooled CCD camera (Photometrics Coolsnap HQ2) and Nikon Elements Software.

Structured Illumination Microscopy (SIM) imaging. Samples were fixed, stained, and mounted as described above. Samples were imaged using a Zeiss Elyra PS.1 structured illumination microscope (Zeiss) and a 63x/1.4 oil DIC M27 objective (Zeiss).

Image analysis

For visualization purposes, contrast was adjusted using FIJI/ImageJ (137,138). To clarify focal adhesion clusters, paxillin or vinculin images were processed with a median filter (0.5 pixels) and a rolling ball background subtraction (12 pixels). To measure ppMLC density along ventral SFs, a line was drawn along a ventral SF between focal adhesions. The intensities along the line in the ppMLC channel were integrated and normalized to the phalloidin integrated intensity. To measure α-actinin-1 intensity, a line was drawn over a ventral SF (including both FAs) and the intensity was measured along that line. FA ends of the ventral SFs were delineated by the phosphorylated-paxillin (pPaxillin) intensity. If necessary, images were stitched together using the Pairwise Stitching plugin in ImageJ (139). Kymographs were generated by drawing a 1-pixel line along the ablated fiber and taking a reslice. Timelapse movies were registered using the Template Matching plugin (136).

To verify that palladin or mDia2 KD resulted in the expected reduction of dorsal SFs or transverse arcs, the number of dorsal SFs along an arc drawn over the curved edge of the crossbow and the number of transverse arcs along a line drawn from the center point of the arc to the innermost transverse arc were quantified. These counts were then divided by the length of the arc or line to obtain the dorsal SF or transverse arc density.

Stress fiber retraction

For SF ablation studies, images were acquired every 1.24 s for 77 s or 155 s. The XY-coordinates of the two severed ends of the SF were manually tracked in ImageJ. The coordinates were used to calculate the half-distance between the severed ends to measure the retraction of one of the severed ends. The half-distance vs. time curve was fitted to the following equation using the curvefit function in MATLAB:

$$L(t) \ = \ L_0 \left(1 - \exp\left(-\frac{t}{\tau} \right) \right) + D_a$$

where L_0 is the stored elastic energy of prestress of the fiber, τ is the viscoelastic time constant, and D_a is the fitted length of the fiber destroyed during ablation (52).

Retraction curves were classified as Kelvin-Voigt (KV) if the fitted curves met all of the following criteria: (1) adjusted $R^2 > 0.9$, (2) viscoelastic time constant $\tau < 0.8$ * imaging window

(i.e. $\tau < 61$ s or < 124 s), and (3) Sum of squared errors of prediction (SSE) < 10. Retractions that failed to meet any of these criteria were classified as non-Kelvin-Voigt (non-KV). Retractions were classified as non-KV/linear if the adjusted R^2 was > 0.9 for a fitted line.

Statistical Analysis

Statistical analyses and graph generation were performed in GraphPad Prism (v 7.00) or using an online calculator in the case of the Fisher Exact test (140). Samples were determined to be non-normal though the Shapiro-Wilk normality test. Non-parametric Kruskal-Wallis tests, followed by a post-hoc Dunn's test for multiple comparisons, were used to assess statistical differences in continuous data sets. In box plots, the top, middle, and bottom of the box represent the 75th, 50th (median), and 25th percentiles, respectively. Bars extend to the 10th and 90th percentiles and the cross depicts the average. The Chi Square test, or the Fisher Exact test, if data set did not meet the requirement for the former, were used to assess differences in the number of KV vs. non-KV SFs.

Chapter 3. Cofilin facilitates remodeling and front-back polarization of tension in stress fiber networks during migration

3.1 Abstract

Cell migration is associated with the establishment of defined leading and trailing edges and the polarization of contractile forces. The actomyosin stress fiber (SF) network plays a critical role in coordinating front-back polarization through the formation of dorsal SFs and transverse arcs in the leading edge lamella, and ventral SFs at the rear. This SF arrangement allows for the cyclic and spatially directed formation and rupture of focal adhesions needed for migration. However, it remains unclear how this mechanical asymmetry is established. In this study, we test the hypothesis that the actin-severing protein cofilin contributes to this symmetry breakage by pruning out low-tension actomyosin subunits during SF maturation. In U2OS cells, we find that of the three SF subtypes, cofilin localizes most prominently to dorsal SFs, which we previously showed do not generate intrinsic tension. Cofilin knockdown (KD) produces abundant SFs that are not organized in a polarized, migratory arrangement. Whereas traction force microscopy indicates that cofilin KD increases whole-cell prestress, single SF laser nanosurgery reveals that individual SFs within cofilin KD cells bear lower prestress, implying that the higher traction forces are due to an accumulation of low-tension SFs. Consistent with this picture, cofilin KD cells have aberrant SF dynamics, with transverse arcs failing to fuse and form smooth, continuous SFs in the lamella. Finally, we find the front-back polarity is not rescued when cofilin KD cells are challenged with a chemokine or cultured on crossbow-shaped extracellular matrix patterns that induce a polarized morphology in control cells. Taken together, these results support a model in which cofilin facilitates the fusion of lower-tension SFs into higher tension SFs, thereby promoting front-back mechanical asymmetry and allowing productive cell migration.

3.2 Introduction

Cell migration is a critical process in many fundamental developmental and pathological processes, including wound healing, embryogenesis, and cancer progression (113). Many cells undergo an adhesion-dependent mesenchymal migration, during which forces generated from the cytoskeleton are transferred to the extracellular matrix (ECM) though focal adhesions (141,142). This migration mode occurs in several distinct steps (143,144). First, a cell establishes front-back polarity, which involves a complex biochemical set of events involving segregation and activation of proteins including Cdc42, PI3K, Rac1, and RhoA (143). Cdc42 restricts the location of the lamellipodia and PI3K activates Rac1 which leads to actin polymerization. The forces produced from this is harnessed to push the membrane in the direction of migration and to stabilize the leading edge (143). At the opposite end of the cell, tension is built up through the assembly of actomyosin stress fiber (SF) bundles, which act to stabilize and define the trailing edge. This tension is subsequently released by disassembling or remodeling SFs, leading to trailing edge retraction (144,145). This cycle of protruding the leading edge, building up tension, and retracting the trailing edge is repeated during directed mesenchymal migration.

Symmetry-breaking through biochemical signaling has been well-studied. However, exactly how the segregation and activity of these molecules translate to mechanical symmetry-breaking is not

well understood. SFs play critical roles in migration by generating traction forces that drive adhesion formation at the leading edge and adhesion detachment at the trailing edge (144,146) and dynamically form, fuse together, and break down as they translocate from the lamella to the rear of the cell (12,45,46). SF subtypes are segregated in specific areas of the cell, with dorsal SFs and transverse arcs found toward the leading edge, and ventral SFs found at the rear of the cell (45,46,114). They are also interconnected: transverse arcs and dorsal SFs are physically coupled together and transverse arcs translocating toward the cell center may also fuse with dorsal SFs positioned at opposite ends to form a single ventral SF (28,46,48,147).

Past work examining the distribution of non-muscle myosin II isoforms A and B (NMM-IIA and NMM-IIB) has shown that SFs at the rear of the cell, that is, ventral SFs, are enriched in NMM-IIB isoform, whereas transverse arcs at the front of the cell are enriched in NMM-IIA (14,25,27). NMM-IIB has been reported to have a higher duty ratio and longer lifetime on SFs compared to the IIA isoform (14), suggesting that the cell spatially organizes tension through the placement of SFs. Our laboratory directly tested this idea using laser nanosurgery; specifically, SFs were severed, and the resulting recoil was tracked as a readout of SF mechanical properties (52,57,63). Peripherally-located SFs are enriched in NMM-IIB and bear higher prestress whereas centrally-located SFs are enriched in NMM-IIA and bear comparatively lower prestress (29,53). Furthermore, disruption of peripheral SFs resulted in a greater dissipation of traction force and larger decreases in cell area (52). In subsequent experiments, we showed that each of the SF subtypes (dorsal, transverse arc, and ventral SFs, which can all be broadly classified as central SFs) have distinct mechanical properties and prestresses. Specifically, dorsal SFs are non-contractile and bear little to no intrinsic prestress, transverse arcs are contractile, with retraction distances dependent on the geometry of the connecting SFs, and ventral SFs are contractile and can bear high prestresses (147). Furthermore, the SF subtypes are highly interconnected, with transverse arcs forming robust connections with and exerting inward radial forces on the non-contractile dorsal SFs. Subtype-specific mechanical properties indicate that the cell spatially organizes tension through the selective placement of SF subtypes. Given the interconnected and dynamic nature of SFs, this also suggests that formation history of the SF can influence its mechanical properties (147).

The polarization and migration processes involve a constant turnover of SFs, with older SFs reinforced, fused together, or broken down to replenish the G-actin pool for incorporation into new F-actin filaments. By extension, the cell undergoes coordinated tensional remodeling depending on where SFs are formed and broken down. For example, EGF-induced front-back polarization is accompanied by increases in the tension borne by the rearmost SF and in the number of connections between the rear SFs. This suggests that cells must increase SF prestress and actively remodel their SF network in preparation for migration (122). How this process is regulated is not well understood. Cofilin, a protein that is involved in the actin recycling process by severing F-actin, has been proposed to play an essential role in the tensional remodeling of SFs, through the tension-dependent recruitment of cofilin to F-actin (148). In support of this idea, purified actin filaments tensed using optical tweezers were found to be resistant to cofilin binding and subsequent depolymerization (149). Evidence of the mechanosensitivity of cofilin has also been seen in cells. In one study, cofilin was found to relocalize from the cytoplasm to SFs when the stretched culture substrate supporting the cells was relaxed (149). Conformational changes in F-actin, either from filament bending or a lack of myosin activity is thought to uncover binding sites for cofilin (149–151). In another line of evidence, cofilin was found to be

enriched on dorsal SFs (48), which have been shown to be under the least amount of prestress of the three SF subtypes (147). Cofilin depletion results in persistent dorsal SFs and a deficiency in the fusion of transverse arcs with dorsal SFs to form ventral SFs (48). These suggest that cofilin participates in the selective removal of low-tension SFs, thereby enriching the cell in higher tension SFs. However, this idea has not been directly measured in living cells.

In this work, we explore the role of cofilin in remodeling and defining the mechanical asymmetry in the SF network. In particular, we test the idea that cofilin is mechanosensitively recruited to sever low-tension SFs while sparing higher-tension SFs. We find that cofilin localizes to low-tension dorsal SFs and that cofilin KD results in an accumulation of SFs. While these accumulated SFs are individually are under lower prestress, they collectively exert higher traction forces at the whole-cell level. Furthermore, transverse arcs in cofilin-depleted cells fail to fuse together during retrograde flow, resulting in decreased contractility: transverse arcs remain thin and form an irregular, nodal network that is under less prestress. In turn, this reduces the cell's ability to break tensional symmetry and migrate in a persistent direction. These results suggest that the process of breaking mechanical symmetry to initiate direction migration is dependent on the ability of the cell to redistribute tension within the cytoskeleton, either by pruning out low-tension SFs by targeting them for depolymerization or by fusing them together to form more contractile SFs.

3.3. Results

Cofilin localizes to dorsal SFs and cofilin KD results in changes in cell morphology.

The actin-severing protein cofilin is a critical regulator of the actin cytoskeleton and is often found in regions of the cell that are undergoing dynamic actin turnover (e.g. lamellipodia). The localization of cofilin could thus indicate regions of high tensional remodeling. In U2OS osteosarcoma cells, we found that a sizeable pool of endogenous cofilin was cytoplasmic and nuclear. However, there was also enrichment of cofilin particularly along dorsal SFs (white arrows, Fig. 3.1a), and to some extent, along ventral SFs and transverse arcs (yellow arrowheads, Fig. 3.1a). This localization is consistent with past findings that dorsal SFs are the subtype that is under the least amount of prestress and the idea that cofilin targets low-tension actin filaments for depolymerization (48,147,149).

To better understand the role of cofilin in our cells, we generated cofilin-1 knockdown (KD) cell lines. KD of cofilin-1 resulted in 70% or greater decreases in cofilin expression and 98% or higher decreases in pCofilin (inactive cofilin) expression compared to control cells transduced with a non-targeting (NT) shRNA (Fig. 3.1b, Appendix II – Fig. S1A). Cofilin-1 is the most abundant isoform of cofilin in non-muscle cells (152) and its KD did not appreciably affect expression levels of ADF, the other cofilin isoform expressed in non-muscle cells (Appendix II – Fig. S1B). Cofilin KD cells had markedly different morphologies, with numerous thin SFs distributed in a disorganized manner (Fig. 3.1C). This observation is consistent with reduced cofilin-severing activity, leading to an accumulation of SFs. Furthermore, we also observed that nuclei of the cofilin KD cells were often multinucleated and/or had nuclei fragments surrounding the nucleus (Fig. 3.1D, shCofilin_1: $p < 0.0001$, shCofilin_3: $p = 0.0003$, Chi Square test). Cofilin KD also increased cell spread area (Fig. 3.1E, shCofilin_1: $p < 0.0001$, shCofilin_3: $p = 0.0265$, Kruskal-Wallis test). The nuclear abnormalities and large cell areas are likely due to failed cell division, as cofilin KD has been reported to impair the formation of the cytokinetic ring in yeast cells (148,153,154); however, the exact mechanism of how cofilin participates in

cytokinetic ring assembly is unknown. Alternatively, the nuclear abnormalities may have arisen from a combination of the accumulation of SFs, which collectively generate large forces, and reduced nuclear structural integrity brought about by the sequestration of actin in the cytoplasm and the concomitant lack of nuclear actin.

Cofilin KD cells contain SFs that are individually under lower prestress but collectively exert higher traction forces

To test the idea that cofilin KD results in an accumulation of SFs that collectively generate larger contractile forces at the cell-scale, we measured the traction forces exerted by RFP-Lifeact transduced cells (Fig. 3.2a). For adherent cells, SFs generate contractile forces which are transmitted to the substrate via focal adhesions. U2OS Cofilin KD cells exerted higher total traction forces at the single cell level (Kruskal Wallis test, shCofilin_1: $p = 0.0060$ and shCofilin_3: $p < 0.0001$, Fig. 3.2b). Given that cell areas of the cofilin KD cells were higher, we also normalized traction forces by the projected area, giving traction stress. Cofilin KD cells also exerted higher traction stresses (Kruskal Wallis test, shCofilin_1: $p = 0.0413$, shCofilin_3: $p = 0.0011$, Fig. 3.2C). Since traction force microscopy measures the overall forces generated, the higher traction forces exerted by the cofilin KD cells could have arisen from one of two mechanisms: (1) an increased number of SFs per cell collectively exerting higher traction forces, or (2) a comparable number of SFs per cell, with each SF exerting higher traction forces. To distinguish between these two possibilities, we experimentally dissipated the tension in SFs using laser nanosurgery. If the force generated per SF is comparable in the cofilin KD and NT cells, then we would expect the retraction distances, a measure of the stored elastic energy, or prestresses, of the SFs, to be similar. On the other hand, if SFs in cofilin KD cells individually exerted higher traction forces, then SFs in the cofilin KD cells would have higher retraction distances.

We first patterned cells onto fibronectin u-shape patterns (122,124), which standardize cell shape and area and provide a framework for the cell to form peripheral SFs with consistent lengths and placements (Fig. 3.3A). We severed the peripheral SF that spanned the gap of the pattern and tracked its retraction over time (Fig. 3.3B). We then fitted the retraction of the SF to a Kelvin-Voigt model, which describes the SF as a viscoelastic material comprised of a series of parallel springs and dashpots (29,52–54,122). From this fitting, characteristic parameters L_o, the stored elastic prestress of the SF, and τ, the viscoelastic time constant or the ratio of viscosity to elasticity, are derived (Fig. 3.3C). We found that the L_o values of SFs in the cofilin KD cells were lower than those in the NT controls (Fig. 3.3D, Kruskal-Wallis test, shCofilin_1: $p = 0.0285$, shCofilin_3: $p < 0.0001$). The lower SF prestresses suggest that cofilin depleted cells are deficient in building up tension in individual SFs. The τ time constants which are a measure of fiber viscoelasticity, were not significantly different across cell lines (Fig. 3.3E). Together with the findings from the traction force studies (Fig. 3.2), these results suggest that individual cofilin KD cells are able to exert higher traction forces due to a sheer increase in the number of low-tension SFs that, when summed together, collectively exert higher traction forces.
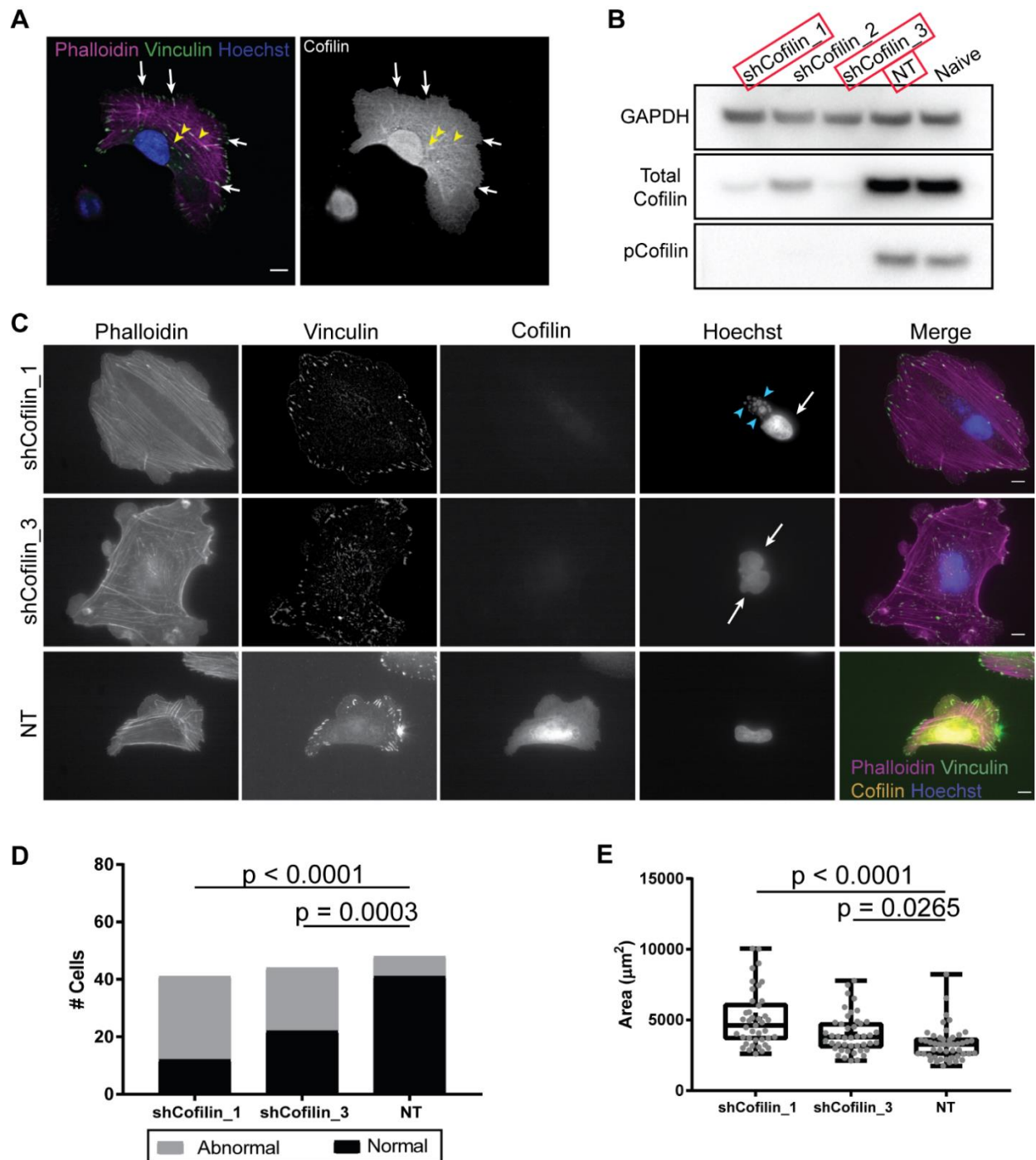
Figure 3.1. Cofilin is enriched along dorsal SFs and cofilin KD cells have altered SF network and nuclear morphologies. (A) Cofilin-1 localizes primarily to the cytoplasm and nucleus of the cell, with some enrichment along dorsal SFs (white arrows) and ventral SFs (yellow arrowheads). (B) Cofilin-1 knockdown reduces both cofilin and pCofilin expression in U2OS cells. Cells transduced with shCofilin_1 and shCofilin_3 shRNA constructs were used in subsequent experiments. (C) Cofilin KD cells are often non-polarized, with multiple protrusions and/or contain multiple nuclei (white arrows) or nuclear fragments (blue arrowheads). Magenta: phalloidin, vinculin: green, cofilin: yellow, Hoechst: blue. (D) Proportion of cofilin KD cells that contain abnormal nuclei, defined as either being multinucleated and/or containing nuclear fragments ("abnormal" shown in gray). (E) Cofilin KD cells have larger projected areas than non-targeting controls. N = 41, 44, and 48 shCofilin_1, shCofilin_3, ant NT cells across 2 independent experiments. Chi-Square test (nucleus morphology) or Kruskal-Wallis post-hoc Dunn's test (cell area). Scale bar: 10 µm.
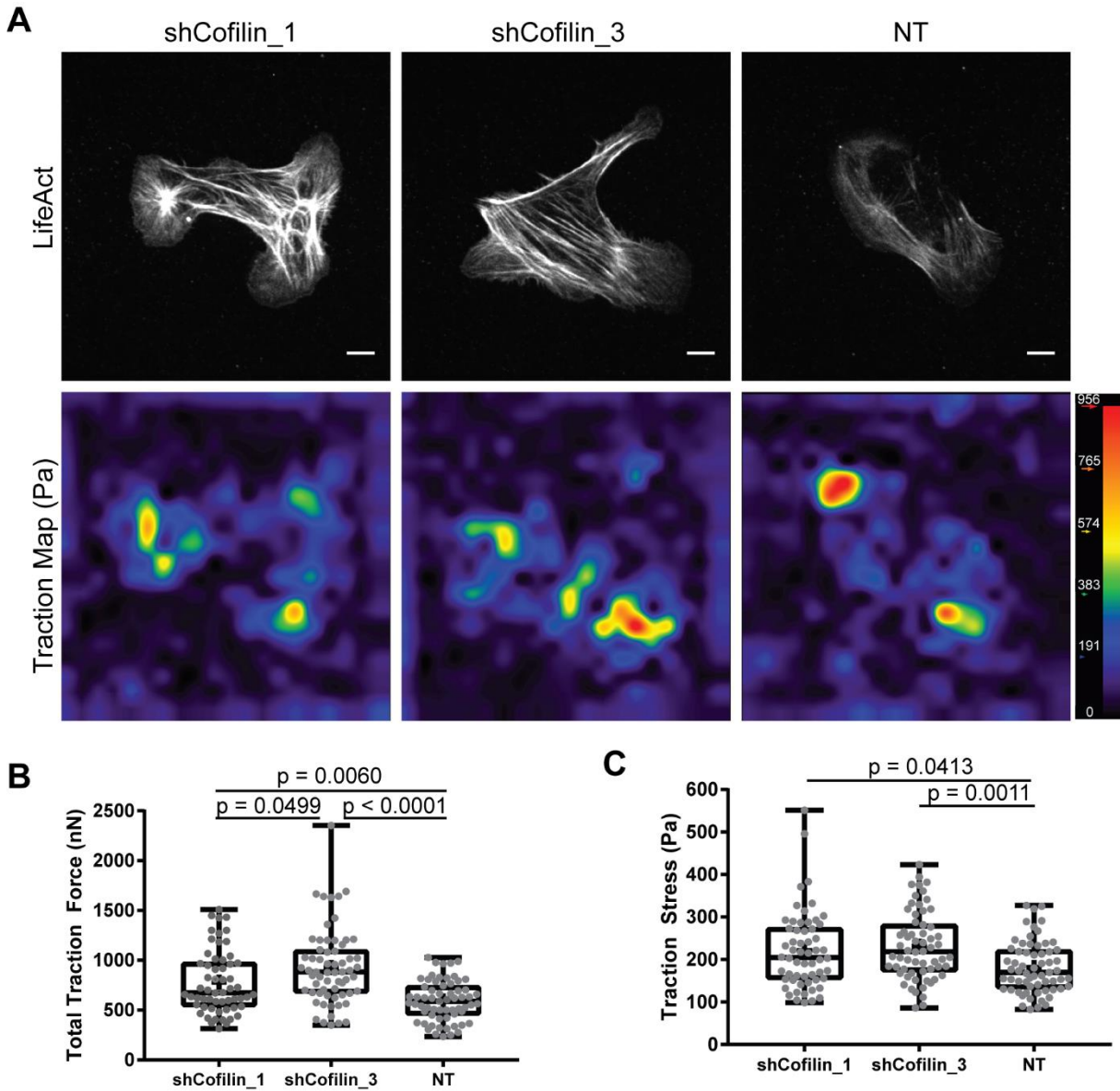
Figure 3.2. Cofilin KD cells generate higher traction forces than NT controls. (A) Top panel: Lifeact images of cells. Bottom panel: corresponding traction maps. (B) Total traction forces exerted by the cells are higher in both KD cell lines. (C). Traction stresses (traction force normalized by cell area) are higher in cofilin KD cells compared to NT cells. Kruskal-Wallis test, post-hoc Dunn's test. N = 58, 63, and 63 cells for shCofilin_1, shcofilin_3, and NT cells from 3 independent experiments. Scale bar: 10 µm.

Cofilin depletion impairs SF fusion transverse arc morphology

Immunofluorescence images (Fig. 3.1), traction force studies (Fig. 3.2), and SF ablation measurements (Fig. 3.3) suggest that cofilin KD cells are accumulating low-tension SFs. Given that cofilin is an actin-severing protein, we next wanted to examine how its depletion would impact SF morphodynamics. To do so, we conducted timelapse studies of RFP-Lifeact transduced cells as they spread and migrated along a uniformly-coated fibronectin glass surface. In NT control cells, transverse arcs formed smooth, continuous transverse arcs that spanned the

36

lamella. Over time, these transverse arcs moved toward the back of the cell and often fused together with adjacent transverse arcs to form thicker SFs (Fig. 3.4a). In contrast, in cofilin-depleted cells, the transverse arcs were jagged and discontinuous and a single SF did not span the entire arc of the lamella (Fig. 3.4a). Often, these transverse arcs formed nodal networks, in which many SFs converged at an intersection point (Fig. 3.4b, inset). Furthermore, unlike transverse arcs in the NT cells, individual transverse arcs in the cofilin KD cells did not undergo fusion and instead translocated toward the center, largely maintaining an even spacing between adjacent SFs (Fig. 3.4a, bottom panel).
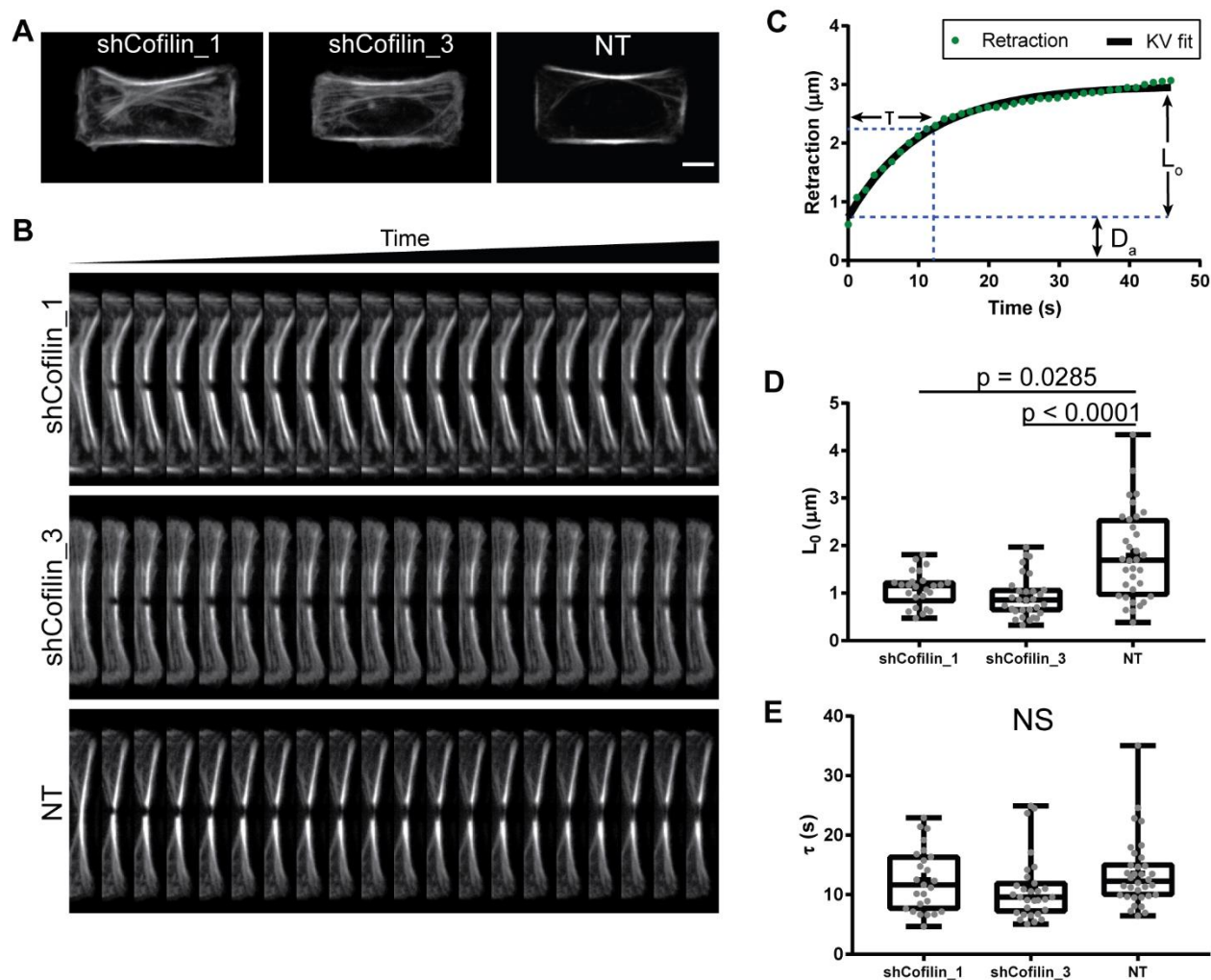
Figure 3.3. Single peripheral SFs in cofilin KD cells exert lower prestresses. (A) Representative images of U2OS cells patterned onto u-patterns. The peripheral SF spanning the gap of the u-pattern was severed. (B) Kymographs of ablated peripheral SF. Time between slices is 1.24 s. (C) Example SF retraction trace tracked over time. Retraction at time t is defined as the half-distance between the severed ends. SF retraction is fitted to the Kelvin-Voigt model. Characteristic parameters L_o (elastic prestress), tau (viscoelasticity), D_a (length of SF destroyed during ablation) are derived from the fitting. (D) Fitted L_o prestresses are lower in cofilin KD cells. (E) Distribution of viscoelastic time constants are not significantly different. Kruskal-Wallis test, post-hoc Dunn's test. N = 25, 30, and 34 shCofilin_1, shCofilin_3, and NT cells across 6-7 independent experiments. Scale bar: 10 μm.
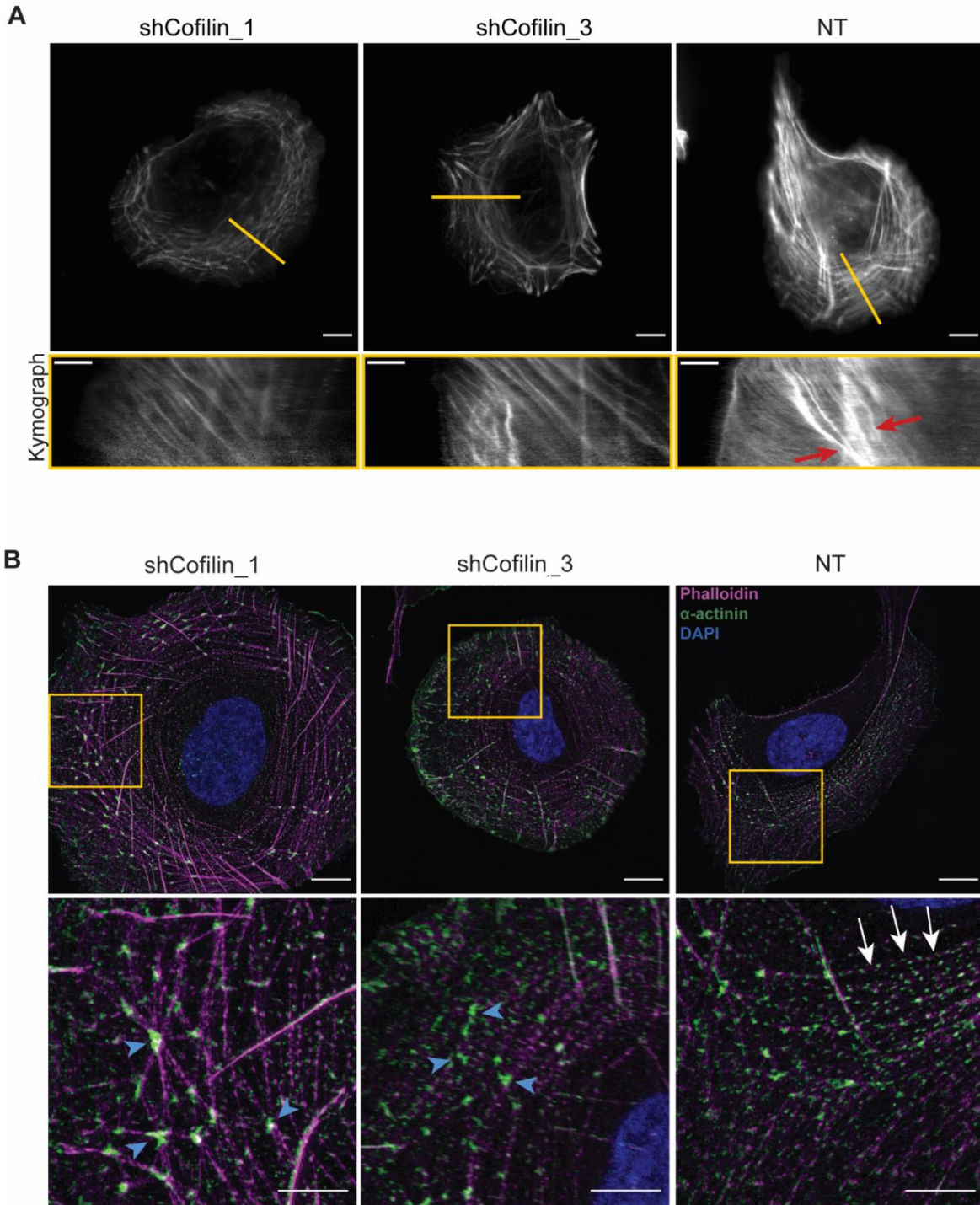
Figure 3.4. Transverse arcs in cofilin KD cells have altered morphodynamics. (A) Transverse arcs in cofilin KD cells are jagged and do not fuse with each other during retrograde SF flow. Yellow line indicates line scan used to generate the kymograph in the bottom panel. Kymographs show movement of transverse arcs toward cell center. Red arrows point to sites of transverse arc fusion. Scale bar, top panel: 10 µm, bottom panel kymograph: 5 µm. Time between slices is 5 minutes. (B) Transverse arcs in cofilin KD cells contain large α-actinin-1 clusters at nodal points where multiple SFs are joined together (blue arrowheads), In NT cells, α-actinin-1 staining is localized to small clusters and is more periodic (white arrows) along the length of the transverse arc. Magenta: phalloidin, green: α-actinin-1, blue: DAPI. Scale bars: 10 µm, ROI: 5 µm.

The temporally-persistent nodes suggested that these areas were comprised of SFs that were robustly connected at these intersection points. Crosslinking proteins, including α-actinin and filamin, are known to be important in bridging actin filaments during the formation of SF bundles and to alternate periodically with NMM-II to form a contractile fiber. Isometric SF contraction is facilitated in part by the regular arrangement of contractile NMM-II and non-contractile crosslinker regions. Thus, examining the crosslinker morphology near the nodes could provide clues about the contractile state in that region. Using structured illumination microscopy (SIM), we found that these nodes were enriched in α-actinin-1, a crosslinking protein that is critical in bundling actin filaments into SFs (Fig. 3.4B). In control cells, α-actinin-1 decorates dorsal SFs continuously, and transverse arcs and ventral SFs in a periodic manner, with bands spaced approximately 1.5 µm apart (Fig. 3.4B, white arrows). Similarly, α-actinin-1 localization along the dorsal SFs and ventral SFs in the cofilin KD cells was continuous and periodic, respectively. Transverse arcs in these cofilin KD cells also contained bands of α-actinin-1, along with larger clusters which were less periodic and spaced at intervals larger than 1.5 µm (Fig. 3.4B, blue arrowheads). These large α-actinin-1 clusters also colocalized to the nodes where multiple SFs were joined together or where transverse arcs intersected with dorsal SFs (Fig. 3.4B).

We speculated that the lack of transverse arc fusion and the irregular crosslinker localization in the cofilin KD cells would result in SFs that are under less prestress. Thicker SFs contain more contractile units, and a periodic, alternating organization with myosin-II is expected to facilitate SF contractility. Thus, the curved, continuous transverse arcs in the NT control cells are expected to bear higher prestresses than the jagged, discontinuous transverse arcs with irregularly-spaced large α-actinin-1 clusters in the cofilin KD cells. Indeed, when we assessed the levels of diphosphorylated myosin light chain (ppMLC), which is the active (contractile) form of NMM-II, we found that that the regions corresponding to the α-actinin-1 clusters were devoid of ppMLC, as expected (Fig. 3.5A, blue arrowheads). This suggests that these nodal regions are discontinuities in the sarcomeric structure of SFs, and in turn, may be deficient in transmitting and/or generating contractile forces. This is because within a sarcomere, NMM-II is thought to slide along F-actin filaments until it collides with α-actinin, and neighboring sarcomeres are known to respond to these forces by contracting (101). Thus, to assess the contractility of transverse arcs, we next severed these SFs in cofilin KD and NT cells and compared their measured retraction distances as a proxy for prestress (Fig. 3.5B). Transverse arcs in the cofilin KD cells were under lower prestress than those in NT controls (Fig. 3.5C, Kruskal-Wallis test, shCofilin_1: p = 0.0272, shCofilin_3: p = 0.0379). This finding lends support to the idea that the nodal regions inhibit transverse arc fusion into thicker, more contractile filaments, and subsequently, an impairment in tension generation.

Lamellar flattening, a hallmark of directed mesenchymal migration, is largely driven by transverse arc contractility being transmitted to orthogonally-connected dorsal SFs (28). Thus, we next asked whether the deficiency in transverse arc contractility would affect cell and lamellar heights. To do so, we took z-stacks of the cell and assessed cell heights, which we measured by taking the distance from the bottom plane of the cell to the top of the nucleus. We found that cofilin KD cells had higher cell heights (Fig. 3.5D-E, shCofilin_1: p = 0.0246, shCofilin_3: p = 0.0075), which is consistent with lower transverse arc contractility and reduced force generation. Furthermore, this suggests that reduced transverse arc contractility and higher cell heights in cofilin KD cells may result in deficiencies in generating a stable leading edge.
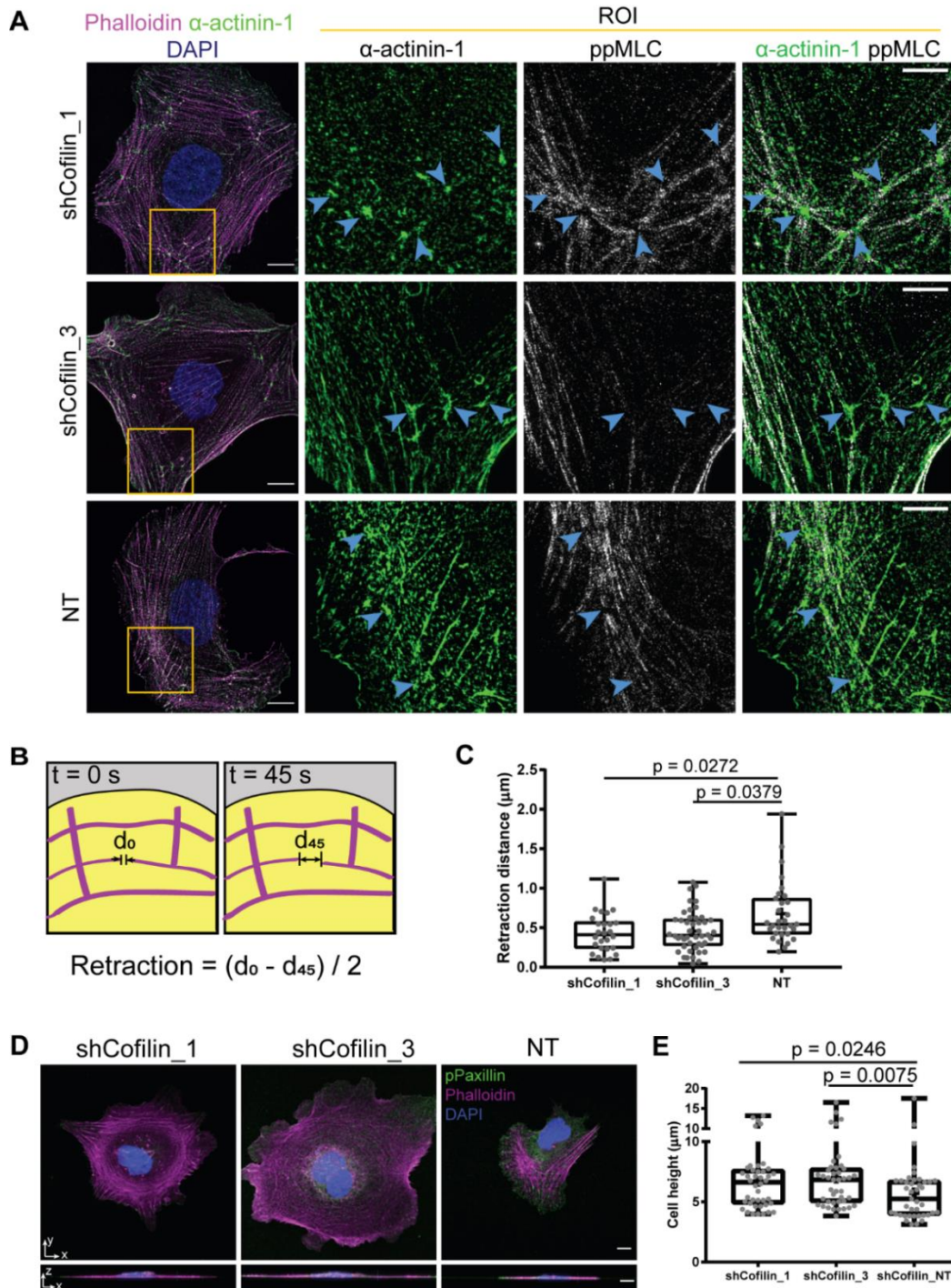
Figure 3.5. Transverse arcs in cofilin KD cells generate lower contractile forces. (A) Jagged, discontinuous transverse arcs in cofilin KD cells form large α-actinin-1 clusters that are devoid of ppMLC (blue arrows). In NT cells, transverse arcs are smooth and continuous, with α-actinin-1 periodically alternating with ppMLC. Scale bar: 10 µm, ROI: 5 µm. Magenta: phalloidin, green: ppMLC, blue: DAPI. (B) Transverse arc retraction is defined as one-half the difference in the distance between severed transverse arc ends 45 s after ablation and immediately after ablation. (C) Distribution of transverse arc prestresses in cofilin KD and NT cells. Kruskal-Wallis, post-hoc Dunn's test. N = 26, 46, and 31 transverse arcs, each from different shCofilin_1, shCofilin_3, and NT cells, across 3-4 independent experiments. (D) Z-stack constructions of cofilin KD and NT cells. Scale bars: 10 µm. (E) Cofilin KD cells have higher nuclear heights compared to NT controls. Kruskal-Wallis, post-hoc Dunn's test. N = 42, 42, and 41 shCofilin_1, shCofilin_3, and NT cells, across 3 independent experiments.

40

Cofilin depletion reduces incidence of cell polarization

In addition to the higher cell heights, we observed that many of the cofilin KD cells did not display polarized SF architectures; that is, transverse arcs orthogonally intersecting with dorsal SFs in the leading edge and ventral SFs in the pointed trailing edge (Fig. 3.1C, 3.4, 3.5). We thus asked whether the cofilin KD cells could be induced to form a polarized SF morphology. Cells were seeded onto a glass surface uniformly-coated with fibronectin and imaged at a time point just after cell attachment to the surface. 100 ng/mL EGF was then dosed into the dish and cell morphology was tracked over the course of 4 or more hours after EGF addition. EGF is a chemoattractant that initiates membrane ruffling and has been shown in the past to induce a polarized SF morphology in cells (122). In NT cells, EGF addition induced membrane ruffling and a majority of the cells tracked exhibited a polarized SF morphology 4 hours after EGF addition (Fig. 3.6A-B). In contrast, a majority of the cofilin KD cells failed to polarize 4 hours after EGF addition (Fig. 3.6B, shCofilin_1: $p < 0.0001$, shCofilin_3: $p < 0.0001$). Many of the cells either remained rounded, with transverse arcs or ventral SFs ringing the cell, or developed multiple dynamic protrusions (Fig. 3.6A). We also seeded cells on adhesive crossbow micropatterns, which have been used in the past to impose a polarized SF arrangement in cells (124,147,155). We found that 65% of the NT cells assessed formed transverse arcs and dorsal SFs in the curved region of the crossbow, indicating that their SFs were arranged in the expected configuration (Fig. 3.6C-D). On the other hand, a majority of the cofilin KD cells did not polarize properly: cells either formed transverse arcs and dorsal SFs in regions beyond the arc, or did not develop them at all (Fig. 3.6C-D, Chi Square test, shCofilin_1: $p < 0.0001$, shCofilin_3: $p < 0.0001$). These results indicate that cofilin KD cells impairs the ability of the cell to polarize, and that a single leading edge cannot be induced by chemoattractant treatment or adhesive patterning.

Finally, we asked whether the deficiencies in lamella flattening and polarization had any consequences for the motility of the cells. For cells to polarize and persistently migrate, they must flatten their lamella and polymerize SFs in the direction of migration. In long-term cell tracking studies, cofilin KD cells had dynamic, ruffled edges, but failed to extend a persistent leading edge. Instead of translocating, these cells ruffled their edges and shifted their nuclei around. Furthermore, the cofilin KD cells had slower migration speeds compared to the NT controls (Fig. 3.6E, Kruskal-Wallis test, shCofilin_1: $p < 0.0001$, shCofilin_3: $p = 0.0003$). Together with the polarization studies, these results indicate that cofilin KD impairs the ability of the cell to generate a stable leading edge, which results in downstream consequences on motility.
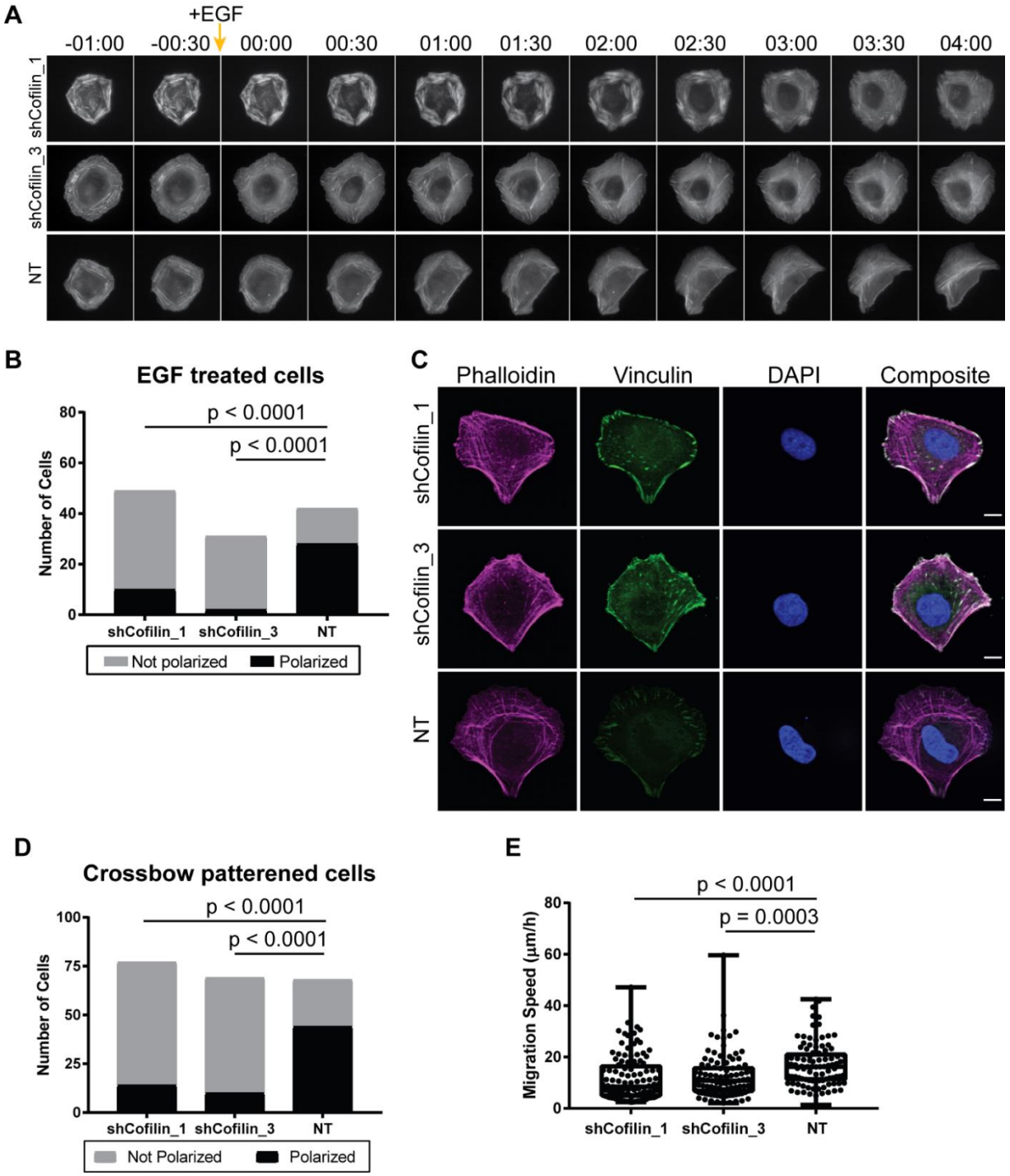
Figure 3.6. Cofilin KD cells do not form a polarized SF arrangement. (A) A series of images depicting cofilin KD and NT cells tracked before and after treatment with EGF to induce a polarized phenotype. (B) Distribution of cells that polarized (developed a single leading edge) 4 hours after treatment with EGF. Chi Square test N = 49, 31, and 42 shCofilin_1, shCofilin_3, and NT cells across 2-3 independent experiments. (C) Representative images of cofilin KD or NT cells patterned on crossbow micropatterns. Scale bar: 10 µm. (D) Distribution of cells that have a polarized arrangement of SFs when seeded on crossbow micropatterns. Chi Square test. N = 77, 69, and 68 shCofilin_1, shCofilin_3, and NT cells across 3 independent experiments. (E) Distribution of random migration speeds. Kruskal-Wallis test, post-hoc Dunn's Test, N = 111, 98, and 96 shCofilin_1, shCofilin_3, and NT cells across 3 independent experiments.

3.4 Discussion

Cells undergo dynamic changes in tension in their SF network during polarization and migration. Cofilin has been proposed to play an important role in this process by mechanosensitively removing low-tension SFs in order to enrich the cell in high tension SFs. This has been based on observations that cofilin localizes to F-actin when it is experimentally untensed using optical tweezers in a reconstituted assay and to SFs in cells upon relaxation of a stretched substrate on which cells are cultured (149). Furthermore, others have observed that cofilin preferentially localizes to dorsal SFs (48), which we have previously shown to be the subtype that is under the least amount of prestress (147). However, it is not clear whether the same mechanosensitive principles apply in the cell and what effects cofilin activity has on the organization of tension in the SF network. Our study addresses these questions by applying laser nanosurgery and live cell tracking to experimentally probe the effects of cofilin depletion on SF tension, dynamics, and building a polarized network. We find that cofilin depletion results in an accumulation of disorganized SFs that are individually under lower tension, but collectively exert higher traction forces which are unproductively leveraged, resulting in an inability to polarize and migrate. Moreover, cofilin depletion results in abnormal transverse arc morphodynamics: transverse arcs form a discontinuous SF interspersed with many crosslinker-rich nodal junctions that prevent the effective generation and transmission of contractile forces and fusion of adjacent SFs into higher contractile SFs. These results indicate that cofilin's roles in the cell include remodeling the SF network, by either removing or concatenating lower tension SFs, ultimately leading to mechanical polarization which is needed for directional migration.

Cofilin may also be important in transverse arc formation. In the cofilin KD cells, we observed aberrant transverse arc properties: α-actinin-1 crosslinkers formed large, irregularly spaced clusters along the length of the SF which likely resulted in the lower amounts of prestresses observed in the laser nanosurgery studies. The crosslinker clusters also corresponded to the junction points where multiple SFs intersected, and prevented fusion of neighboring transverse arcs into thicker SFs in the cofilin KD cells. We propose that the crosslinker clusters result from diminished cofilin activity during transverse assembly. From previous studies, we know that transverse arcs are formed from the annealing of several short Arp2/3-nucleated actin filaments with myosin/tropomyosin complexes into a smooth, continuous SF (50). Our findings suggest that cofilin participates in this process by removing lower-tension branched actin in the Arp2/3-nucleated filaments that are not directly tensed by the non-muscle myosin during arc assembly (Fig. 3.7). These branched actin fragments are persistent in the cofilin KD cells and act as incompressible struts which prevent fusion of neighboring arcs during retrograde SF flow. The crosslinker-enriched nodes correspond to the points where the branched actin meets the main arc. These nodes in turn prevent the effective generation of inward-directed radial contractile forces in the transverse arcs in the cofilin KD cells. Furthermore, this nodal transverse arc network could be an intermediate state that is present during polarization, but is persistent in the cofilin KD cells: analogous nodal F-actin networks are intermediate structures that are observed during contractile ring formation (156) and SF reassembly following treatment and washout of actin depolymerizing agent Latruculin A (157). As is the case with transverse arcs formation, the contractile ring formation is largely thought to be driven by the coalescence of formin-derived actin filaments with myosin-positive nodes into a ring structure. In the cytokinetic ring, the nodes are eventually incorporated into the final contractile ring (156,158,159). Similarly, nodal actin in mammalian cells have been reported to be intermediate structures that serve as template sites for

formin-mediated actin polymerization following treatment with and washout of Latrunculin A (157). These Lifeact-positive nodes lead to aster or geodesic actin networks, which are assumed to generate intermediate levels of tension until SFs can organize into a more contractile network (157,160). Therefore, the transverse arcs in the cofilin KD cells could be arrested in an intermediate state of transverse arc assembly, as cofilin-mediated remodeling is abrogated.

This points to a role of cofilin in generating front-back tensional polarity. SF-tensional symmetry is broken when the rate of transverse arc formation and fusion into thicker SFs increases in one region of the cell, which subsequently results in greater force generation, reinforcement of the leading edge, disassembly of arcs in other regions of the cells, and symmetry-breaking in tension. When cofilin is depleted from the cell, the lack of transverse arc fusion and the nodal network arrangement preclude efficient force generation. As a result, tension is arranged symmetrically and cell remains circular since it is unable to break tensional symmetry. It should be noted that while cofilin KD cells exert higher traction forces due to a sheer increase in the number of SFs in the cell, it is likely that these forces are likely unproductively distributed, i.e., the traction forces are distributed in a way that the cell cannot establish a persistent leading edge. Neither treatment with EGF nor patterning onto crossbow micropatterns, both of which result in a polarized SF architecture in control cells, rescues the polarity defect in cofilin-depleted cells. This inability to polarize subsequently leads to impairments in migration: in long-term tracking studies of cofilin KD cells, we either observed circular cells that ruffled their membrane edges continuously or cells that extended dynamic protrusions in different directions, neither of which resulted in productive cell motility.

Interestingly, in other studies where cofilin-1 and ADF were simultaneously depleted, it was found that there were increased levels of active myosin along single SFs and at the whole-cell level, suggesting increased prestress per SF and an overall higher tensional state (151,161). It was proposed that cofilin/ADF competes with myosin II to bind onto actin filaments, and that depleting both proteins resulted in excessive myosin binding and activation. In our studies, where we directly assessed SF tension, we saw thinner SFs that had lower prestresses per SF, but higher collective force generation. A primary difference between our studies and the previous studies of cofilin and ADF function is that we selectively depleted cofilin-1 only, the primary form found in U2OS cells, with no compensatory upregulation of ADF. Furthermore, in U2OS cells, ADF expression is not as high as cofilin-1, suggesting that cofilin-1 is the primary actin-severing protein (Appendix II – Fig. S1). If both cofilin and ADF compete with NMM-II binding, this could suggest that in our U2OS cofilin KD cells, ADF is binding to actin in compensation for the lowered cofilin expression levels, thereby precluding excessive myosin II binding. However, since ADF expression is not as high as cofilin, there are still morphological changes due to cofilin KD, namely accumulation of SFs due to the lack of fusion or breakdown.
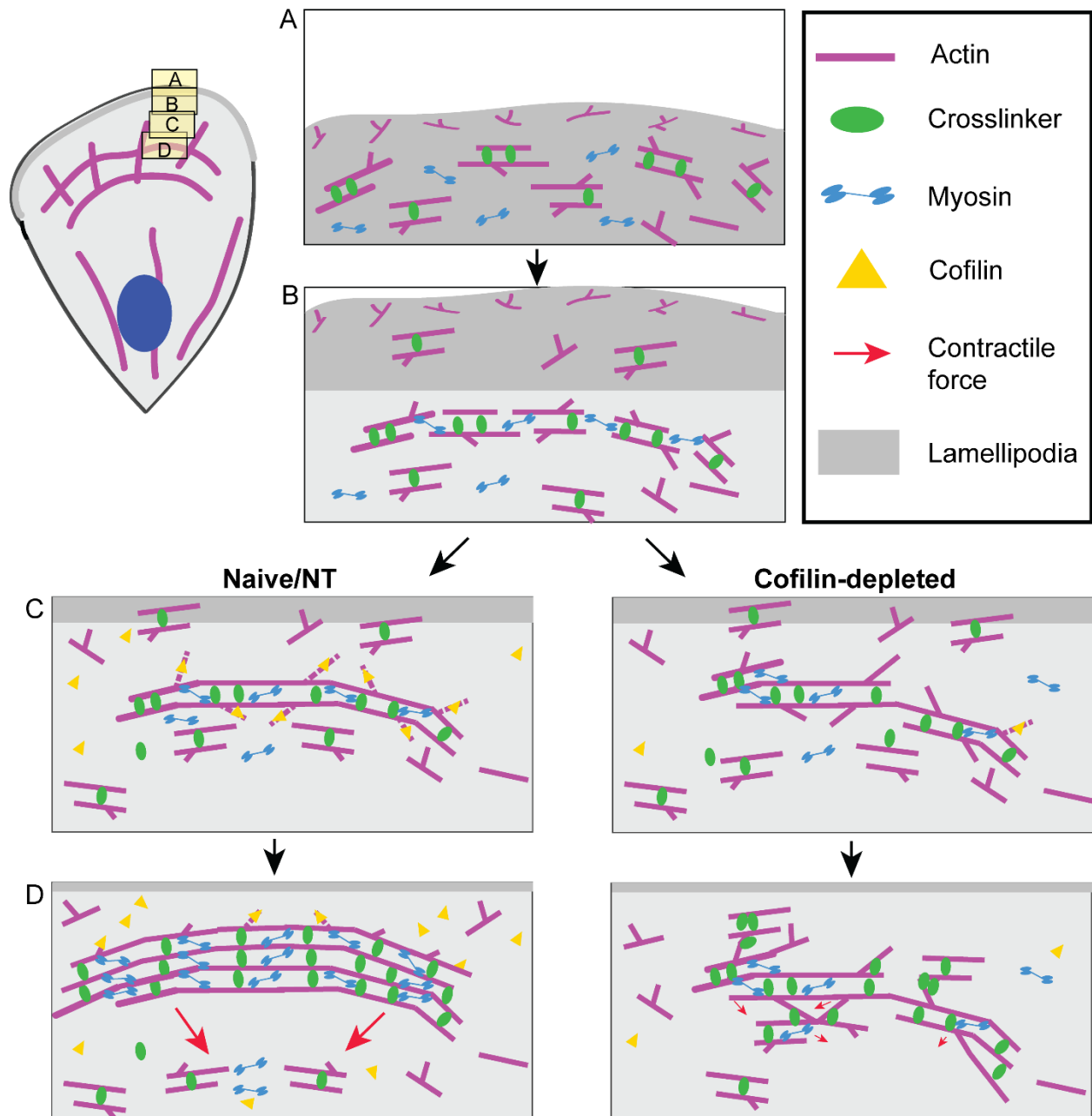
Figure 3.7. **Cofilin is responsible for front-back polarization of tension through selective removal of low tension SFs, either by targeting them for disassembly or by participating in the fusion of SFs into higher tension SFs.** (A) Transverse arcs form from Arp2/3-nucleated (branched) actin filaments and mDia2/tropomyosin/myosin II fragments. (C) Cofilin trims excess, branched actin filaments that are not incorporated directly into the tarc. In cofilin KD cells, branched actin filaments not incorporated into transverse arcs continue to elongate and form connections with other adjacent transverse arcs. (D) Increasing contractility aligns actomyosin fragments into a smooth arc shape. Cofilin trims excess actin filaments to facilitate the formation of a smooth, contractile arc that may fuse with adjacent transverse arcs to form a thicker, more contractile SF, which is able to break the tensional symmetry lead to polarization. In cofilin-depleted cells, persistent branched actin prevents the consolidation of actomyosin filaments into a smooth arc, leading to the formation of nodal, crosslinker-rich junctions in the transverse arc. These junctions prevent effective long-range contractile force generation and fusion of adjacent SFs, leading to unproductive force generation and no polarization.

Our results demonstrate that cofilin plays a critical role in the tensional remodeling of SFs. However, we still do not know how cofilin is able to specifically target the low-tension SFs. In vitro studies of purified actin filaments suggest that the conformation of actin filaments change under low tension or high torsion, resulting in higher cofilin binding (149,150). Furthermore, cosedimentation assays of cofilin, F-actin, and myosin II reveal that cofilin competes with NMM-II for F-actin binding (151). However, it is unclear whether similar principles apply to SFs in cells, which are bundles of actin filaments held together by myosin motor proteins and crosslinking proteins. Finally, an important question is whether the findings presented here hold true in more complex microenvironments, including 3D matrices and compliant substrates. In fibrous 3D matrices, SFs are thinner and tend to follow the fibrous ECM tracks. Future studies exploring the roles of cofilin in these complex environments will offer insight into how tension within SFs are remodeled and how cell shape and migration are regulated.

3.5 Materials and Methods

Cell culture

U2OS cells (ATCC HBT-96) were cultured in DMEM (Gibco) supplemented with 10% FBS (JR Scientific), 1% non-essential amino acids (Gibco), and 1% penicillin/streptomycin (Gibco). Cells were tested for mycoplasma every three months and authenticated via short tandem repeat profiling.

Cloning and cell line generation

We used shRNA constructs targeting the cofilin-1 isoform (shCofilin_1: 5' - ACGACATGAGGTGCGTAAGT - 3', shCofilin_2: 5' – CCAGATAAGGACTGCCGCTAT - 3', shCofilin_3: 5' - AAGGAGGATCTGGTGTTTATC - 3'. A non-targeting sequence (NT: 5' – GCTTCTAGCCAGTTACGTACA - 3') was also included as a control. Each oligonucleotide was inserted into the pLKO.1-TRC cloning vector (Addgene plasmid # 10878) using AgeI and EcoRI (134) and verified by sequencing. RFP-LifeAct was cloned into the pFUG vector as described previously (96).

Lentiviral particles were packaged in HEK 293T cells. shRNA viral particles were used to transduce U2OS cells at a multiplicity of infection (MOI) of 1. Cells were selected using 2 µg/mL puromycin (Clontech). Following confirmation of KD via western blot and immunofluorescence characterization, cells were subsequently transduced with pFUG-RFP LifeAct (MOI 3).

Western Blot

Cells were lysed in RIPA buffer (Sigma) with phosphatase and protease inhibitors (EMD Millipore) and heated to 70ºC. Samples were run on a 4-12% Bis-Tris gel (Life Technologies) and transferred to a PVDF membrane (Life Technologies). The following primary antibodies were used: rabbit anti-cofilin (1:1000; Cell Signaling Technologies, D3FP XP), rabbit anti-phosphorylated Cofilin (1:1000; Cell Signaling Technologies, Ser3 77G2), mouse anti-GAPDH (1:10000, Sigma). The following secondary antibodies were used: goat anti-mouse HRP-conjugate, goat anti-rabbit HRP-conjugate (both from Life Technologies). HRP-conjugated bands were imaged using enhanced chemiluminescence reagent (ECL, Thermo Fisher).

Immunostaining

Cells were rinsed briefly with DPBS and then fixed in 4% (v/v) paraformaldehyde (Alfa-Aeser) for 10 min at room temperature. Cells were permeabilized for 10 minutes in 0.3% (v/v) triton-X (EMD Millipore) diluted in PBS containing 5% (v/v) goat serum (Thermo Fisher) for 10 min. Cells were blocked in PBS containing 5% (v/v) goat serum for 16 h at 4 °C. Coverslips were incubated with primary antibodies for 2 h at room temperature, rinsed with 1% (v/v) goat serum in PBS, and then incubated with secondary antibodies and phalloidin (Life Technologies) for 1 h at room temperature in the dark. Nuclei were stained with Hoechst (1:500, Thermo Fisher) or DAPI (1:500, Sigma). Cells were rinsed in PBS and mounted using Fluoromount-G (Southern Biotech).

The following primary antibodies were used for immunostaining: mouse anti-vinculin hVin-1 (1:200; Sigma), rabbit anti-di-phosphorylated myosin light chain Thr18/Ser19 (1:200; Cell Signaling Technologies), mouse anti-α-actinin-1 Clone BM 75.2 (1:200; Sigma), rabbit anti-cofilin (1:200, Cell Signaling Technologies, D3F9 XP), rabbit anti-cofilin (1:200, Abcam ab11062). The following secondary antibodies were used: AlexaFluor 488 anti-rabbit (1:400), AlexaFluor 647 anti-mouse (1:400), phalloidin-AlexaFluor 546 (1:200), all from Life Technologies.

Micropatterning

Micropatterns were made as described previously (122,124,135,136,147). Briefly, plasma-treated coverslips were incubated with 10 µg/mL poly-l-lysine conjugated to polyethylene glycol (PLL-g-PEG; SuSoS) in 10 mM HEPES, pH 7.4 for 1 h at room temperature. The coverslips were rinsed briefly with PBS and deionized water. Coverslips were placed on a quartz-chrome photomask bearing the micropattern features (Front Range Photomask) which were designed using AutoCAD (Autodesk). The assembly was then illuminated under 180 nm UV light (Jelight) for 15 minutes. Coverslips were rinsed briefly with PBS.

Imaging

Unpatterned or micropatterned coverslips were coated with 20 µg/mL fibronectin (EMD Millipore) in 100 mM bicarbonate solution, pH 8.5, overnight at 4°C and rinsed extensively. U2OS cells were seeded at 3000-5000 cells/cm^2 and allowed to adhere for 4-6 h before imaging. Prior to imaging, the medium was changed to phenol red-free DMEM (Gibco) supplemented with 10% FBS, 1% nonessential amino acids, 1% penicillin/streptomycin, and 25 mM HEPES (imaging media).

Confocal imaging. For laser ablation and fixed cell studies, an upright Olympus BX51WI microscope (Olympus Corporation) equipped with Swept Field Confocal Technology (Bruker) and a Ti:Sapphire 2-photon Chameleon Ultra II laser (Coherent) was used. The 2-photon laser was set to 770 nm and single SF ablation was performed using three 20 ms pulses. Cells were imaged again at least 20 min after ablation to verify viability and membrane integrity. Live cell imaging was performed using an Olympus LUMPlanFL N 60x/1.0 water dipping objective. Cells were kept at 37°C using a stage-top sample heater (Warner Instruments). Fixed cell imaging was performed using an Olympus UPlanSApo 60x/1.35 oil immersion objective. Images were captured using an EM-CCD camera (Photometrics). The following emission filters were used:

Quad FF-01-446/523/600/677-25 (Semrock) and 525/50 ET525/50 (Chroma). PrairieView Software (v. 5.3 U3, Bruker) was used to acquire images.

<u>Epifluorescence imaging</u>. For live and fixed cell imaging studies, a Nikon Ti-E inverted microscope was used with a 60x/1.40 Plan Apo VC objective and a xenon arc lamp (Lambda LS, Sutter Instrument). The microscope is equipped with a motorized, programmable stage (Applied Scientific Instrumentation) and a stage-top sample heater to maintain optimal humidity, CO2 levels, and temperature (In Vivo Scientific). Images were acquired using a cooled CCD camera (Photometrics Coolsnap HQ2) and Nikon Elements Software.

Traction force microscopy

Coverslips were cleaned briefly with 70% ethanol and plasma treated for 5 minutes before being incubated with a silanization solution consisting of 5% acetic acid and 0.3% bind-silane in 100% ethanol. Polyacrylamide gels were synthesized with 5% acrylamide, 0.2% bis-acrylamide, 1% ammonium persulfate, 0.1% tetramethylethylenediamine (TEMED), and 1.5 % 0.2 µm-diameter dark red fluorescent microspheres. 0.0001% 2-pyridinecarboxaldehyde was added to the precursor solution just prior to gel polymerization for subsequent fibronectin conjugation (96). A drop of the precursor solution was polymerized between a silanized coverslip and a glass surface treated with a hydrophobic solution (RainX). The final gel height is approximately 75 µm. Following polymerization, the gels were carefully removed from the hydrophobic surface and rinsed extensively in PBS. Gels were then incubated with 20 µg/mL fibronectin (EMD Millipore) in 100 mM bicarbonate solution, pH 8.5, overnight at 37ºC and rinsed extensively. U2OS RFP-Lifeact cells were seeded at 2500 cells/cm^2 and allowed to adhere for 4-6 hours before imaging. Prior to imaging, media was changed to phenol red-free imaging media. Images of the fluorescent microspheres and the cells were acquired before and after treatment with a 2% sodium dodecyl sulfate solution to remove cells. We computed maps of cellular traction stresses from bead positions before and after cell detachment using Fourier transform traction cytometry implemented using a modified ImageJ plugin (162). Total traction forces were measured by summing the traction forces over the cell area.

Image analysis

For visualization purposes, image contrast was adjusted using FIJI (137,138). Kymographs were generated by drawing a 1-pixel line perpendicular to the flow of transverse arcs and taking a reslice. Timelapse movies were registered using the Stack Reg plugin (163) and corrected for photobleaching using the BleachCorr function.

Stress fiber retraction

For SF ablation studies, images were acquired every 1.24 s for 77 s. The XY-coordinates of the two severed ends of the SF were manually tracked in ImageJ. The coordinates were used to calculate the half-distance between the severed ends, giving the retraction of one of the severed ends. The half-distance vs. time curve was fitted to the following equation using the curvefit function in MATLAB:

$$L(t) \; = \; L_0 \left(1 - \exp\left(-\frac{t}{\tau} \right) \right) + D_a$$

where L_0 is the stored elastic energy of prestress of the fiber, τ is the viscoelastic time constant, and D_a is the fitted length of the fiber destroyed during ablation (52).

Transverse arc prestress was measured by subtracting the distance between the severed ends at 45 s and the distance between the SF ends at 0 s and dividing by 2.

Cell Height Analysis

Z-stack images with 0.5 µm-spacing were acquired and reconstructed in ImageJ. Heights were manually measured from the base of the cell to the highest point.

Polarization Analysis

Unpatterned cells were classified as polarized if the cell had a single lamella containing transverse arcs and dorsal SFs. Rounded cells with transverse arcs and dorsal SFs ringing the cell were classified as unpolarized. Cells on crossbows were classified as polarized if dorsal SFs and transverse arcs were present along the curved arc of the pattern.

Migration Analysis

Phase contrast images of cells were acquired every 10 minutes for at least 6 h. The centroid of the cell was tracked using the Manual Tracking plugin in ImageJ to obtain the frame-to-frame instantaneous speed. These instantaneous speeds were averaged over a 6 h window to obtain the average migration speed of the cell.

Statistical Analysis

Statistical analyses and graph generation were performed using GraphPad Prism (v 7.00). Samples were determined to be non-normal through the Shapiro-Wilk normality test. Non-parametric Kruskal-Wallis tests, followed by a post-hoc Dunn's test for multiple comparisons, were used to assess statistical differences in continuous data sets. In box plots, the top, middle, and bottom of the plot represent the 75th, 50th (median), and 25th percentiles, respectively. The average is represented by the cross. Bars extend to the maximum and minimum value of the data set. The Chi Square test was used to assess differences in the distributions of polarized vs. non-polarized cells.

3.6 Acknowledgements

Chapter 4. Extracellular matrix dimensionality and curvature influence stress fiber architecture and mechanics

4.1 Abstract

Cells migrating throughout the body may interact with extracellular matrix (ECM) structures that vary in their adhesive properties, mechanics, and geometry, all of which are known to influence cytoskeletal architecture, cell shape, and migration. Curvature is a geometric property that has not been extensively studied due to limitations in fabricating reproducible substrates with curvatures relevant to cells. Recent work has shown that the degree of curvature acutely affects overall migration behavior and the orientation and alignment of apical and basal stress fibers (SFs), which differ in their location in the cell. However, it is unknown what mechanical functions apical and basal SFs have and whether those change when substrate geometry is altered. In this study, we probe the mechanical properties of apical and basal SFs and their roles in shaping the cell. We find that apical SFs are not universally expressed at the same frequency across different cell lines. Furthermore, despite their known connections with the nucleus, we do not find any correlation between the presence of organized apical SFs and nuclear morphology, suggesting that the function of apical SFs is not to shape the nucleus. When cells are cultured on fibronectin microlines of varying widths, we find that apical SFs are not as commonly expressed on thin, 2 µm-wide microlines as they are when the cells are cultured on wider 50 µm-wide microlines. Next, to better understand the mechanical roles of apical and basal SFs, we used laser nanosurgery to sever SFs and measure their retraction dynamics. We find that apical SFs have longer lengths and are under higher prestresses than basal SFs. These observations also hold true for apical and basal SFs in cells are cultured on curved substrates. Taken together, our results show that the presence of apical SFs does not correlate with nucleus shape. However, apical SFs may be still be important in transmitting large stresses from the ECM to the nucleus and positioning the nucleus when the cell is placed on a challenging microenvironment.

4.2 Introduction

A cell may interact with chemically-, mechanically-, and topographically-varied surfaces as it migrates from one region of the body to another. These extracellular matrix (ECM) features may all influence location and size of focal adhesions, internal cytoskeletal architecture, cell fate, and migration speed. Past studies of cell migration have primarily focused on the influences of chemical (e.g. ligand type and density) and mechanical (e.g. stiffness) ECM properties on cell function. These works have yielded many important insights into how cells process the biophysical properties of the extracellular matrix. For example, there is a biphasic relationship between fibronectin concentration and migration speed, with intermediate concentrations of fibronectin promoting the fastest migration speeds (164,165). Furthermore, cells on mechanically stiffer ECMs can migrate faster than cells on a more compliant substrate due to the ability of the substrate to resist cell-generated forces which are needed for effective migration (8,9). Studies of cell interactions with varied topographies have primarily focused on the alignment behavior of neurons or other cells in channel grooves of varying heights (166,167). However, another

geometric property, curvature, has not been extensively studied, despite the prevalence of curved features found throughout the body (e.g. vasculature, intestinal villi, lung alveoli, and large collagen bundles) (168). This has largely been due to technological limitations in fabricating reproducible substrates with relevant degrees of curvature at the cell scale. However, there is a need to understand how the topographical properties of the cell-scale microenvironment influence cytoskeletal architecture, which ultimately can determine the overall cell shape and migration at shorter time scales, and gene expression and cell fate at longer time scales.

Recent work has shown that cell-scale curvature strongly influences the organization of the actomyosin stress fiber (SF) network. For example, cells cultured on borosilicate microcapillary tubes of defined radii have different apical and basal SF orientations depending on the degree of curvature. Apical and basal SFs are both connected to focal adhesions (FAs) at both ends, but apical SFs arc upward over the nucleus, whereas basal SFs are aligned close to the bottom surface. Cells adhered on microcapillary tubes with high curvatures (40 µm radius microcapillaries), preferentially oriented basal SFs in the circumferential direction, whereas apical SFs were oriented along the axial direction of the microcapillary (i.e. along the length of the microcapillary), perpendicular to the basal SFs. This preferential orientation of basal and apical SFs was lost when cells were cultured on larger 125 µm radius microcapillaries (169). Similarly, the alignment of apical and basal SFs depended on the degree of curvature when cells were cultured on microfabricated sphere-with-skirt (SWS) surfaces with defined, smoothly varying degrees of curvatures (170). However, it is unclear whether the preferential arrangement of apical and basal SFs has a specific structural or mechanical role in shaping the cell when it interacts with a curved surface.

Groups of apical SFs that run over the nucleus and physically anchor the nucleus to the ECM form a perinuclear actin cap. Linkers of the nucleoskeleton and cytoskeleton (LINC) complexes mediate the connection between the actin cap and the nucleus, suggesting that these apically-located SFs may be important in translating biophysical ECM cues to the nucleus and/or shaping the cell (171,172). These SFs are spatially and behaviorally distinct from other SF subpopulations – dorsal, transverse arc, and basal ventral SFs – which are found primarily on the bottom portion of the cell. Within the dorsal, transverse arc, ventral SFs subtype classification system, both apical and basal SFs may be classified as ventral SFs since both types are anchored to FAs at both ends. However, the FAs associated with the apical SFs are more dynamic and have larger areas than FAs associated with other SFs. Furthermore the apical SFs contain higher levels of phosphorylated myosin light chain (pMLC), which suggests that they are under greater tension than basal SFs (173).

Like many SFs in migrating cells, apical SFs are highly dynamic. However, apical SFs are also transient: they are not present until a specified period has elapsed following cell division, and may also appear following stem cell differentiation and after an epithelial to mesenchymal transition (174–176). Apical SFs are more commonly observed in some cell types, including fibroblasts (3T3, MEF, HFF) and endothelial cells (HUVEC). In other cell lines, including U2OS osteosarcoma, MCF-7 mammary adenocarcinoma, undifferentiated stem cells, and cells in epithelial sheets, and laminopathic cells, apically-located SFs are rarer and are not as regularly

organized or identifiable (173,174). This suggests that apically-located SFs may have a transient purpose in mechanosignaling during migration (171,174,177–179).

A majority of the studies on the function of apical and basal SFs have been done on cells cultured on flat coverglasses. It is unclear whether apical SFs are mechanically distinct from basal SFs. Furthermore, the changing orientation of apical SFs with respect to basal SFs on different curvature substrates and their presence in cells cultured on thin-width microlines raises the intriguing possibility that the formation of apical SFs is promoted by certain geometric cues. In this study, we combine different substrate geometries with laser nanosurgery to measure the mechanical properties of apical and basal SFs. We find that apical SFs are not universally expressed at the same frequency across different cell lines and that their presence does not correlate with nuclear morphology. Furthermore, apical SFs are longer in length and are under higher prestress than basal SFs; these trends also hold true when cells are cultured on curved substrates. Together, these results indicate that the presence of apical SFs does not correlate to nuclear morphology, but may have a role in transmitting stresses to and positioning the nucleus.

4.3 Results

The presence of apical SFs is not correlated with nucleus shape and height

Apical SFs are reported to be transiently present in cells (174). We thus wanted to assess whether there were morphological differences between cells with and without apical SFs. To do so, we screened a panel of cells and assessed the proportion displaying apical SFs. NIH 3T3 fibroblasts, mouse embryonic fibroblasts (MEFs), U2OS osteosarcoma, and U251 glioblastoma cells were cultured on glass coverslips uniformly coated with fibronectin and were fixed and stained to examine their SF architecture and nuclear shape (Fig. 4.1A). We took z-stack images of the cells to distinguish between SFs on the apical (top) and basal (bottom, near the ECM) planes. Of the four cell lines, a majority of the 3T3 and MEF cells displayed both basal SFs and apical SFs. Apical SFs were oriented parallel to one another and ran over the nucleus (white arrowheads, Fig. 4.1A). 3T3 cells were often elongated, with apical SFs spanning the long axis of the cell, and basal SFs approximately oriented orthogonally and aligned with the short axis. MEF cells exhibited varied morphologies, either elongated (similar to the 3T3 cells), or circular, with basal SFs and apical SFs arranged roughly normal to each other (Fig. 4.1A). For both these cell lines, 80% or more of the cells surveyed displayed apical SFs. On the other hand, U2OS and U251 cells had different morphologies compared to the 3T3s and MEFs. Both U2OS and U251 cells had fan-shaped morphologies which are a hallmark of mesenchymal-migrating cells. Transverse arcs and dorsal SFs were found in the lamella and basal ventral SFs were located at the rear of the cell. Furthermore, the proportion of U2OS and U251 cells containing apical SFs was significantly lower than in the 3T3s and MEFs (Fig. 4.1B, Appendix III – Fig. S1, Chi Square test, p < 0.05). While a small number of U2OS and 3T3 cells had apically-located SFs, they did not form the neatly parallel arrangement seen in the 3T3 and MEF cells: apically-located SFs either intersected with one another at the top of the nucleus or formed several SFs that were not completely parallel over the nucleus (white arrowheads, Fig. 4.1A).
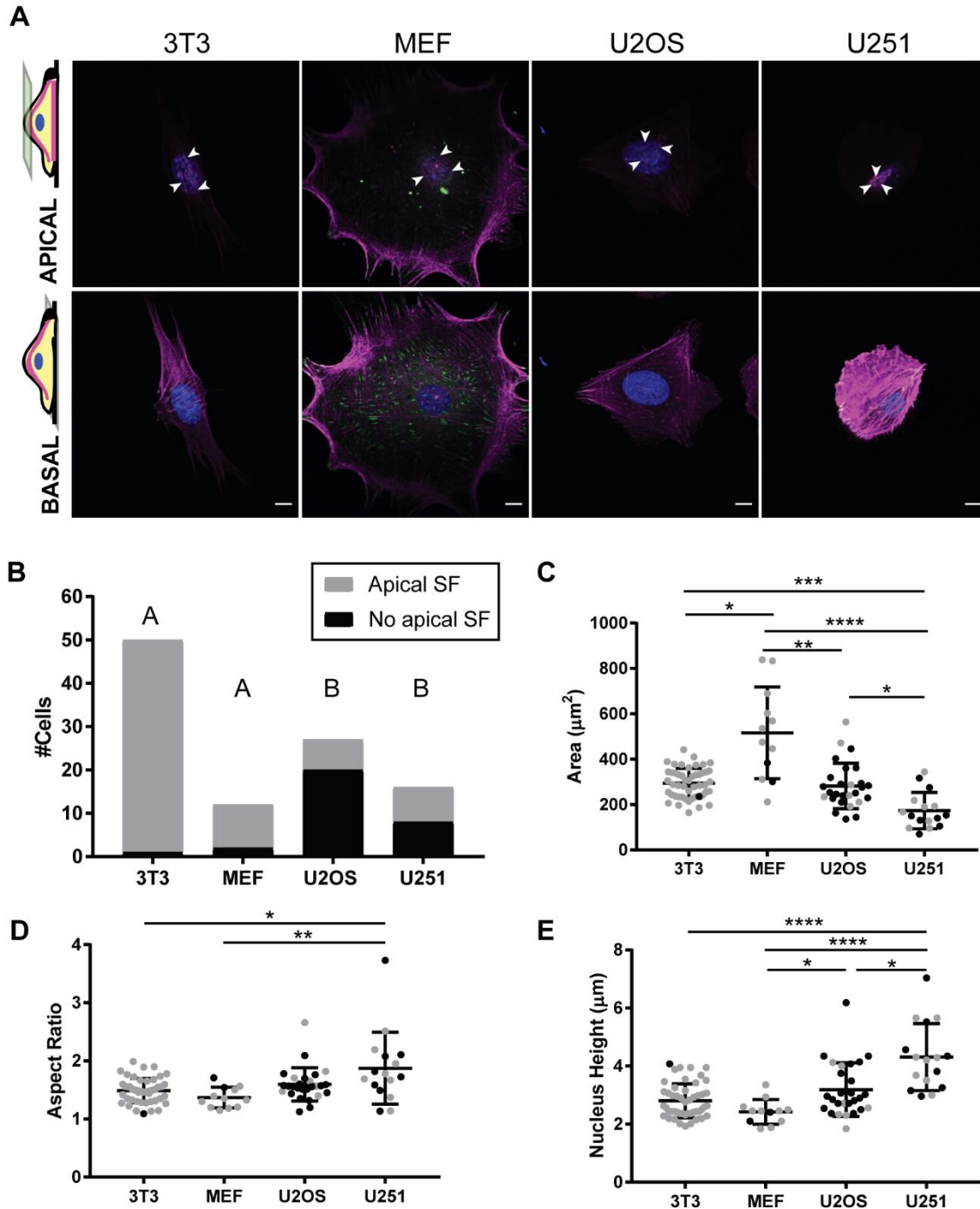
Figure 4.1. Nuclear morphology is not correlated with the presence of apical SFs. (A) Representative images of NIH 3T3, MEF, U2OS, and U251 cells stained for actin (phalloidin, magenta), vinculin (green), and nuclei (blue). Top and bottom rows show the z-slice at the apical or basal surface, respectively. White arrowheads point to apically-located SFs. Scale bar: 10 µm. (B) Proportion of cells assessed displaying apical SFs (gray) or not displaying apical SFs (black). Chi Square test; A vs. B statistical families: $p < 0.0001$. (C) Distribution of projected nuclear areas. (D) Distribution of projected nuclear aspect ratios. (E) Distribution of nucleus heights as measured from XZ-plane reconstructions. Points in gray in (C-E) indicate cells displaying apical SFs. Kruskal-Wallis test, post-hoc Dunn's test; * $p < 0.05$, ** $p < 0.01$, *** $p < 0.001$, **** $p < 0.0001$. N = 49 3T3, 12 MEF, 27 U2OS, and 16 U251 cells across 1-2 independent experiments.

Apical SFs are positioned over the nuclei and are reported to be mechanically connected to the nucleus via the LINC complex. We thus asked whether their presence influenced the morphology of the nuclei. If apical SFs play a role in shaping the nucleus by exerting forces, then their presence would be expected result in changes in nuclear morphology, including larger projected areas, higher aspect ratios, and lower cell heights. We found that the projected nuclear areas varied across cell lines, with the MEFs having the largest nuclear areas ($p < 0.05$) and the U251 cells having the smallest areas ($p < 0.05$, Fig. 4.1C). However, within any one cell line, there did not appear to be any relationship between the presence of apical SFs (indicated by gray circles in plots) and projected nuclear area (Fig. 4.1C). Similarly, while nuclear aspect ratios and nucleus heights may have differed between cell lines, there was neither a correlation between the presence of apical SFs and nuclear aspect ratio nor one between the presence of apical SFs and nucleus height (Fig. 4,1D-E). Taken together, these data indicate that in U2OS and U251 cells, the presence of apical SFs does not correlate with changes in nuclear morphology. However, any relationships between the presence of apical SFs in 3T3 and MEF cells and nuclear morphology is unclear, as a vast majority of the cells within these lines had robust populations of apical SFs.

Cells on microlines deform their nuclei

Apical SFs are reported to be prevalent in cells that are cultured on thin-width microlines (178) and curved substrates (169,170). We thus asked whether apical SFs were formed in response to adhesive restrictions. To answer this question, we cultured two cell lines, 3T3 cells and U2OS cells, on fibronectin microlines of varying widths. The 3T3 and U2OS cell lines were chosen because they do and do not commonly display organized apical SFs when cultured on 2D substrates uniformly coated with an ECM, respectively. If apical SFs are formed in response to increasingly constrained adhesion sites, then the frequency of U2OS cells with apical SFs would be expected to be higher when the cells are cultured on thin-width microlines that restrict cell spreading along one axis. On 2 µm-wide microlines, the thinnest and most restrictive patterns, we found that a majority of 3T3 and U2OS cells did not form apical SFs (Fig. 4.2A-B, Appendix III – Fig. S2). The few cells with apically-located SFs often arranged them irregularly over the nucleus (Fig. 4.2A, white arrowheads), and there were no overall morphological differences between cells with and without apical SFs. However, on the 10 and 50 µm-wide microlines, a large proportion of 3T3 cells displayed apical SFs, suggesting that apical SFs were able to form and had a role in shaping the cell. As was the case on the uniformly-coated fibronectin coverslips, U2OS cells rarely displayed apically-located SFs when cultured on the 2, 10, and 50 µm-wide microlines (Fig. 4.2A-B). The U2OS cells with apically-located SFs did not regularly arrange them over the nucleus. These results suggest that the 2 µm-wide microlines are too restrictive to support the formation of apical SFs, whereas the 10 and 50 µm-wide microlines can support formation of apical SFs in cell lines that regularly display this SF type.
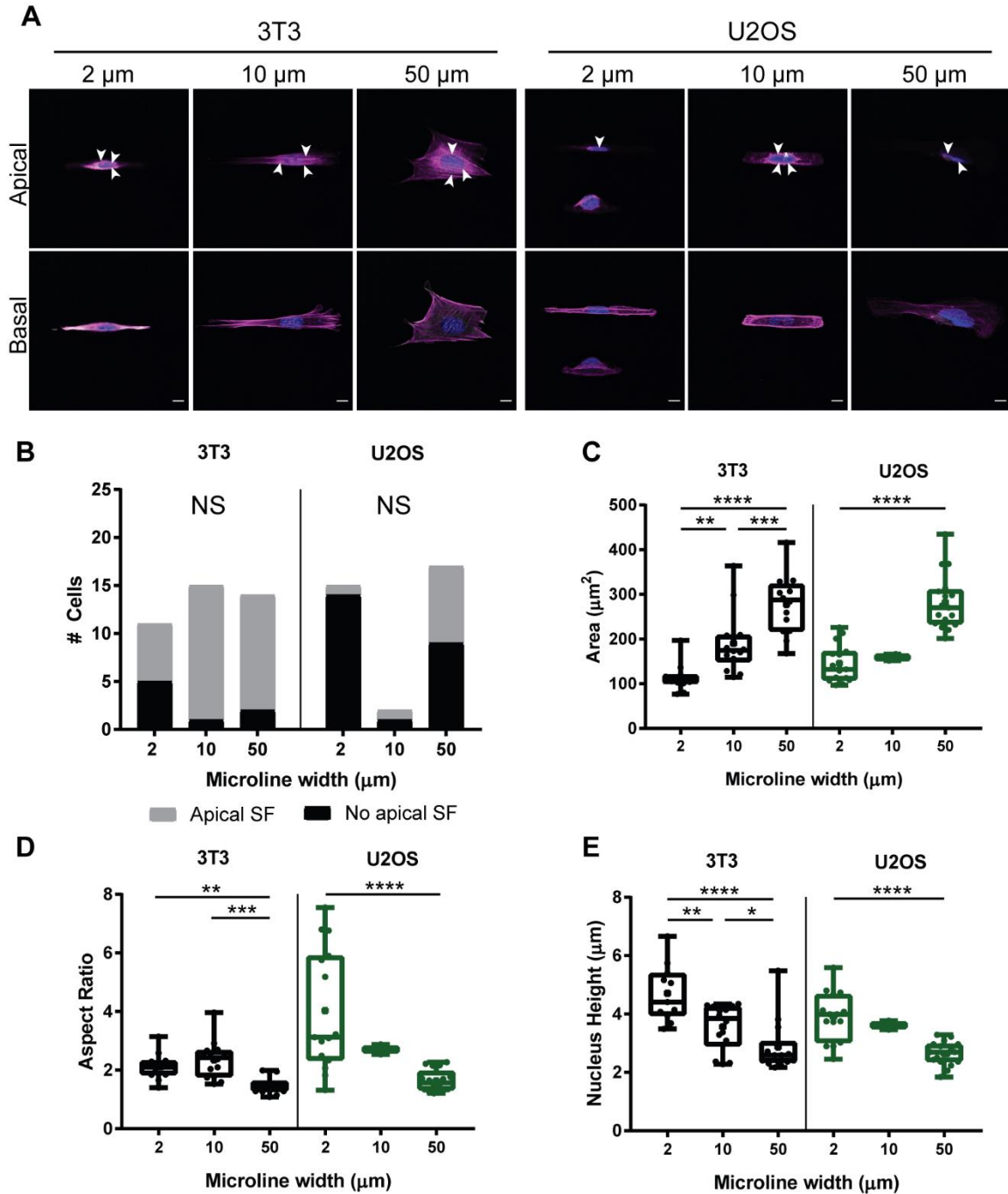
Figure 4.2. Extracellular matrix geometry influences SF architecture and nuclear morphology, but is not correlated with the proportion of cells displaying apical SFs. (A) Representative images of 3T3 or U2OS cells stained for actin (phalloidin, magenta), vinculin (green), and nuclei (blue) on 2, 10, and 50 µm-wide fibronectin microlines. Top and bottom panels show the apical and basal z-slices, respectively. Scale bar: 10 µm. White arrowheads point to selected apically-located SFs. (B) Distribution of 3T3 and U2OS cells with (gray) or without (black) apical SFs on 2, 10, and 50 µm-wide fibronectin microlines. Chi Sqaure testNS: not significant. (C) Distribution of projected nuclear areas. (D) Distribution of projected nuclear aspect ratios. (E) Distribution of nuclear heights. Kruskal-Wallis test, post-hoc Dunn's test; * p < 0.05, ** p < 0.01, *** p < 0.001, **** p < 0.0001. N = 11, 14, and 14 3T3, and 15, 2, and 17 U2OS cells on 2, 10, and 50 µm microlines across 2 independent experiments.

We next asked whether the presence of apical SFs had any impact on the nucleus morphology when cells were cultured on microlines. For both 3T3 and U2OS cells, as the microline width increased, the projected nuclear area increased, the aspect ratio decreased, and the nuclear height decreased (Fig. 4.2C-E). There was no correlation between apical SF formation and altered nuclear morphology. These findings are consistent with the idea that the balance between the ECM adhesive area and the mechanical integrity of the nucleus are more important determinants of nuclear morphology than the presence of apical SFs. Furthermore, the distribution of nuclear aspect ratios of U2OS cells on the 2 µm microlines was larger than that of the 3T3 cells, indicating that the nuclei in U2OS cells are more deformable. Taken together, these results suggest that the presence of apical SFs does not correlate with nuclear morphology when cells are cultured on fibronectin microlines of varying widths.

Apical SFs are under higher prestress than basal SFs

SFs are a major determinant to cell shape, enabling migration and mechanosensing. Previously, we and other have shown that spatial organization, SF composition, and SF length influences SF mechanics and presumably their structural role (29,52,53,122,147,174). Since apical SFs are spatiotemporally distinct, contain higher levels of pMLC, and are longer than basal SFs, we next assessed whether these two categories of SFs had different mechanical properties. We used laser ablation to sever apical and basal SFs in MEF Lifeact-GFP cells and tracked the retraction of the SFs over time. MEF Lifeact-GFP cells cultured on flat, fibronectin-coated glass coverslips displayed both apical and basal SFs, which were spatially distinct in the z-direction and enabled selective severing of either population without affecting the other (Fig. 4.3A). Upon incision, SFs underwent retraction, which could be tracked over time (Fig. 4.3A-B). To compare SF prestress (stored elastic energy), we used the retraction distance at 45 s, the time at which a majority of severed SFs reached their plateau retraction distance, as a proxy measurement. We defined the retraction distance at 45 s as one-half the difference between the two severed ends at 45 s and at 0 s. Apical SFs had higher retraction distances than basal SFs (p < 0.001, Mann-Whitney test, Fig. 4.3C), indicating that apical SFs are under higher prestresses. However, we also found that apical SFs also tended to be longer in length than basal SFs (p < 0.0001 Mann-Whitney test, Fig. 4.3D), so it is unclear whether the measured differences in prestress are due to differences in SF composition or formation, the length disparities, or some combination of the two. When we plotted the prestresses against the length of the unsevered SF (Fig. 4.3E), we did not find a correlation between SF length and measured prestress for the apical SF or basal SF subpopulation (apical SFs: Spearman's R = 0.24, p = 0.16; basal SFs: Spearman's R = 0.25, p = 0.16). Taken together, these results indicate that apical SFs are under higher mechanical tension than basal SFs, which is in part due to longer overall SF lengths.

Apical SFs and basal SFs in MEFs on curved substrates are not mechanically distinct from apical SFs and basal SFs, respectively, on flat surfaces

Given that substrate curvature has been found to influence the organization of apical and basal SFs, we next asked what effect curvature would have on the mechanical properties of these SFs. To answer this, we cultured cells on SWS surfaces with smoothly continuous changes in substrate curvature (Fig. 4.4A-B). These substrates are fabricated from a thin layer of PDMS
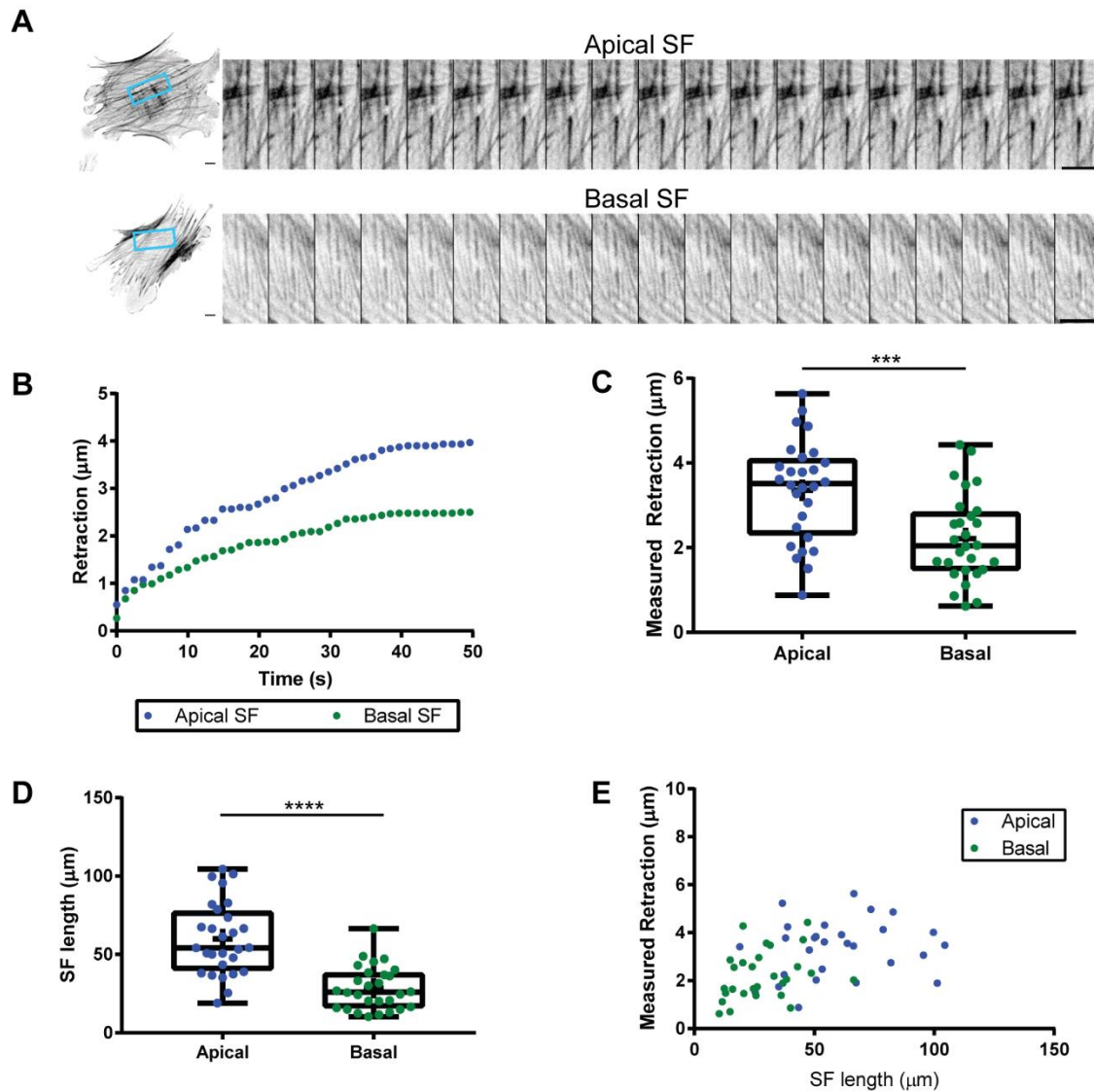
Figure 4.3: Apical SFs are under higher prestress than basal SFs. (A) A single apical SF or basal SF in MEF Lifeact-GFP cells are severed. Montages show retraction upon severing over time for apical SF (top row) or basal (bottom row) SFs. Blue box indicates region containing the severed SF. Time between each frame in the montage is ~3 s. Scale bars: 10 µm. (B) Representative retraction traces of severed apical (blue) and basal (green) SFs. (C) Distribution of apical (blue) and basal (green) SF retraction distances measured at 45 s post-ablation. *** p < 0.001, Mann-Whitney test. (D) Distribution of apical (blue) and basal (green) SF lengths. **** p < 0.001, Mann-Whitney test. (E) Retraction distance plotted against SF length for apical (blue) and basal (green) SFs. No correlation exists between apical SF length and retraction distance (Spearman's R = 0.24, p = 0.16); no correlation exists between basal SF length and retraction distance (Spearman's R = 0.25, p = 0.16). N = 28 apical and 28 basal SFs across 3 independent experiments.

spun-coat over glass beads embedded in a PDMS layer, resulting in a surface with smooth curvature gradients with maximum curvature at the top of the sphere and decreasing curvature further down the skirt surface, and flat regions between SWS features (Fig. 4.4B) (170). MEFs on the curved regions tended to be more elongated along the radial direction of the SWS (i.e. long axis oriented along the curvature gradient), whereas those on the flat regions tended to be

57

more symmetrically spread (Fig. 4.4A). None of the cells imaged had their long axis circumferential around the SWS (i.e. long axis oriented around the SWS, at the same curvature). We next used laser nanosurgery to sever a single apical SF or a single basal SF in cells that were on either residing on the curved or flat regions of the SWS substrates (Fig. 4.4A, 4.4C). For cells on the curved regions of the substrates, apical SFs had larger retraction distances than basal SFs, suggesting that they were under higher prestress ($p < 0.0001$, Kruskal-Wallis test, post-hoc Dunn's test). Similarly, on the flat regions of the substrate, apical SFs also had larger retraction distances than basal SFs ($p < 0.05$, Kruskal-Wallis test, post-hoc Dunn's test). These results mirror the apical vs. basal SF prestress findings on the flat glass substrates. When we compare prestresses of apical SFs on flat vs. curved regions of the SWS substrates, however, we do not find any statistical differences between those two groups ($p > 0.9999$, Kruskal-Wallis test, post-hoc Dunn's test). Similarly, there were no statistical differences in retraction distances of basal SFs on curved and flat regions ($p > 0.9999$, Kruskal-Wallis test, post-hoc Dunn's test). The disparities in apical SF and basal SF lengths were also observed on both the curved and flat regions of the substrates ($p < 0.01$, Kruskal-Wallis test, post-hoc Dunn's test, Fig. 4.4E). Finally, we did not find a correlation between SF length and retraction distance within any of the groups tested. These results indicate that curvature does not measurably influence apical and basal SF prestresses: apical (basal) SF prestresses on curved substrates were not different from apical (basal) SF prestresses on flat substrates, and differences in apical and basal SF prestresses are preserved across flat and curved geometries.

4.4 Discussion

Apical and basal SFs are spatiotemporally-separate subsets of ventral SFs that have distinct organizations on curved topographies. By combining laser nanosurgery and engineered surfaces with precisely defined adhesive or topographical features, we have shown that apical SFs are under higher mechanical tension than basal SFs and that while substrate topography does influence the organization of the SFs, it does not affect their underlying mechanical properties. Furthermore, although apical SFs are positioned over and mechanically link the nucleus to the ECM, we find no evidence that they have a measurable impact on nuclear area, aspect ratio, and height. Likewise, when cells are cultured on fibronectin microlines of defined adhesive widths, we find that the presence of apical SFs is not correlated with nuclear shape. Taken together, these results suggest that the roles of apical SFs may be to position the nucleus in the cell or to directly transmit biophysical signals from the ECM to the nucleus.

Our studies directly measure apical and basal SF mechanics and test predictions of their functions. For example, one study found that the FAs associated with apical SFs have different morphodynamics and are important in mechanosensing on substrates in the 5-500 kPa stiffnesses range, compared to basal SF-associated FAs, which are mechanosensitive up to 5 kPa (173). Based largely on observational studies of FA and SF morphology in response to perturbations in substrate stiffness, protein expression, myosin regulatory light chain phosphorylation, and FA area, it was suggested that FAs associated with apical SFs were under higher tension.
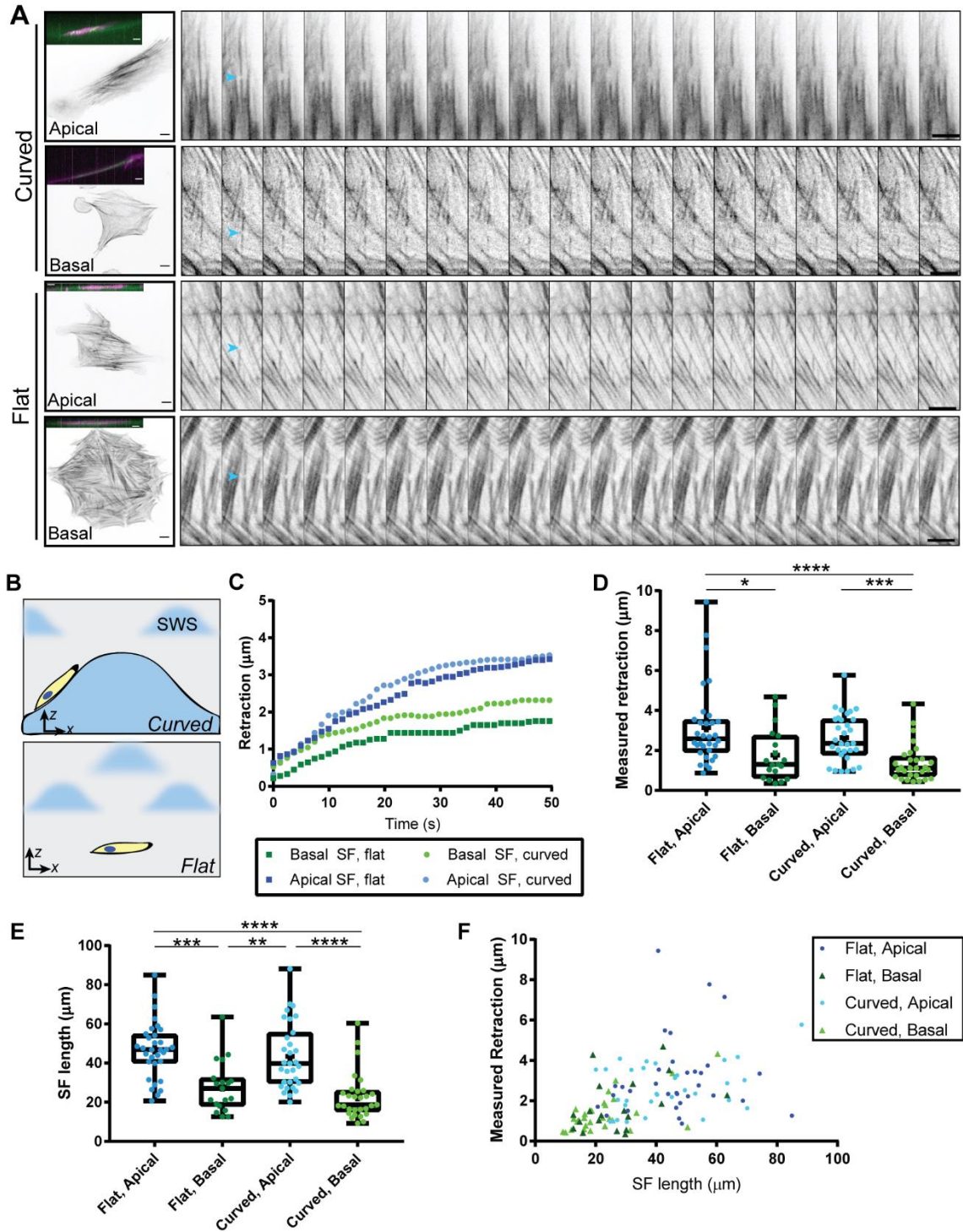
Figure 4.4. Curvature does not influence apical SF and basal SF mechanics. (A) Representative images of MEF Lifeact GFP cells on curved or flat regions of the SWS substrate where an apical or basal SF is severed. Insets show pseudocolor xz-reconstructions of the cell (magenta) and the fibronectin-coated substrate (green). Montages show retraction of the severed SF, indicated by the blue arrowhead. Time between each frame in the montage is ~3 s Scale bars: 10 µm. (B) Schematic showing xz-view of cells on a curved (top panel) or flat (bottom panel) region of the SWS substrate. (C) Example retraction traces of severed apical SFs on a flat region (dark blue) and curved region (light blue), and of basal SFs on a flat (dark green) and curved region (light green)

of the SWS substrate. (D) Measured retraction distances for apical and basal SFs on flat and curved regions of the SWS substrate. Within any given substrate topography, apical SFs retracted larger distances than basal SFs. (E) Distribution of severed SF lengths for apical or basal SFs on flat and curved regions. (F) Retraction distance plotted against SF length for apical SFs on flat (blue) or curved (light blue) regions and basal SFs on flat (green) and curved (light green) regions. * $p < 0.05$, ** $p < 0.01$, *** $p < 0.001$, **** $p < 0.0001$, Kruskal-Wallis test, post-hoc Dunn's test (Panel D and E). Spearman's R values: apical SF, curved: 0.26, basal SF, curved: 0.49, apical SF, flat: 0.11, basal SF, flat: 0.42, not significant. N = 32 apical SFs on flat regions, 19 basal SFs on flat regions, 31 apical SFs on curved regions, and 29 basal SFs on curved regions across 6 independent experiments.

However, these perturbations are not specific to apical SFs and may also influence basal SF function (173). Furthermore, observations that apical SFs are thicker, and are more susceptible to contractility inhibitors and actin depolymerization agents, suggested that these SFs were differentially regulated and may have different properties (171). By applying laser nanosurgery, we are able to conduct direct-loss-of-function studies on selected SFs in the cell and infer its prestress from its retraction kinetics. Our results support previous findings that apical SFs bear larger prestresses and are mechanically distinct from basal SFs.

It remains unclear from the data presented here how the differences in apical and basal SF prestress arise. Past work has shown that SF composition, structure, and formation pathway can affect SF retraction properties (53,123,147) and that longer SFs tend to bear higher prestresses due to an increase in the number of contractile units along the SF (122). Thus, the higher prestresses observed in the apical SFs could have been a result of (1) the differences in SF length, (2) intrinsic differences in the formation, composition, and structure of these two types of SFs, or (3) some combination of the two. SFs have been conventionally modeled as viscoelastic Kelvin-Voigt materials, with the retraction expected to follow a negative exponential curve. SF prestress is derived from the fitted plateau retraction distance, and the viscoelasticity is derived from the fitted time constant (52,63). However, during the course of SF retraction tracking, we noted that 20-30% of the retraction curves for both apical and basal SFs did not follow a negative exponential curve, and instead appeared to be linear or did not reach a plateau retraction distance within the imaging window. These effects were more prominent in the apical SFs. Because these curves would not produce meaningful Kelvin-Voigt fits, we used the retraction distance after 45 s, a metric that does not make any assumptions about SF material properties, as a proxy for prestress. It was speculated that these non-Kelvin-Voigt SFs could arise from the underlying organization of the SF, which in turn is derived from the method that the SF forms and/or the amount of external connections to cytosolic components, which can act to slow or speed retractions (147). Either of these possibilities could be in play for the apical and basal SFs severed in our experiments. Apical SFs have more pronounced non-Kelvin-Voigt effects, which can be due to their long lengths and curved shape. Basal SFs are typically located flush against the bottom membrane surface, giving ample opportunity for sections of the SF to experience drag during retraction, which would slow down retraction. Live cell timelapse imaging along with super-resolution imaging of the SF network would provide clues into the dynamics of apical and basal SF formation and evolution and connections to other cytoskeletal and FA components.

Given their localization along the bottom inner membrane of the cell, the primary role of basal SFs is likely to generate traction forces which enable the cell to extend lamellipodia for

migration. However, the exact function of apical SFs is currently unknown. Their placement over the nucleus suggests that they interact with the nucleus: apical SFs have been reported to shape and compress the nucleus (171,172). However, we did not observe any correlation between the presence of apical SFs and nuclear morphology, which suggests that apical SFs may have other functions. For example, others have reported that apical SFs are important for nuclear positioning and translocation, particularly during migration (170,173,177). Given that the 3T3 and MEF cells we studied rarely displayed the dorsal SFs and transverse arc subtypes commonly associated with mesenchymal migrating cells, a possible role of apical SFs could be to provide the structural framework to enable migration and to directly connect the ECM to the nucleus in the absence of the dorsal SF and transverse arc SF subtypes. Apical SFs also likely are critical in mechanosensing through their association with the LINC complex, which provides a direct connection from the ECM to the nucleus (174). In support of this mechanosensing role, enucleated cells, which by definition lack apical SFs, are less sensitive to substrate cues and are unable to polarize and directionally migrate when embedded in a fibrous 3D collagen substrate (180). Finally, we and others have found that apical and basal SFs could have roughly orthogonal orientations with respect to one another when cells were on 2D substrates and this effect was more pronounced when cells were cultured on substrates with high curvatures (169). Taken together, these suggest that apical SFs may become more critical when the cell is cultured in challenging microenvironments.

Our work demonstrates that apical SFs and basal SFs have different mechanical properties in the cell. Future work would explore the causes and mechanism of apical SF formation in cells that do not reliably display them (e.g. U2OS and U251 cells). High-resolution timelapse imaging combined with precisely engineered surfaces would also provide insights into how changing topographical features reorganization the SF network and enable a more nuanced analysis of the effect of the degree of curvature on SF mechanics. These studies should offer invaluable insights into how cells establish their shape when cultured on topographically-complex substrates.

4.5 Materials and Methods

Cell Culture

NIH 3T3 cells were obtained from the UC Berkeley Cell Culture Facility and were cultured in DMEM (Gibco) supplemented with 10% calf serum (JR Scientific), 1% non-essential amino acids (Gibco), 1% sodium pyruvate (Gibco), and 1% penicillin/streptomycin (Gibco).

U2OS cells (ATCC HBT-96) were cultured in DMEM (Gibco) supplemented with 10% FBS (JR Scientific), 1% non-essential amino acids (Gibco), and 1% penicillin/streptomycin (Gibco). Cells were tested for mycoplasma every three months and authenticated via short tandem repeat profiling.

U251 cells were obtained from the UC Berkeley Cell Culture Facility and were cultured in DMEM (Gibco) supplemented with 10% calf serum (JR Scientific), 1% non-essential amino acids (Gibco), 1% sodium pyruvate (Gibco), and 1% penicillin/streptomycin (Gibco).

Primary MEF Lifeact-GFP cells were obtained from the Richard Assoian lab and cultured in DMEM (Gibco) supplemented with 10% FBS (JR Scientific), 1% non-essential amino acids (Gibco), and 1% penicillin/streptomycin (Gibco).

Immunostaining

Cells were rinsed briefly with DPBS and then fixed in 4% (v/v) paraformaldehyde (Alfa-Aeser) for 10 min at room temperature. Cells were permeabilized for 10 minutes in 0.3% (v/v) triton-X (EMD Millipore) diluted in PBS containing 5% (v/v) goat serum (Thermo Fisher) for 10 min. Cells were blocked in PBS containing 5% (v/v) goat serum for 16 h at 4 ºC. Coverslips were incubated with primary antibodies for 2 h at room temperature, rinsed with 1% (v/v) goat serum in PBS, and then incubated with secondary antibodies and phalloidin (Life Technologies) for 1 h at room temperature in the dark. Nuclei were stained with Hoechst (1:500, Thermo Fisher) or DAPI (1:500, Sigma). Cells were rinsed in PBS and mounted using Fluoromount-G (Southern Biotech).

The following primary antibodies were used for immunostaining: mouse anti-vinculin hVin-1 (1:200; Sigma), rabbit anti-di-phosphorylated myosin light chain Thr18/Ser19 (1:200; Cell Signaling Technologies). The following secondary antibodies were used: AlexaFluor 488 anti-rabbit (1:400), AlexaFluor 647 anti-mouse (1:400), phalloidin-AlexaFluor 546 (1:200), all from Life Technologies.

Micropatterning

Micropatterns were made as described previously (122,124,135,136,147). Briefly, plasma-treated coverslips were incubated with 10 µg/mL poly-l-lysine conjugated to polyethylene glycol (PLL-g-PEG; SuSoS) in 10 mM HEPES, pH 7.4 for 1 h at room temperature. The coverslips were rinsed briefly with PBS and deionized water. Coverslips were placed on a quartz-chrome photomask bearing the micropattern features (Front Range Photomask) which were designed using AutoCAD (Autodesk). The assembly was then illuminated under 180 nm UV light (Jelight) for 15 minutes. Coverslips were rinsed briefly with PBS.

Imaging

Unpatterned or micropatterned coverslips were coated with 20 µg/mL fibronectin in 100 mM bicarbonate solution, pH 8.5, overnight at 4ºC and rinsed extensively prior to cell seeding. SWS substrates were generously provided by the Kathleen Stebe lab (170) and coated with 20 µg/mL fibronectin and 5 µg/mL Alexa 647-fibronectin (147) in 100 mM bicarbonate solution, pH 8.5, overnight at 4ºC and rinsed extensively before cell seeding. Cells were seeded at 3000-5000 cells/cm^2 and allowed to adhere for 4-6 h before imaging. Prior to live-cell imaging, the medium was changed to phenol red-free DMEM (Gibco) supplemented with 10% FBS, 1% nonessential amino acids, 1% penicillin/streptomycin, and 25 mM HEPES (imaging media).

Confocal imaging. For laser ablation and fixed cell studies, an upright Olympus BX51WI microscope (Olympus Corporation) equipped with Swept Field Confocal Technology (Bruker) and a Ti:Sapphire 2-photon Chameleon Ultra II laser (Coherent) was used. The 2-photon laser was set to 770 nm and single SF ablation was performed using three 20 ms pulses. Cells were imaged again at least 20 min after ablation to verify viability and membrane integrity. Live cell imaging was performed using an Olympus LUMPlanFL N 60x/1.0 water dipping objective. Cells were kept at 37ºC using a stage-top sample heater (Warner Instruments). Fixed cell imaging was

performed using an Olympus UPlanSApo 60x/1.35 oil immersion objective. Images were captured using an EM-CCD camera (Photometrics). The following emission filters were used: Quad FF-01-446/523/600/677-25 (Semrock) and 525/50 ET525/50 (Chroma). PrairieView Software (v. 5.3 U3, Bruker) was used to acquire images.

Image analysis

For visualization purposes, image contrast was adjusted using FIJI (137,138). Nuclear heights were measured from the bottom to top of the nucleus from the 3D reconstruction of z-stack images.

Stress fiber retraction

For SF ablation studies, images were acquired every 1.24 s for 77 s. The XY-coordinates of the two severed ends of the SF were manually tracked in ImageJ. The coordinates were used to calculate the half-distance between the severed ends to measure the retraction of one of the severed ends. The plateau retraction distance, which commonly occurs a time before 45 s post-ablation, is used as a proxy for the stored elastic energy of prestress of the fiber (52).

Statistical Analysis

Statistical analyses and graph generation were performed using GraphPad Prism (v 7.00). Sample distributions was determined to be normal or non-normal through the Shapiro-Wilk normality test. Non-parametric Kruskal-Wallis tests, followed by a post-hoc Dunn's test for multiple comparisons, were used to assess statistical differences in non-normal, continuous data sets. In box plots, the top, middle, and bottom of the plot represent the 75th, 50th (median), and 25th percentiles, respectively. The average is represented by the cross. Bars extend to the maximum and minimum value of the data set. The Chi Square test or the Fisher Exact test were used to assess differences in the distribution of cells with or without apical SFs.

4.6 Acknowledgements

Chapter 5. Conclusions

The work described in this dissertation explores how cell shape is regulated by stress fiber (SF) tension and architecture. In Chapter 1, we reviewed the roles of actomyosin SFs in probing extracellular matrix (ECM) mechanical properties, or mechanosensing, during migration. SFs can differ in their location, formation, and molecular composition, which suggests that these SF subtypes each have different roles in maintaining cell shape and mechanosensing. We also briefly summarized work developing engineered ECMs, including fibronectin microlines, polyacrylamide microchannels, and 2.5D sandwich systems, which all seek to reproducibly and controllably recapitulate salient features of the complex *in vivo* microenvironments in order to examine their effects on cell shape and behavior.

In Chapter 2, we systematically interrogated the biophysical properties of single SFs within the three SF subtypes (dorsal SFs, transverse arcs, and ventral SFs) by examining their retraction kinetics upon incision with a femtosecond laser nanosurgery. We found that while each subtype has distinct mechanical properties, these properties are highly interdependent, given the interconnected nature of the SF network. Consistent with this interdependence, subtype-specific genetic depletion of dorsal SFs or transverse arcs influenced ventral SF retraction. These altered ventral SF retraction kinetics were also partially phenocopied in cells that are cultured on ECM microlines that prevent the formation of dorsal SFs and transverse arcs. Our findings indicate that SF subtypes form a mechanically and temporally integrated network in which contractile properties are determined by intrinsic structure, external connections to other SFs, and formation history.

SFs play a key role in orchestrating the front-back polarization of tension through the organization of SF subtypes. In Chapter 3, we explored the role of actin-severing protein cofilin in establishing mechanical asymmetry in cells. Specifically, we asked whether cofilin contributed to tensional polarization by selectively removing low-tension SFs in order to enrich the population of high-tension SFs, which in turn facilitates symmetry breaking and migration. Endogenous cofilin localized to dorsal SFs, which we showed were the subtype under the least amount of prestress. Next, through traction force microscopy experiments and single SF laser nanosurgery measurements, we found that cofilin knockdown (KD) resulted in an accumulation of low-tension SFs that when summed together, collectively generated higher traction forces than control cells. We also found that cofilin was particularly crucial for the maturation and contractility of transverse arcs, which is needed to establish tensional polarity. Taken together, our findings suggest that cofilin facilitates the depolymerization of low-tension SFs or the fusion of actomyosin fragments into higher-tension SFs, thereby promoting the front-back mechanical asymmetry needed for directed cell migration.

In Chapter 4, we began to explore how substrate curvature influenced the organization and mechanics of apical SFs and basal SFs, two subcategories of ventral SFs. While basal SFs, those found closest to the ECM, are found in virtually all cell types displaying SFs, apical SFs, which are anchored at both ends to the ECM but arc over the nucleus, are not as prevalent. Despite their

placement over and mechanical linkage to the nucleus, we did not find a correlation between the presence of apical SFs and nuclear morphology. Next, using laser nanosurgery to sever SFs in cells cultured on flat substrates, we found that apical SFs were longer in length and under higher prestress than basal SFs. These findings also held true for apical and basal SFs in cells that were cultured on sphere-with-skirt substrates which have topographical features that smoothly change in curvature. Our findings suggest that while apical SFs do not actively shape the nucleus, they are likely important in directly transmitting mechanical information about the ECM to the nucleus.

Overall, our work systematically examines the mechanical roles of different SF subtypes and how cells organize these subtypes to establish cell shape in response to topographical and adhesive ECM cues. However, several unanswered questions still remain. First, our results show that some SFs had retraction kinetics that did not follow a negative exponential curve that is typical of viscoelastic Kelvin-Voigt materials. Instead, the retractions were linear in nature or very gradually reached a plateau, indicating that there was an impaired braking mechanism to slow and eventually stop SF retraction. Super-resolution imaging of crosslinker proteins along SFs suggested that a diminished crosslinker buffer region at the SF ends could account for the lack of SF braking. However, it is unclear whether other factors may also contribute to SF braking, including external connections to other cytoskeletal or cytosolic components. For example, crosslinking proteins along the length of the SF, in theory, can bind to focal adhesion proteins (e.g. crosslinking protein α-actinin is known to have an integrin binding site). For basally-located SFs, these could serve as transient or weak adhesion sites which contribute to SF retraction braking. In contrast, for ventral SFs that form de novo (i.e. independently of dorsal SF and transverse arcs) and for apically-located SFs that arc upward over the nucleus and thus have fewer potential interaction sites with focal adhesions, we observed some SF retractions that had linear characteristics. A systematic study modulating the expression levels of crosslinking proteins would provide more insight into whether they are responsible for braking SF retractions upon compromise of an SF. Furthermore, super-resolution imaging could also show whether there are other cytosolic components that may also affect SF braking.

Second, it is unclear exactly how cofilin is able to mechanosensitively target SFs for depolymerization. Based on in vitro reconstituted assays, others have proposed that the conformation of the actin filament, which can be influenced by myosin contractility levels or increased torsion, affects cofilin binding. SFs are comprised of bundles of F-actin, myosin, and crosslinking proteins, so it is unknown if similar principles apply in cells. Studies in which cofilin localization is tracked in response to localized dissipation of tension, for example, by SF severing, would provide direct evidence that cofilin mechanosensitively targets SFs in cells. Furthermore, the most prominent effects of cofilin KD were observed in the transverse arc SF subtype in U2OS cells. It is unclear how cofilin affects contractility and actin turnover in cells that do not regularly display transverse arcs, e.g. cells that migrate without forming large SFs or fibroblasts with mainly apical and basal ventral SFs. Examining the effects of cofilin KD in other cell types would provide more general idea of the role of tension and actin turnover in establishing front-back polarity.

Finally, an important question is whether these findings hold true when cells are cultured in more complex microenvironments. A majority of studies on SF mechanics done so far have been conducted in cells on flat glass substrates, which are widely used due to ease of cell culture and imaging. However, this simplified substrate fails to capture the complexities that are relevant to cells in vivo. In Chapters 2 and 4, we began to explore the effect of changing environments on SF organization and mechanics by patterning cells on thin-width fibronectin microlines as a model of ECM fibrils and to controllably study cell morphology, and on sphere-with-skirt substrates which subject cells to changing substrate curvatures. However, these experiments only capture a single ECM feature, whereas in vivo, cells interact with environments that may vary in stiffness, adhesivity, and topography. It is important to understand how these parameters individually influence SF mechanics and cell behavior, and then systematically dial in increasing ECM complexity. Advances in substrate engineering and imaging will enable the field to examine how different combinations of ECM properties influence SF mechanics and paint a more nuanced picture of cell behavior in complex environments.

References

1. Discher DE. Tissue Cells Feel and Respond to the Stiffness of Their Substrate. Science (80-). 2005 Nov 18;310(5751):1139–43. DOI: 10.1126/science.1116995

2. Engler A, Bacakova L, Newman C, Hategan A, Griffin M, Discher D. Substrate Compliance versus Ligand Density in Cell on Gel Responses. Biophys J. 2004 Jan;86(1):617–28. DOI: 10.1016/S0006-3495(04)74140-5

3. Engler AJ, Sen S, Sweeney HL, Discher DE. Matrix Elasticity Directs Stem Cell Lineage Specification. Cell. 2006 Aug;126(4):677–89. DOI: 10.1016/j.cell.2006.06.044

4. Keung AJ, Asuri P, Kumar S, Schaffer D V. Soft microenvironments promote the early neurogenic differentiation but not self-renewal of human pluripotent stem cells. Integr Biol. 2012 Aug 21;4(9):1049–58. DOI: 10.1039/c2ib20083j

5. Keung AJ, de Juan-Pardo EM, Schaffer D V., Kumar S. Rho GTPases Mediate the Mechanosensitive Lineage Commitment of Neural Stem Cells. Stem Cells. 2011 Nov;29(11):1886–97. DOI: 10.1002/stem.746

6. Rajnicek A, Britland S, McCaig C. Contact guidance of CNS neurites on grooved quartz: influence of groove dimensions, neuronal age and cell type. J Cell Sci. 1997 Dec;110 (Pt 2(23):2905–13.

7. Lo C-M, Wang H-B, Dembo M, Wang Y. Cell Movement Is Guided by the Rigidity of the Substrate. Biophys J. 2000 Jul;79(1):144–52. DOI: 10.1016/S0006-3495(00)76279-5

8. Ulrich TA, de Juan Pardo EM, Kumar S. The Mechanical Rigidity of the Extracellular Matrix Regulates the Structure, Motility, and Proliferation of Glioma Cells. Cancer Res. 2009 May 15;69(10):4167–74. DOI: 10.1158/0008-5472.CAN-08-4859

9. Chan CE, Odde DJ. Traction dynamics of filopodia on compliant substrates. Science. 2008 Dec 12;322(5908):1687–91. DOI: 10.1126/science.1163595

10. Elosegui-Artola A, Oria R, Chen Y, Kosmalska A, Pérez-González C, Castro N, et al. Mechanical regulation of a molecular clutch defines force transmission and transduction in response to matrix rigidity. Nat Cell Biol. 2016 Apr 11; DOI: 10.1038/ncb3336

11. Aratyn-Schaus Y, Gardel ML. Transient Frictional Slip between Integrin and the ECM in Focal Adhesions under Myosin II Tension. Curr Biol. 2010 Jul;20(13):1145–53. DOI: 10.1016/j.cub.2010.05.049

12. Cramer LP, Siebert M, Mitchison TJ. Identification of Novel Graded Polarity Actin Filament Bundles in Locomoting Heart Fibroblasts: Implications for the Generation of Motile Force. J Cell Biol. 1997 Mar 24;136(6):1287–305. DOI: 10.1083/jcb.136.6.1287

13. Niederman R, Pollard TD. Human platelet myosin. II. In vitro assembly and structure of myosin filaments. J Cell Biol. 1975 Oct;67(1):72–92.

14. Vicente-Manzanares M, Ma XX, Adelstein RS, Horwitz AR. Non-muscle myosin II takes centre stage in cell adhesion and migration. Nat Rev Mol Cell Biol. 2009 Nov;10(11):778–90. DOI: 10.1038/nrm2786

15. Ikebe M, Hartshorne DJ. Phosphorylation of smooth muscle myosin at two distinct sites by myosin light chain kinase. J Biol Chem. 1985 Aug 25;260(18):10027–31.

16.   Ikebe M, Koretz J, Hartshorne DJ. Effects of phosphorylation of light chain residues threonine 18 and serine 19 on the properties and conformation of smooth muscle myosin. J Biol Chem. 1988 May 5;263(13):6432–7.

17.   Ikebe M, Hartshorne DJ, Elzinga M. Phosphorylation of the 20,000-dalton light chain of smooth muscle myosin by the calcium-activated, phospholipid-dependent protein kinase. Phosphorylation sites and effects of phosphorylation. J Biol Chem. 1987 Jul 15;262(20):9569–73.

18.   Murata-Hori M, Suizu F, Iwasaki T, Kikuchi A, Hosoya H. ZIP kinase identified as a novel myosin regulatory light chain kinase in HeLa cells. FEBS Lett. 1999 May 14;451(1):81–4. DOI: 10.1016/S0014-5793(99)00550-5

19.   Newell-Litwa KA, Horwitz R, Lamers ML. Non-muscle myosin II in disease: mechanisms and therapeutic opportunities. Dis Model Mech. 2015;dmm.022103-. DOI: 10.1242/dmm.022103

20.   Vicente-Manzanares M, Horwitz AR. Myosin light chain mono- and di-phosphorylation differentially regulate adhesion and polarity in migrating cells. Biochem Biophys Res Commun. 2010 Nov;402(3):537–42. DOI: 10.1016/j.bbrc.2010.10.071

21.   Chrzanowska-Wodnicka M. Rho-stimulated contractility drives the formation of stress fibers and focal adhesions. J Cell Biol. 1996 Jun 1;133(6):1403–15. DOI: 10.1083/jcb.133.6.1403

22.   Jana SS, Kawamoto S, Adelstein RS. A Specific Isoform of Nonmuscle Myosin II-C Is Required for Cytokinesis in a Tumor Cell Line. J Biol Chem. 2006 Aug 25;281(34):24662–70. DOI: 10.1074/jbc.M604606200

23.   Beach JR, Shao L, Remmert K, Li D, Betzig E, Hammer JA. Nonmuscle Myosin II Isoforms Coassemble in Living Cells. Curr Biol. 2014 May;24(10):1160–6. DOI: 10.1016/j.cub.2014.03.071

24.   Shutova MS, Spessott WA, Giraudo CG, Svitkina T. Endogenous Species of Mammalian Nonmuscle Myosin IIA and IIB Include Activated Monomers and Heteropolymers. Curr Biol. 2014 Sep;24(17):1958–68. DOI: 10.1016/j.cub.2014.07.070

25.   Vicente-Manzanares M, Newell-Litwa K, Bachir AI, Whitmore LA, Horwitz AR. Myosin IIA/IIB restrict adhesive and protrusive signaling to generate front–back polarity in migrating cells. J Cell Biol. 2011 Apr 18;193(2):381–96. DOI: 10.1083/jcb.201012159

26.   Vicente-Manzanares M, Koach MA, Whitmore L, Lamers ML, Horwitz AF. Segregation and activation of myosin IIB creates a rear in migrating cells. J Cell Biol. 2008 Nov 3;183(3):543–54. DOI: 10.1083/jcb.200806030

27.   Vicente-Manzanares M, Zareno J, Whitmore L, Choi CK, Horwitz AF. Regulation of protrusion, adhesion dynamics, and polarity by myosins IIA and IIB in migrating cells. J Cell Biol. 2007 Feb 26;176(5):573–80. DOI: 10.1083/jcb.200612043

28.   Burnette DT, Shao L, Ott C, Pasapera AM, Fischer RS, Baird MA, et al. A contractile and counterbalancing adhesion system controls the 3D shape of crawling cells. J Cell Biol. 2014 Apr 14;205(1):83–96. DOI: 10.1083/jcb.201311104

29.   Chang C-W, Kumar S. Differential Contributions of Nonmuscle Myosin II Isoforms and Functional Domains to Stress Fiber Mechanics. Sci Rep. 2015 Sep 4;5:13736. DOI: 10.1038/srep13736

30.   Kovács M, Wang F, Hu A, Zhang Y, Sellers JR. Functional Divergence of Human Cytoplasmic Myosin II. J Biol Chem. 2003 Oct 3;278(40):38132–40. DOI: 10.1074/jbc.M305453200

31.   Wang F, Kovács M, Hu A, Limouze J, Harvey E V., Sellers JR. Kinetic Mechanism of Non-muscle Myosin IIB. J Biol Chem. 2003 Jul 25;278(30):27439–48. DOI: 10.1074/jbc.M302510200

32.   Sandquist JC, Means AR. The C-Terminal Tail Region of Nonmuscle Myosin II Directs Isoform-specific Distribution in Migrating Cells. Mol Biol Cell. 2008 Dec 1;19(12):5156–67. DOI: 10.1091/mbc.E08-05-0533

33.   Pasapera AM, Plotnikov S V., Fischer RS, Case LB, Egelhoff TT, Waterman CM. Rac1-Dependent Phosphorylation and Focal Adhesion Recruitment of Myosin IIA Regulates Migration and Mechanosensing. Curr Biol. 2015 Jan;25(2):175–86. DOI: 10.1016/j.cub.2014.11.043

34.   Jorrisch MH, Shih W, Yamada S. Myosin IIA deficient cells migrate efficiently despite reduced traction forces at cell periphery. Biol Open. 2013 Apr 15;2(4):368–72. DOI: 10.1242/bio.20133707

35.   Lo C-M, Buxton DB, Chua GCH, Dembo M, Adelstein RS, Wang Y. Nonmuscle Myosin IIB Is Involved in the Guidance of Fibroblast Migration. Mol Biol Cell. 2004 Mar 29;15(3):982–9. DOI: 10.1091/mbc.e03-06-0359

36.   Beach JR, Hammer JA. Myosin II isoform co-assembly and differential regulation in mammalian systems. Exp Cell Res. 2015 May;334(1):2–9. DOI: 10.1016/j.yexcr.2015.01.012

37.   Beadle C, Assanah MC, Monzo P, Vallee R, Rosenfeld SS, Canoll P. The Role of Myosin II in Glioma Invasion of the Brain. Mol Biol Cell. 2008 Aug 1;19(8):3357–68. DOI: 10.1091/mbc.E08-03-0319

38.   Thomas DG, Yenepalli A, Denais CM, Rape A, Beach JR, Wang Y, et al. Non-muscle myosin IIB is critical for nuclear translocation during 3D invasion. J Cell Biol. 2015 Aug 17;210(4):583–94. DOI: 10.1083/jcb.201502039

39.   Takaoka M, Saito H, Takenaka K, Miki Y, Nakanishi A. BRCA2 Phosphorylated by PLK1 Moves to the Midbody to Regulate Cytokinesis Mediated by Nonmuscle Myosin IIC. Cancer Res. 2014 Mar 1;74(5):1518–28. DOI: 10.1158/0008-5472.CAN-13-0504

40.   Wylie SR, Chantler PD. Myosin IIC: A Third Molecular Motor Driving Neuronal Dynamics. Mol Biol Cell. 2008 Sep 1;19(9):3956–68. DOI: 10.1091/mbc.E07-08-0744

41.   Thoresen T, Lenz M, Gardel ML. Reconstitution of Contractile Actomyosin Bundles. Biophys J. 2011 Jun;100(11):2698–705. DOI: 10.1016/j.bpj.2011.04.031

42.   Stachowiak MR, McCall PM, Thoresen T, Balcioglu HE, Kasiewicz L, Gardel ML, et al. Self-Organization of Myosin II in Reconstituted Actomyosin Bundles. Biophys J. 2012 Sep;103(6):1265–74. DOI: 10.1016/j.bpj.2012.08.028

43.   Murrell MP, Gardel ML. F-actin buckling coordinates contractility and severing in a biomimetic actomyosin cortex. Proc Natl Acad Sci. 2012 Dec 18;109(51):20820–5. DOI: 10.1073/pnas.1214753109

44.   Murrell M, Gardel ML. Actomyosin sliding is attenuated in contractile biomimetic cortices. Mol Biol Cell. 2014 Jun 15;25(12):1845–53. DOI: 10.1091/mbc.E13-08-0450

45.   Small JV, Rottner K, Kaverina I, Anderson KI. Assembling an actin cytoskeleton for cell attachment and movement. Biochim Biophys Acta - Mol Cell Res. 1998 Sep;1404(3):271–81. DOI: 10.1016/S0167-4889(98)00080-9

46.   Hotulainen P, Lappalainen P. Stress fibers are generated by two distinct actin assembly

mechanisms in motile cells. J Cell Biol. 2006 May 8;173(3):383–94. DOI: 10.1083/jcb.200511093

47. Skau CT, Plotnikov S V., Doyle AD, Waterman CM. Inverted formin 2 in focal adhesions promotes dorsal stress fiber and fibrillar adhesion formation to drive extracellular matrix assembly. Proc Natl Acad Sci. 2015 May 12;112(19):E2447–56. DOI: 10.1073/pnas.1505035112

48. Tojkander S, Gateva G, Husain A, Krishnan R, Lappalainen P. Generation of contractile actomyosin bundles depends on mechanosensitive actin filament assembly and disassembly. Elife. 2015 Jan;4:e06126. DOI: 10.7554/eLife.06126

49. Kovac B, Teo JL, Mäkelä TP, Vallenius T. Assembly of non-contractile dorsal stress fibers requires α-actinin-1 and Rac1 in migrating and spreading cells. J Cell Sci. 2013 Jan 1;126(1):263–73. DOI: 10.1242/jcs.115063

50. Tojkander S, Gateva G, Schevzov G, Hotulainen P, Naumanen P, Martin C, et al. A Molecular Pathway for Myosin II Recruitment to Stress Fibers. Curr Biol. 2011 Apr;21(7):539–50. DOI: 10.1016/j.cub.2011.03.007

51. Totsukawa G, Yamakita Y, Yamashiro S, Hartshorne DJ, Sasaki Y, Matsumura F. Distinct Roles of Rock (Rho-Kinase) and MLCK in Spatial Regulation of MLC Phosphorylation for Assembly of Stress Fibers and Focal Adhesions in 3T3 Fibroblasts. J Cell Biol. 2000 Aug 21;150(4):797–806. DOI: 10.1083/jcb.150.4.797

52. Kumar S, Maxwell IZ, Heisterkamp A, Polte TR, Lele TP, Salanga M, et al. Viscoelastic retraction of single living stress fibers and its impact on cell shape, cytoskeletal organization, and extracellular matrix mechanics. Biophys J. 2006 May;90(10):3762–73. DOI: 10.1529/biophysj.105.071506

53. Tanner K, Boudreau A, Bissell MJ, Kumar S. Dissecting Regional Variations in Stress Fiber Mechanics in Living Cells. Biophys J. 2010 Nov;99(9):2775–83. DOI: 10.1016/j.bpj.2010.08.071

54. Chang C-W, Kumar S. Vinculin tension distributions of individual stress fibers within cell-matrix adhesions. J Cell Sci. 2013 Jul 15;126(14):3021–30. DOI: 10.1242/jcs.119032

55. Albert PJ, Schwarz US. Dynamics of Cell Shape and Forces on Micropatterned Substrates Predicted by a Cellular Potts Model. Biophys J. 2014 Jun;106(11):2340–52. DOI: 10.1016/j.bpj.2014.04.036

56. Kumar A, Ouyang M, Van den Dries K, McGhee EJ, Tanaka K, Anderson MD, et al. Talin tension sensor reveals novel features of focal adhesion force transmission and mechanosensitivity. J Cell Biol. 2016 May 9;213(3):371–83. DOI: 10.1083/jcb.201510012

57. Kassianidou E, Kumar S. A biomechanical perspective on stress fiber structure and function. Biochim Biophys Acta - Mol Cell Res. 2015 Nov;1853(11):3065–74. DOI: 10.1016/j.bbamcr.2015.04.006

58. Deguchi S, Ohashi T, Sato M. Tensile properties of single stress fibers isolated from cultured vascular smooth muscle cells. J Biomech. 2006 Jan;39(14):2603–10. DOI: 10.1016/j.jbiomech.2005.08.026

59. Lu L, Oswald SJ, Ngu H, Yin FC-P. Mechanical Properties of Actin Stress Fibers in Living Cells. Biophys J. 2008 Dec;95(12):6060–71. DOI: 10.1529/biophysj.108.133462

60. Costa KD, Hucker WJ, Yin FC-P. Buckling of actin stress fibers: A new wrinkle in the cytoskeletal tapestry. Cell Motil Cytoskeleton. 2002 Aug;52(4):266–74. DOI: 10.1002/cm.10056

61. Oakes PW, Beckham Y, Stricker J, Gardel ML. Tension is required but not sufficient for focal adhesion maturation without a stress fiber template. J Cell Biol. 2012 Feb 6;196(3):363–74. DOI: 10.1083/jcb.201107042

62. Gateva G, Tojkander S, Koho S, Carpen O, Lappalainen P. Palladin promotes assembly of non-contractile dorsal stress fibers. J Cell Sci. 2014 May 1;127(9):1887–98. DOI: 10.1242/jcs.135780

63. Colombelli J, Besser A, Kress H, Reynaud EG, Girard P, Caussinus E, et al. Mechanosensing in actin stress fibers revealed by a close correlation between force and protein localization. J Cell Sci. 2009 May 15;122(10):1665–79. DOI: 10.1242/jcs.042986

64. Katoh K, Kano Y, Amano M, Kaibuchi K, Fujiwara K. Stress fiber organization regulated by MLCK and Rho-kinase in cultured human fibroblasts. Am J Physiol Physiol. 2001 Jun;280(6):C1669–79. DOI: 10.1152/ajpcell.2001.280.6.C1669

65. Sandquist JC, Swenson KI, DeMali KA, Burridge K, Means AR. Rho Kinase Differentially Regulates Phosphorylation of Nonmuscle Myosin II Isoforms A and B during Cell Rounding and Migration. J Biol Chem. 2006 Nov 24;281(47):35873–83. DOI: 10.1074/jbc.M605343200

66. Guo W, Frey MT, Burnham NA, Wang Y. Substrate Rigidity Regulates the Formation and Maintenance of Tissues. Biophys J. 2006 Mar;90(6):2213–20. DOI: 10.1529/biophysj.105.070144

67. Califano JP, Reinhart-King CA. Substrate Stiffness and Cell Area Predict Cellular Traction Stresses in Single Cells and Cells in Contact. Cell Mol Bioeng. 2010 Mar 6;3(1):68–75. DOI: 10.1007/s12195-010-0102-6

68. Galbraith CG, Yamada KM, Sheetz MP. The relationship between force and focal complex development. J Cell Biol. 2002 Nov 25;159(4):695–705. DOI: 10.1083/jcb.200204153

69. Pelham RJ, Wang Y -l. Cell locomotion and focal adhesions are regulated by substrate flexibility. Proc Natl Acad Sci. 1997 Dec 9;94(25):13661–5. DOI: 10.1073/pnas.94.25.13661

70. Mih JD, Marinkovic A, Liu F, Sharif AS, Tschumperlin DJ. Matrix stiffness reverses the effect of actomyosin tension on cell proliferation. J Cell Sci. 2012 Dec 15;125(24):5974–83. DOI: 10.1242/jcs.108886

71. Zhang H, Berg JS, Li Z, Wang Y, Lång P, Sousa AD, et al. Myosin-X provides a motor-based link between integrins and the cytoskeleton. Nat Cell Biol. 2004 Jun 23;6(6):523–31. DOI: 10.1038/ncb1136

72. Tokuo H, Ikebe M. Myosin X transports Mena/VASP to the tip of filopodia. Biochem Biophys Res Commun. 2004 Jun;319(1):214–20. DOI: 10.1016/j.bbrc.2004.04.167

73. Bohil AB, Robertson BW, Cheney RE. Myosin-X is a molecular motor that functions in filopodia formation. Proc Natl Acad Sci. 2006 Aug 15;103(33):12411–6. DOI: 10.1073/pnas.0602443103

74. Nemethova M, Auinger S, Small JV. Building the actin cytoskeleton: filopodia contribute to the construction of contractile bundles in the lamella. J Cell Biol. 2008 Mar 24;180(6):1233–44. DOI: 10.1083/jcb.200709134

75. Soiné JRD, Brand CA, Stricker J, Oakes PW, Gardel ML, Schwarz US. Model-based Traction Force Microscopy Reveals Differential Tension in Cellular Actin Bundles. Vikram D, editor. PLOS Comput Biol. 2015 Mar 6;11(3):e1004076. DOI: 10.1371/journal.pcbi.1004076

76. Stricker J, Aratyn-Schaus Y, Oakes PW, Gardel ML. Spatiotemporal Constraints on the Force-Dependent Growth of Focal Adhesions. Biophys J. 2011 Jun;100(12):2883–93. DOI:

10.1016/j.bpj.2011.05.023

77.   Beningo KA, Dembo M, Kaverina I, Small JV, Wang Y. Nascent Focal Adhesions Are
       Responsible for the Generation of Strong Propulsive Forces in Migrating Fibroblasts. J Cell Biol.
       2001 May 14;153(4):881–8. DOI: 10.1083/jcb.153.4.881

78.   Grashoff C, Hoffman BD, Brenner MD, Zhou R, Parsons M, Yang MT, et al. Measuring
       mechanical tension across vinculin reveals regulation of focal adhesion dynamics. Nature. 2010
       Jul 8;466(7303):263–6. DOI: 10.1038/nature09198

79.   Austen K, Ringer P, Mehlich A, Chrostek-Grashoff A, Kluger C, Klingner C, et al. Extracellular
       rigidity sensing by talin isoform-specific mechanical linkages. Nat Cell Biol. 2015 Dec
       2;17(12):1597–606. DOI: 10.1038/ncb3268

80.   Meng F, Sachs F. Visualizing dynamic cytoplasmic forces with a compliance-matched FRET
       sensor. J Cell Sci. 2011 Jan 15;124(Pt 2):261–9. DOI: 10.1242/jcs.071928

81.   Wolfenson H, Meacci G, Liu S, Stachowiak MR, Iskratsch T, Ghassemi S, et al. Tropomyosin
       controls sarcomere-like contractions for rigidity sensing and suppressing growth on soft matrices.
       Nat Cell Biol. 2015;18(1):33–42. DOI: 10.1038/ncb3277

82.   Jiang G, Giannone G, Critchley DR, Fukumoto E, Sheetz MP. Two-piconewton slip bond between
       fibronectin and the cytoskeleton depends on talin. Nature. 2003 Jul 17;424(6946):334–7. DOI:
       10.1038/nature01805

83.   Giannone G, Jiang G, Sutton DH, Critchley DR, Sheetz MP. Talin1 is critical for force-dependent
       reinforcement of initial integrin–cytoskeleton bonds but not tyrosine kinase activation. J Cell Biol.
       2003 Oct 27;163(2):409–19. DOI: 10.1083/jcb.200302001

84.   del Rio A, Perez-Jimenez R, Liu R, Roca-Cusachs P, Fernandez JM, Sheetz MP. Stretching Single
       Talin Rod Molecules Activates Vinculin Binding. Science (80-). 2009 Jan 30;323(5914):638–41.
       DOI: 10.1126/science.1162912

85.   Mitchison T, Kirschner M. Cytoskeletal dynamics and nerve growth. Neuron. 1988 Nov;1(9):761–
       72.

86.   Hu K, Ji L, Applegate KT, Danuser G, Waterman-Storer CM. Differential transmission of actin
       motion within focal adhesions. Science. 2007 Jan 5;315(5808):111–5. DOI:
       10.1126/science.1135085

87.   Smilenov LB, Mikhailov A, Pelham RJ, Marcantonio EE, Gundersen GG. Focal adhesion motility
       revealed in stationary fibroblasts. Science. 1999 Nov 5;286(5442):1172–4.

88.   Jurado C. Slipping or Gripping? Fluorescent Speckle Microscopy in Fish Keratocytes Reveals
       Two Different Mechanisms for Generating a Retrograde Flow of Actin. Mol Biol Cell. 2004 Dec
       1;16(2):507–18. DOI: 10.1091/mbc.E04-10-0860

89.   Yeung T, Georges PC, Flanagan LA, Marg B, Ortiz M, Funaki M, et al. Effects of substrate
       stiffness on cell morphology, cytoskeletal structure, and adhesion. Cell Motil Cytoskeleton. 2005
       Jan;60(1):24–34. DOI: 10.1002/cm.20041

90.   Choi CK, Vicente-Manzanares M, Zareno J, Whitmore LA, Mogilner A, Horwitz AR. Actin and
       α-actinin orchestrate the assembly and maturation of nascent adhesions in a myosin II motor-
       independent manner. Nat Cell Biol. 2008 Sep 17;10(9):1039–50. DOI: 10.1038/ncb1763

91.   Peyton SR, Putnam AJ. Extracellular matrix rigidity governs smooth muscle cell motility in a

biphasic fashion. J Cell Physiol. 2005 Jul;204(1):198–209. DOI: 10.1002/jcp.20274

92.   Pathak A, Kumar S. From Molecular Signal Activation to Locomotion: An Integrated, Multiscale Analysis of Cell Motility on Defined Matrices. Klymkowsky M, editor. PLoS One. 2011 Mar 31;6(3):e18423. DOI: 10.1371/journal.pone.0018423

93.   Pathak A, Kumar S. Independent regulation of tumor cell migration by matrix stiffness and confinement. Proc Natl Acad Sci. 2012 Jun 26;109(26):10334–9. DOI: 10.1073/pnas.1118073109

94.   Kubow KE, Conrad SK, Horwitz AR. Matrix Microarchitecture and Myosin II Determine Adhesion in 3D Matrices. Curr Biol. 2013 Sep;23(17):1607–19. DOI: 10.1016/j.cub.2013.06.053

95.   Garcia AJ, Vega MD, Boettiger D. Modulation of Cell Proliferation and Differentiation through Substrate-dependent Changes in Fibronectin Conformation. Mol Biol Cell. 1999 Mar 1;10(3):785–98. DOI: 10.1091/mbc.10.3.785

96.   Lee JP, Kassianidou E, MacDonald JI, Francis MB, Kumar S. N-terminal specific conjugation of extracellular matrix proteins to 2-pyridinecarboxaldehyde functionalized polyacrylamide hydrogels. Biomaterials. 2016 Sep;102:268–76. DOI: 10.1016/j.biomaterials.2016.06.022

97.   Wong SY, Ulrich TA, Deleyrolle LP, MacKay JL, Lin J-MG, Martuscello RT, et al. Constitutive Activation of Myosin-Dependent Contractility Sensitizes Glioma Tumor-Initiating Cells to Mechanical Inputs and Reduces Tissue Invasion. Cancer Res. 2015 Mar 15;75(6):1113–22. DOI: 10.1158/0008-5472.CAN-13-3426

98.   Rape AD, Kumar S. A composite hydrogel platform for the dissection of tumor cell migration at tissue interfaces. Biomaterials. 2014 Oct;35(31):8846–53. DOI: 10.1016/j.biomaterials.2014.07.003

99.   Friedl P, Alexander S. Cancer Invasion and the Microenvironment: Plasticity and Reciprocity. Cell. 2011 Nov;147(5):992–1009. DOI: 10.1016/j.cell.2011.11.016

100.   Doyle AD, Wang FW, Matsumoto K, Yamada KM. One-dimensional topography underlies three-dimensional fibrillar cell migration. J Cell Biol. 2009 Feb 23;184(4):481–90. DOI: 10.1083/jcb.200810041

101.   Burridge K, Wittchen ES. The tension mounts: stress fibers as force-generating mechanotransducers. J Cell Biol. 2013 Jan 7;200(1):9–19. DOI: 10.1083/jcb.201210090

102.   Vallenius T. Actin stress fibre subtypes in mesenchymal-migrating cells. Open Biol. 2013 Jun 19;3(6):130001–130001. DOI: 10.1098/rsob.130001

103.   Pellegrin S, Mellor H. Actin stress fibres. J Cell Sci. 2007 Oct 15;120(20):3491–9. DOI: 10.1242/jcs.018473

104.   Doyle AD, Carvajal N, Jin A, Matsumoto K, Yamada KM. Local 3D matrix microenvironment regulates cell migration through spatiotemporal dynamics of contractility-dependent adhesions. Nat Commun. 2015 Nov 9;6:8720. DOI: 10.1038/ncomms9720

105.   Berthiaume F, Moghe P V, Toner M, Yarmush ML. Effect of extracellular matrix topology on cell structure, function, and physiological responsiveness: hepatocytes cultured in a sandwich configuration. FASEB J. 1996 Nov;10(13):1471–84.

106.   Doyle AD, Yamada KM. Mechanosensing via cell-matrix adhesions in 3D microenvironments. Exp Cell Res. 2015 Nov; DOI: 10.1016/j.yexcr.2015.10.033

107.   Pathak A, Kumar S. Transforming potential and matrix stiffness co-regulate confinement

sensitivity of tumor cell migration. Integr Biol. 2013;5(8):1067–75. DOI: 10.1039/c3ib40017d

108. Denais CM, Gilbert RM, Isermann P, McGregor AL, te Lindert M, Weigelin B, et al. Nuclear envelope rupture and repair during cancer cell migration. Science (80-). 2016 Apr 15;352(6283):353–8. DOI: 10.1126/science.aad7297

109. Rape A, Ananthanarayanan B, Kumar S. Engineering strategies to mimic the glioblastoma microenvironment. Adv Drug Deliv Rev. 2014 Dec;79–80:172–83. DOI: 10.1016/j.addr.2014.08.012

110. Doyle AD, Kutys ML, Conti MA, Matsumoto K, Adelstein RS, Yamada KM. Micro-environmental control of cell migration - myosin IIA is required for efficient migration in fibrillar environments through control of cell adhesion dynamics. J Cell Sci. 2012 May 1;125(9):2244–56. DOI: 10.1242/jcs.098806

111. Shih W, Yamada S. Myosin IIA Dependent Retrograde Flow Drives 3D Cell Migration. Biophys J. 2010 Apr;98(8):L29–31. DOI: 10.1016/j.bpj.2010.02.028

112. Friedl P, Wolf K. Tumour-cell invasion and migration: diversity and escape mechanisms. Nat Rev Cancer. 2003 May;3(5):362–74. DOI: 10.1038/nrc1075

113. Friedl P, Gilmour D. Collective cell migration in morphogenesis, regeneration and cancer. Nat Rev Mol Cell Biol. 2009 Jul;10(7):445–57. DOI: 10.1038/nrm2720

114. Lee S, Kumar S. Actomyosin stress fiber mechanosensing in 2D and 3D. F1000Research. 2016;5(0):2261. DOI: 10.12688/f1000research.8800.1

115. Blanchoin L, Boujemaa-Paterski R, Sykes C, Plastino J. Actin Dynamics, Architecture, and Mechanics in Cell Motility. Physiol Rev. 2014 Jan;94(1):235–63. DOI: 10.1152/physrev.00018.2013

116. Owen LM, Adhikari AS, Patel M, Grimmer P, Leijnse N, Kim MC, et al. A cytoskeletal clutch mediates cellular force transmission in a soft, three-dimensional extracellular matrix. Théry M, editor. Mol Biol Cell. 2017 Jul 7;28(14):1959–74. DOI: 10.1091/mbc.E17-02-0102

117. Hayes AJ, Benjamin M, Ralphs JR. Role of actin stress fibres in the development of the intervertebral disc: Cytoskeletal control of extracellular matrix assembly. Dev Dyn. 1999 Jul;215(3):179–89. DOI: 10.1002/(SICI)1097-0177(199907)215:3<179::AID-AJA1>3.0.CO;2-Q

118. Caspani EM, Echevarria D, Rottner K, Small JV. Live imaging of glioblastoma cells in brain tissue shows requirement of actin bundles for migration. Neuron Glia Biol. 2006 Mar 31;2(02):105. DOI: 10.1017/S1740925X06000111

119. Machesky LM, Hall A. Role of Actin Polymerization and Adhesion to Extracellular Matrix in Rac- and Rho-induced Cytoskeletal Reorganization. J Cell Biol. 1997 Aug 25;138(4):913–26. DOI: 10.1083/jcb.138.4.913

120. Burridge K, Guilluy C. Focal adhesions, stress fibers and mechanical tension. Exp Cell Res. 2016;343(1):14–20. DOI: 10.1016/j.yexcr.2015.10.029

121. Ingber DE. Tensegrity I. Cell structure and hierarchical systems biology. J Cell Sci. 2003 Apr 1;116(7):1157–73. DOI: 10.1242/jcs.00359

122. Kassianidou E, Brand CA, Schwarz US, Kumar S. Geometry and network connectivity govern the mechanics of stress fibers. Proc Natl Acad Sci. 2017 Mar 7;114(10):2622–7. DOI: 10.1073/pnas.1606649114

123. Kassianidou E, Hughes JH, Kumar S. Activation of ROCK and MLCK tunes regional stress fiber formation and mechanics via preferential myosin light chain phosphorylation. Wang Y-L, editor. Mol Biol Cell. 2017 Dec 15;28(26):3832–43. DOI: 10.1091/mbc.e17-06-0401

124. Théry M, Pépin A, Dressaire E, Chen Y, Bornens M. Cell distribution of stress fibres in response to the geometry of the adhesive environment. Cell Motil Cytoskeleton. 2006 Jun;63(6):341–55. DOI: 10.1002/cm.20126

125. Dixon RDS, Arneman DK, Rachlin AS, Sundaresan NR, Costello MJ, Campbell SL, et al. Palladin Is an Actin Cross-linking Protein That Uses Immunoglobulin-like Domains to Bind Filamentous Actin. J Biol Chem. 2008 Mar 7;283(10):6222–31. DOI: 10.1074/jbc.M707694200

126. Grooman B, Fujiwara I, Otey C, Upadhyaya A. Morphology and Viscoelasticity of Actin Networks Formed with the Mutually Interacting Crosslinkers: Palladin and Alpha-actinin. Kreplak L, editor. PLoS One. 2012 Aug 16;7(8):e42773. DOI: 10.1371/journal.pone.0042773

127. Azatov M, Goicoechea SM, Otey CA, Upadhyaya A. The actin crosslinking protein palladin modulates force generation and mechanosensitivity of tumor associated fibroblasts. Sci Rep. 2016 Sep 29;6(1):28805. DOI: 10.1038/srep28805

128. Rönty M, Taivainen A, Moza M, Otey CA, Carpén O. Molecular analysis of the interaction between palladin and α-actinin. FEBS Lett. 2004 May 21;566(1–3):30–4. DOI: 10.1016/j.febslet.2004.04.006

129. Sjöblom B, Salmazo A, Djinović-Carugo K. α-Actinin structure and regulation. Cell Mol Life Sci. 2008 Sep 19;65(17):2688–701. DOI: 10.1007/s00018-008-8080-8

130. Otey CA, Carpen O. a-actinin revisited: A fresh look at an old player. Cell Motil Cytoskeleton. 2004 Jun;58(2):104–11. DOI: 10.1002/cm.20007

131. Parast MM, Otey CA. Characterization of Palladin, a Novel Protein Localized to Stress Fibers and Cell Adhesions. J Cell Biol. 2000 Aug 7;150(3):643–56. DOI: 10.1083/jcb.150.3.643

132. Gupton SL, Eisenmann K, Alberts AS, Waterman-Storer CM. mDia2 regulates actin and focal adhesion dynamics and organization in the lamella for efficient epithelial cell migration. J Cell Sci. 2007 Oct 1;120(19):3475–87. DOI: 10.1242/jcs.006049

133. Leal-Egaña A, Letort G, Martiel J-L, Christ A, Vignaud T, Roelants C, et al. The size-speed-force relationship governs migratory cell response to tumorigenic factors. Gardel M, editor. Mol Biol Cell. 2017 Jun 15;28(12):1612–21. DOI: 10.1091/mbc.E16-10-0694

134. Moffat J, Grueneberg DA, Yang X, Kim SY, Kloepfer AM, Hinkle G, et al. A Lentiviral RNAi Library for Human and Mouse Genes Applied to an Arrayed Viral High-Content Screen. Cell. 2006 Mar;124(6):1283–98. DOI: 10.1016/j.cell.2006.01.040

135. Carpi N, Piel M, Azioune A, Fink J. Micropatterning on glass with deep UV. Protoc Exch. 2011 Jul 7; DOI: 10.1038/protex.2011.238

136. Tseng Q, Wang I, Duchemin-Pelletier E, Azioune A, Carpi N, Gao J, et al. A new micropatterning method of soft substrates reveals that different tumorigenic signals can promote or reduce cell contraction levels. Lab Chip. 2011;11(13):2231. DOI: 10.1039/c0lc00641f

137. Schindelin J, Arganda-Carreras I, Frise E, Kaynig V, Longair M, Pietzsch T, et al. Fiji: an open-source platform for biological-image analysis. Nat Methods. 2012 Jul 1;9(7):676–82. DOI: 10.1038/nmeth.2019

138. Rueden CT, Schindelin J, Hiner MC, DeZonia BE, Walter AE, Arena ET, et al. ImageJ2: ImageJ for the next generation of scientific image data. BMC Bioinformatics. 2017 Dec 29;18(1):529. DOI: 10.1186/s12859-017-1934-z

139. Preibisch S, Saalfeld S, Tomancak P. Globally optimal stitching of tiled 3D microscopic image acquisitions. Bioinformatics. 2009 Jun 1;25(11):1463–5. DOI: 10.1093/bioinformatics/btp184

140. Kirkman TW. Statistics to Use [Internet]. 1996. DOI: http://www.physics.csbsju.edu/stats/

141. Huttenlocher A, Horwitz AR. Integrins in Cell Migration. Cold Spring Harb Perspect Biol. 2011 Sep 1;3(9):a005074–a005074. DOI: 10.1101/cshperspect.a005074

142. Parsons JT, Horwitz AR, Schwartz MA. Cell adhesion: integrating cytoskeletal dynamics and cellular tension. Nat Rev Mol Cell Biol. 2010 Sep 1;11(9):633–43. DOI: 10.1038/nrm2957

143. Ridley AJ. Cell Migration: Integrating Signals from Front to Back. Science (80-). 2003 Dec 5;302(5651):1704–9. DOI: 10.1126/science.1092053

144. Vicente-Manzanares M. Cell migration at a glance. J Cell Sci. 2005 Nov 1;118(21):4917–9. DOI: 10.1242/jcs.02662

145. Petrie RJ, Yamada KM. At the leading edge of three-dimensional cell migration. J Cell Sci. 2012 Dec 15;125(24):5917–26. DOI: 10.1242/jcs.093732

146. Livne A, Geiger B. The inner workings of stress fibers - from contractile machinery to focal adhesions and back. J Cell Sci. 2016 Apr 1;129(7):1293–304. DOI: 10.1242/jcs.180927

147. Lee S, Kassianidou E, Kumar S. Actomyosin stress fiber subtypes have unique viscoelastic properties and roles in tension generation. Wang Y-L, editor. Mol Biol Cell. 2018 Aug 8;29(16):1992–2004. DOI: 10.1091/mbc.E18-02-0106

148. Bravo-Cordero JJ, Magalhaes MAO, Eddy RJ, Hodgson L, Condeelis J. Functions of cofilin in cell locomotion and invasion. Nat Rev Mol Cell Biol. 2013 Jul 19;14(7):405–15. DOI: 10.1038/nrm3609

149. Hayakawa K, Tatsumi H, Sokabe M. Actin filaments function as a tension sensor by tension-dependent binding of cofilin to the filament. J Cell Biol. 2011 Nov 28;195(5):721–7. DOI: 10.1083/jcb.201102039

150. Wioland H, Jegou A, Romet-Lemonne G. Torsional stress generated by ADF/cofilin on cross-linked actin filaments boosts their severing. Proc Natl Acad Sci. 2019 Feb 12;116(7):2595–602. DOI: 10.1073/pnas.1812053116

151. Wiggan O, Shaw AE, DeLuca JG, Bamburg JR. ADF/Cofilin Regulates Actomyosin Assembly through Competitive Inhibition of Myosin II Binding to F-Actin. Dev Cell. 2012 Mar;22(3):530–43. DOI: 10.1016/j.devcel.2011.12.026

152. Bamburg JR, Bernstein BW. Roles of ADF/cofilin in actin polymerization and beyond. F1000 Biol Rep. 2010 Aug 19; DOI: 10.3410/B2-62

153. Chen Q, Pollard TD. Actin filament severing by cofilin is more important for assembly than constriction of the cytokinetic contractile ring. J Cell Biol. 2011 Oct 31;195(3):485–98. DOI: 10.1083/jcb.201103067

154. Hotulainen P, Paunola E, Vartiainen MK, Lappalainen P. Actin-depolymerizing Factor and Cofilin-1 Play Overlapping Roles in Promoting Rapid F-Actin Depolymerization in Mammalian Nonmuscle Cells. Mol Biol Cell. 2005 Feb;16(2):649–64. DOI: 10.1091/mbc.e04-07-0555

155. Thery M, Racine V, Piel M, Pepin A, Dimitrov A, Chen Y, et al. Anisotropy of cell adhesive microenvironment governs cell internal organization and orientation of polarity. Proc Natl Acad Sci. 2006 Dec 26;103(52):19771–6. DOI: 10.1073/pnas.0609267103

156. Vavylonis D, Wu J-Q, Hao S, O'Shaughnessy B, Pollard TD. Assembly Mechanism of the Contractile Ring for Cytokinesis by Fission Yeast. Science (80-). 2008 Jan 4;319(5859):97–100. DOI: 10.1126/science.1151086

157. Luo W, Lieu ZZ, Manser E, Bershadsky AD, Sheetz MP. Formin DAAM1 Organizes Actin Filaments in the Cytoplasmic Nodal Actin Network. Aspenstrom P, editor. PLoS One. 2016 Oct 19;11(10):e0163915. DOI: 10.1371/journal.pone.0163915

158. Tolliday N, VerPlank L, Li R. Rho1 Directs Formin-Mediated Actin Ring Assembly during Budding Yeast Cytokinesis. Curr Biol. 2002 Oct;12(21):1864–70. DOI: 10.1016/S0960-9822(02)01238-1

159. Pollard TD. Regulation of Actin Filament Assembly by Arp2/3 Complex and Formins. Annu Rev Biophys Biomol Struct. 2007 Jun;36(1):451–77. DOI: 10.1146/annurev.biophys.35.040405.101936

160. Luo W, Yu C, Lieu ZZ, Allard J, Mogilner A, Sheetz MP, et al. Analysis of the local organization and dynamics of cellular actin networks. J Cell Biol. 2013 Sep 30;202(7):1057–73. DOI: 10.1083/jcb.201210123

161. Wiggan O, Schroder B, Krapf D, Bamburg JR, DeLuca JG. Cofilin Regulates Nuclear Architecture through a Myosin-II Dependent Mechanotransduction Module. Sci Rep. 2017 Dec 19;7(1):40953. DOI: 10.1038/srep40953

162. Martiel J-L, Leal A, Kurzawa L, Balland M, Wang I, Vignaud T, et al. Measurement of cell traction forces with ImageJ. In 2015. p. 269–87. DOI: 10.1016/bs.mcb.2014.10.008

163. Thevenaz P, Ruttimann UE, Unser M. A pyramid approach to subpixel registration based on intensity. IEEE Trans Image Process. 1998;7(1):27–41. DOI: 10.1109/83.650848

164. Lauffenburger DA, Horwitz AF. Cell Migration: A Physically Integrated Molecular Process. Cell. 1996 Feb;84(3):359–69. DOI: 10.1016/S0092-8674(00)81280-5

165. Gupton SL, Waterman-Storer CM. Spatiotemporal Feedback between Actomyosin and Focal-Adhesion Systems Optimizes Rapid Cell Migration. Cell. 2006 Jun;125(7):1361–74. DOI: 10.1016/j.cell.2006.05.029

166. Li N, Folch A. Integration of topographical and biochemical cues by axons during growth on microfabricated 3-D substrates. Exp Cell Res. 2005 Dec;311(2):307–16. DOI: 10.1016/j.yexcr.2005.10.007

167. Uttayarat P, Toworfe GK, Dietrich F, Lelkes PI, Composto RJ. Topographic guidance of endothelial cells on silicone surfaces with micro- to nanogrooves: Orientation of actin filaments and focal adhesions. J Biomed Mater Res Part A. 2005 Dec 1;75A(3):668–80. DOI: 10.1002/jbm.a.30478

168. Baptista D, Teixeira L, van Blitterswijk C, Giselbrecht S, Truckenmüller R. Overlooked? Underestimated? Effects of Substrate Curvature on Cell Behavior. Trends Biotechnol. 2019 Mar; DOI: 10.1016/j.tibtech.2019.01.006

169. Bade ND, Kamien RD, Assoian RK, Stebe KJ. Curvature and Rho activation differentially control the alignment of cells and stress fibers. Sci Adv. 2017 Sep 6;3(9):e1700150. DOI:

10.1126/sciadv.1700150

170. Bade ND, Xu T, Kamien RD, Assoian RK, Stebe KJ. Gaussian Curvature Directs Stress Fiber Orientation and Cell Migration. Biophys J. 2018 Mar;114(6):1467–76. DOI: 10.1016/j.bpj.2018.01.039

171. Khatau SB, Hale CM, Stewart-Hutchinson PJ, Patel MS, Stewart CL, Searson PC, et al. A perinuclear actin cap regulates nuclear shape. Proc Natl Acad Sci. 2009 Nov 10;106(45):19017–22. DOI: 10.1073/pnas.0908686106

172. Khatau SB, Kim D-H, Hale CM, Bloom RJ, Wirtz D. The perinuclear actin cap in health and disease. Nucleus. 2010 Jul 27;1(4):337–42. DOI: 10.4161/nucl.1.4.12331

173. Kim D-H, Khatau SB, Feng Y, Walcott S, Sun SX, Longmore GD, et al. Actin cap associated focal adhesions and their distinct role in cellular mechanosensing. Sci Rep. 2012 Dec 3;2(1):555. DOI: 10.1038/srep00555

174. Kim D-H, Chambliss AB, Wirtz D. The multi-faceted role of the actin cap in cellular mechanosensation and mechanotransduction. Soft Matter. 2013;9(23):5516. DOI: 10.1039/c3sm50798j

175. Khatau SB, Kusuma S, Hanjaya-Putra D, Mali P, Cheng L, Lee JSH, et al. The Differential Formation of the LINC-Mediated Perinuclear Actin Cap in Pluripotent and Somatic Cells. Kreplak L, editor. PLoS One. 2012 May 4;7(5):e36689. DOI: 10.1371/journal.pone.0036689

176. Gay O, Gilquin B, Nakamura F, Jenkins ZA, McCartney R, Krakow D, et al. RefilinB (FAM101B) targets FilaminA to organize perinuclear actin networks and regulates nuclear shape. Proc Natl Acad Sci. 2011 Jul 12;108(28):11464–9. DOI: 10.1073/pnas.1104211108

177. Chambliss AB, Khatau SB, Erdenberger N, Robinson DK, Hodzic D, Longmore GD, et al. The LINC-anchored actin cap connects the extracellular milieu to the nucleus for ultrafast mechanotransduction. Sci Rep. 2013 Dec 18;3(1):1087. DOI: 10.1038/srep01087

178. Kim D-H, Cho S, Wirtz D. Tight coupling between nucleus and cell migration through the perinuclear actin cap. J Cell Sci. 2014 Jun 1;127(11):2528–41. DOI: 10.1242/jcs.144345

179. Maninová M, Vomastek T. Dorsal stress fibers, transverse actin arcs and perinuclear actin fibers form an interconnected network that induces nuclear movement in polarizing fibroblasts. FEBS J. 2016 Aug; DOI: 10.1111/febs.13836

180. Graham DM, Andersen T, Sharek L, Uzer G, Rothenberg K, Hoffman BD, et al. Enucleated cells reveal differential roles of the nucleus in cell migration, polarity, and mechanotransduction. J Cell Biol. 2018 Mar 5;217(3):895–914. DOI: 10.1083/jcb.201706097

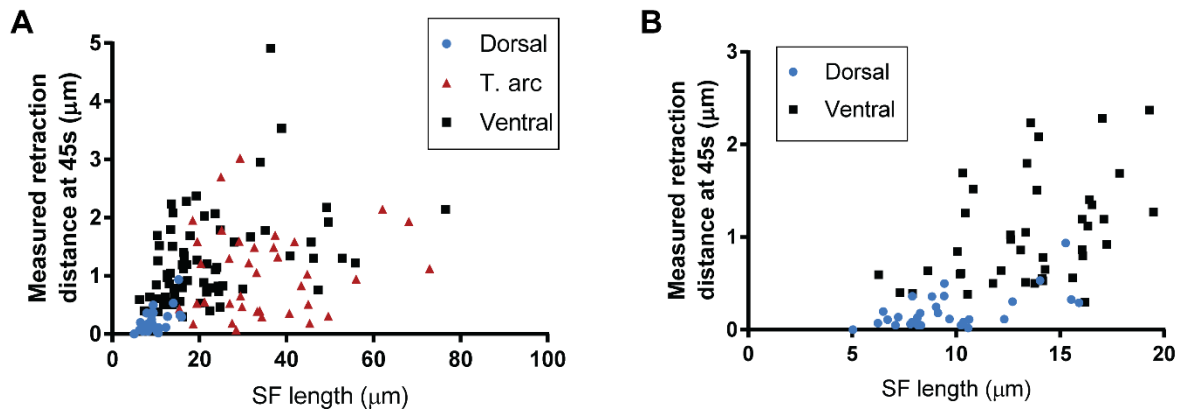# Appendix I. Supplementary Figures for Chapter 2

Figure S1. The reduced retraction of dorsal SFs is not solely explained by short fiber length. (A) Retraction of dorsal SFs (blue circles), transverse arcs (red triangles), and ventral SFs (black squares) plotted against SF length. Data is replotted from Fig. 2.1D. n = 29, 37, and 74 dorsal, transverse arc, or ventral SFs from 13-17 independent experiments. (B) Retraction distance vs. length of dorsal and ventral SFs less than 20 µm in length. n = 29 and 42 dorsal and ventral SFs (data replotted from panel A).
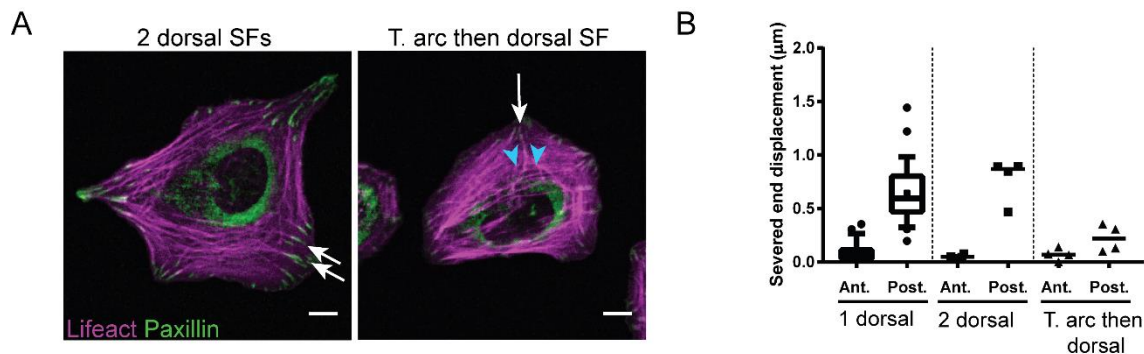
Figure S2. Transverse arcs tense dorsal SFs through direct mechanical connections. (A) Images of cell where either two dorsal SFs (white arrows) are severed simultaneously or a single transverse arc is ablated at two locations (blue arrowheads) followed by a dorsal SF (white arrow). (B) Measured displacements of anterior or posterior dorsal SF fragments 45 s after severing a dorsal SF. Data from cells where only one dorsal SF is ablated is reproduced from Figure 2.2. Each pair of data points where 2 dorsal SFs are severed represents the average anterior and average posterior displacements. Data points where a transverse arc is first severed and then a dorsal SF is severed is measured 45 s after severing the dorsal SF (equivalent to 75 s after the transverse arc was ablated).
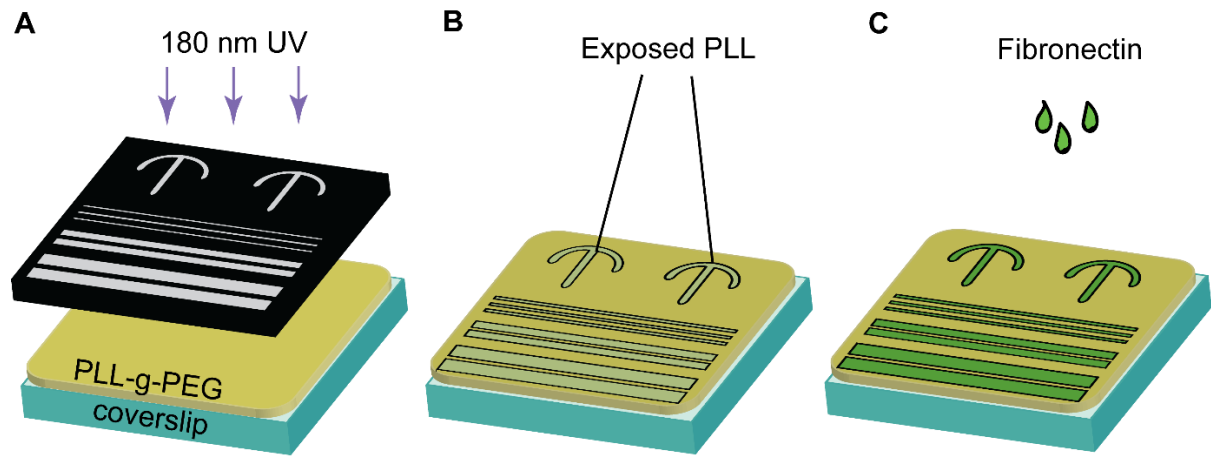
Figure S3. **Schematic of photopatterning method to make fibronectin crossbow or microline patterns.** A PLL-g-PEG coated coverslip is patterned with 180 nm UV and a quartz-chrome mask bearing the pattern features. Fibronectin solution is then adsorbed onto the exposed PLL.
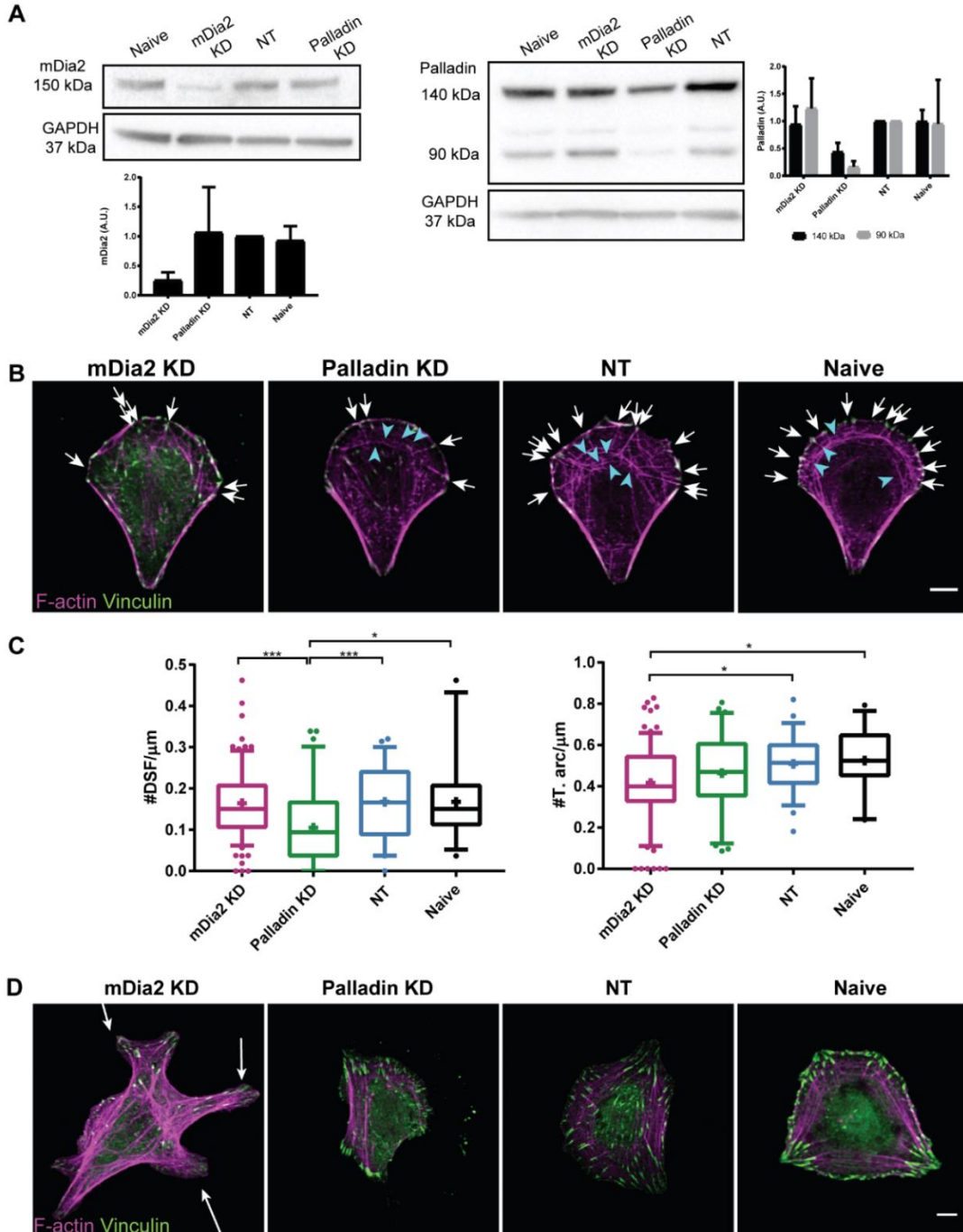
Figure S4. mDia2 KD and palladin KD result in the respective depletion of transverse arcs and dorsal SFs. (A) Western blots showing shRNA-mediated knockdown of mDia2 (~150kDa) or the 140 kDa and 90 kDa isoforms of palladin and relative to naïve and NT controls. Note that the shRNA against palladin was designed to target all nine isoforms, but the antibody only detects the 140 kDa and 90 kDa isoforms. Bar plots show the average band intensities across n = 3 (for mDia2) or n = 2 (for palladin) independent experiments. (B) Cells stained for phalloidin (magenta) and vinculin (green) on fibronectin crossbow patterns. Dorsal SFs are indicated by the white arrows. Transverse arcs are indicated by the blue arrow heads. (C) Quantification of dorsal SF or transverse arc density in each of the cell lines. N = 82, 63, 54, and 27 mDia2 KD, palladin KD, NT, or naïve control cells from 5-7 independent experiments. Kruskal-Wallis test followed by post-hoc Dunn's test. * p < 0.05, *** p < 0.001. Bars extend to 10th and 90th percentiles. Cross depicts mean. (D) Representative images of KD and control cells on unpatterned fibronectin-coated glass. White arrows point to protrusions in a representative mDia2 KD cell that are devoid of transverse arcs. Scale bar: 10 µm.
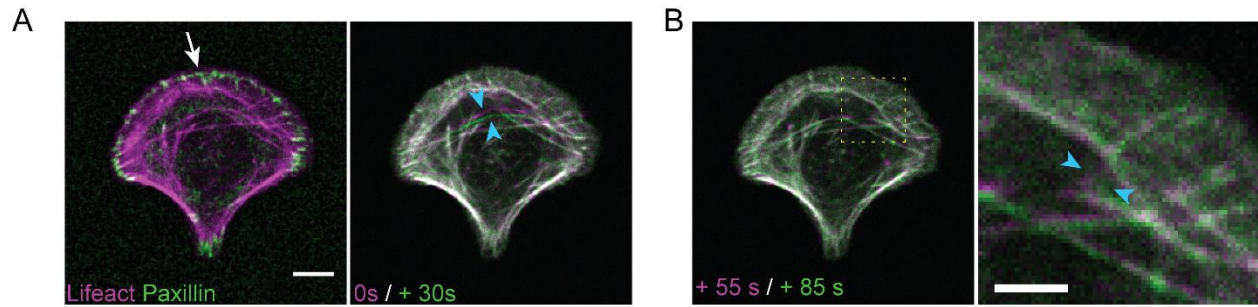
Figure S5. **Evidence of mechanical connections between fiber subtypes in crossbow-patterned cells.** (A) A dorsal SF (white arrow) is severed, after which a connected transverse arc translocates (blue arrowheads). Left panel shows a LifeAct (magenta)/paxillin (green) merged image. Right panel shows a merged image of the cell immediately after ablation of the indicated dorsal SF (magenta) and 30 s after the dorsal SF is severed (green). Scale bar 10 µm. (B) A transverse arc in the same cell as in (A) is severed 55 s after the dorsal SF. A dorsal SF connected to one of the severed transverse arc ends translocates with the retracting transverse arc end (blue arrowheads). Image shows Lifeact image at the point when the transverse arc is severed (magenta) and 30 s after the arc is severed (green). Inset shows the dotted region of interest, scale bar 5 µm.
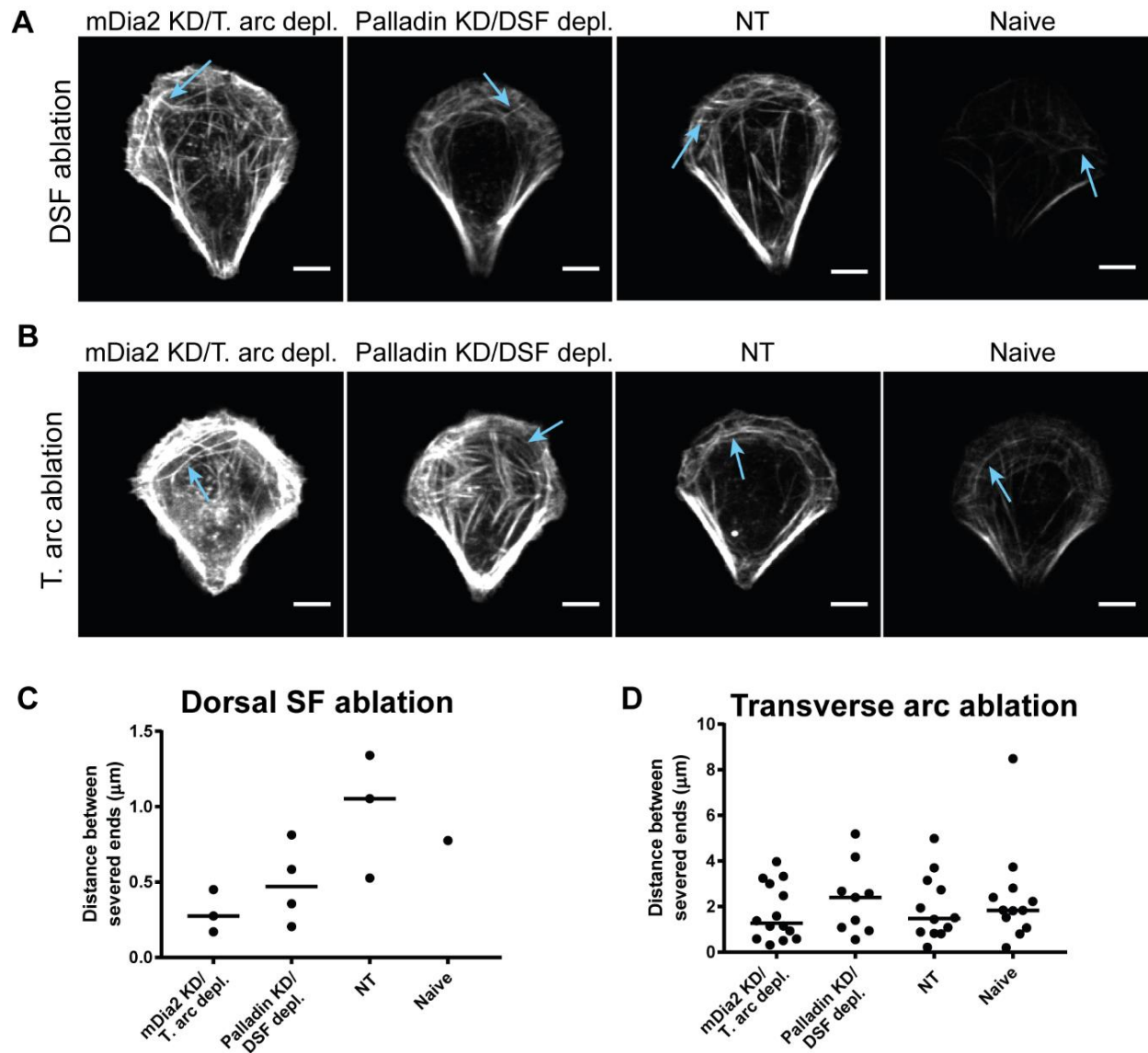
Figure S6. **Ablation of dorsal SFs and transverse arcs in SF-depleted and control cells.** (A) Dorsal SFs in crossbow-patterned cells imaged by RFP-LifeAct. Palladin KD/dorsal SF depleted cell has fewer and shorter dorsal SFs compared to controls. Severed dorsal SFs are indicated by the blue arrows. (B) Transverse arcs in crossbow-patterned cells. mDia2 KD/transverse arc-depleted cells have short transverse arc-like SFs that do not span the entire width of the pattern. Severed transverse arcs are indicated by the blue arrows. (C) Retraction of dorsal SFs (note y-axis values) in each cell line. N = 3, 4, 3, and 1 cells for mDia2 KD/transverse arc-depleted, palladin KD/dorsal SF-depleted, NT, and naïve cells from 1-3 independent experiments. Line indicates median. (D) Transverse arc retraction across cell lines. N = 14, 9, 12, and 12 cells for mDia2 KD/transverse arc-depleted, palladin KD/dorsal SF-depleted, NT, and naïve cells from 4-7 independent experiments. Line indicates median. Scale bar: 10 µm.
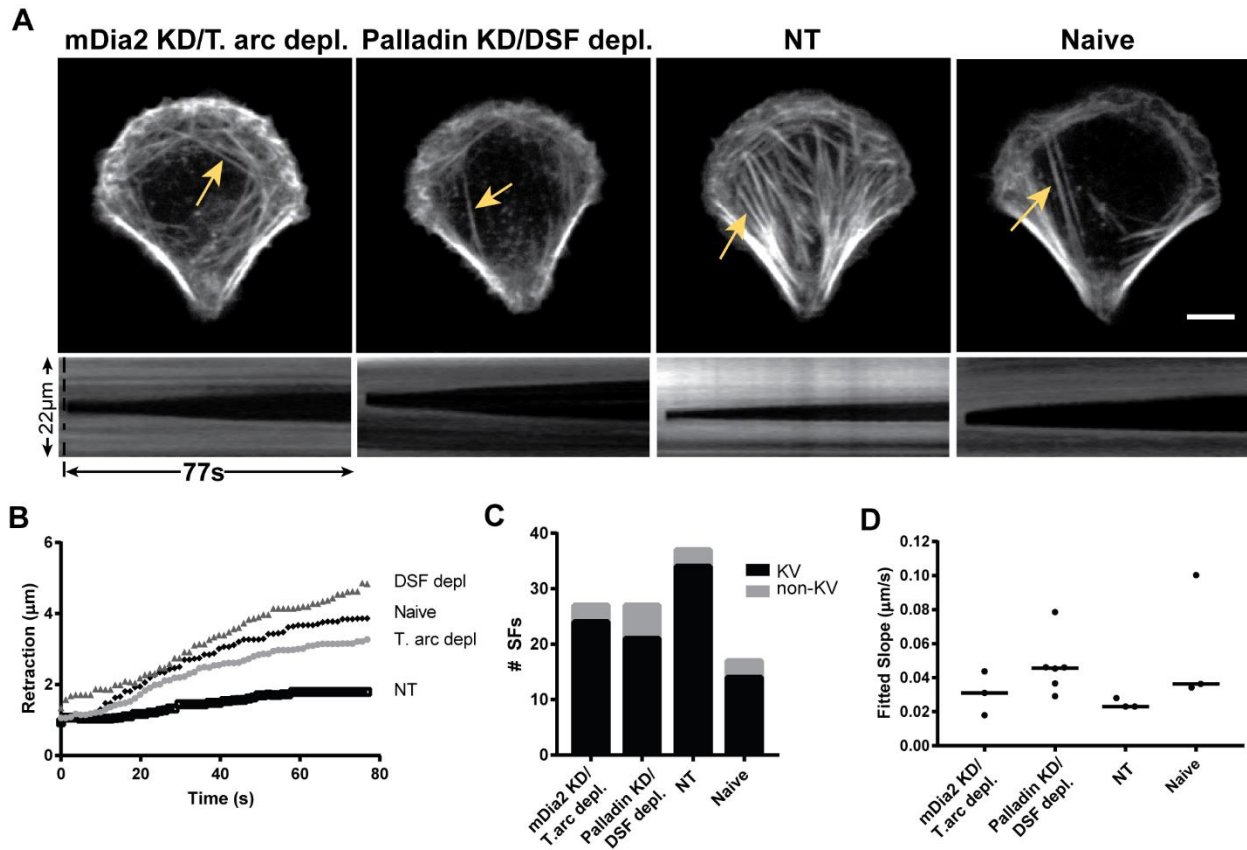
Figure S7. A subset of ventral SFs did not clearly plateau within the 77 s imaging window. (A) Representative images of cells and corresponding kymographs of ablated ventral SFs (yellow arrow). Scale bar: 10µm. (B). Retraction profiles corresponding to the kymographs in (A). (C) Distribution of retraction profiles for severed ventral SFs, with profiles categorized according to whether they displayed Kelvin-Voigt kinetics (KV) or not (non-KV) based on the value of the fitted τ. N = 27, 27, 39, and 17 ventral SFs for mDia2 KD/transverse arc-depleted, palladin KD/dorsal SF-depleted, NT, and naïve cells from 9-10 independent experiments. (D) Measured linear retraction rate at 77 s for SFs that were classified as non-KV in (C). Line indicates median.
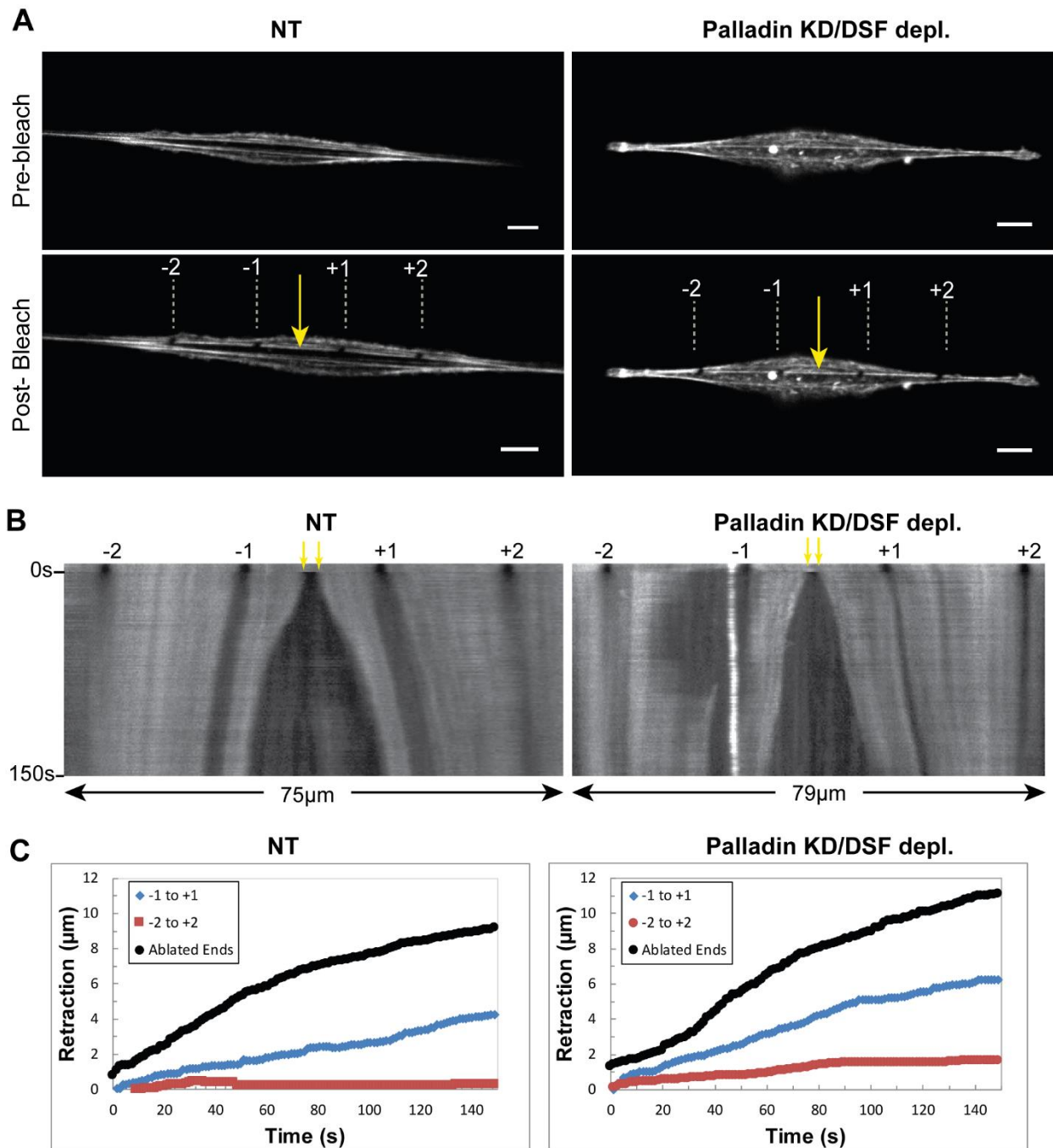
Figure S8. **The atypical, non-plateauing retractions observed in several cells is due to retraction rather than depolymerization of the severed ends.** (A) Top panel: image of NT or palladin KD cell on a 2 µm microline prior to SF bleaching and severing. Bottom panel: bleached fiducial markers are indicated by the numbers. The ablation site is indicated by the yellow arrow. Scale bar: 10 µm. (B) Kymograph of the indicated fiber. Yellow arrows point to the ablation site and the numbered spots correspond to the labels in (A). (C) Retraction traces between pairs of the ablated ends (black) or the bleached spots (blue, red).
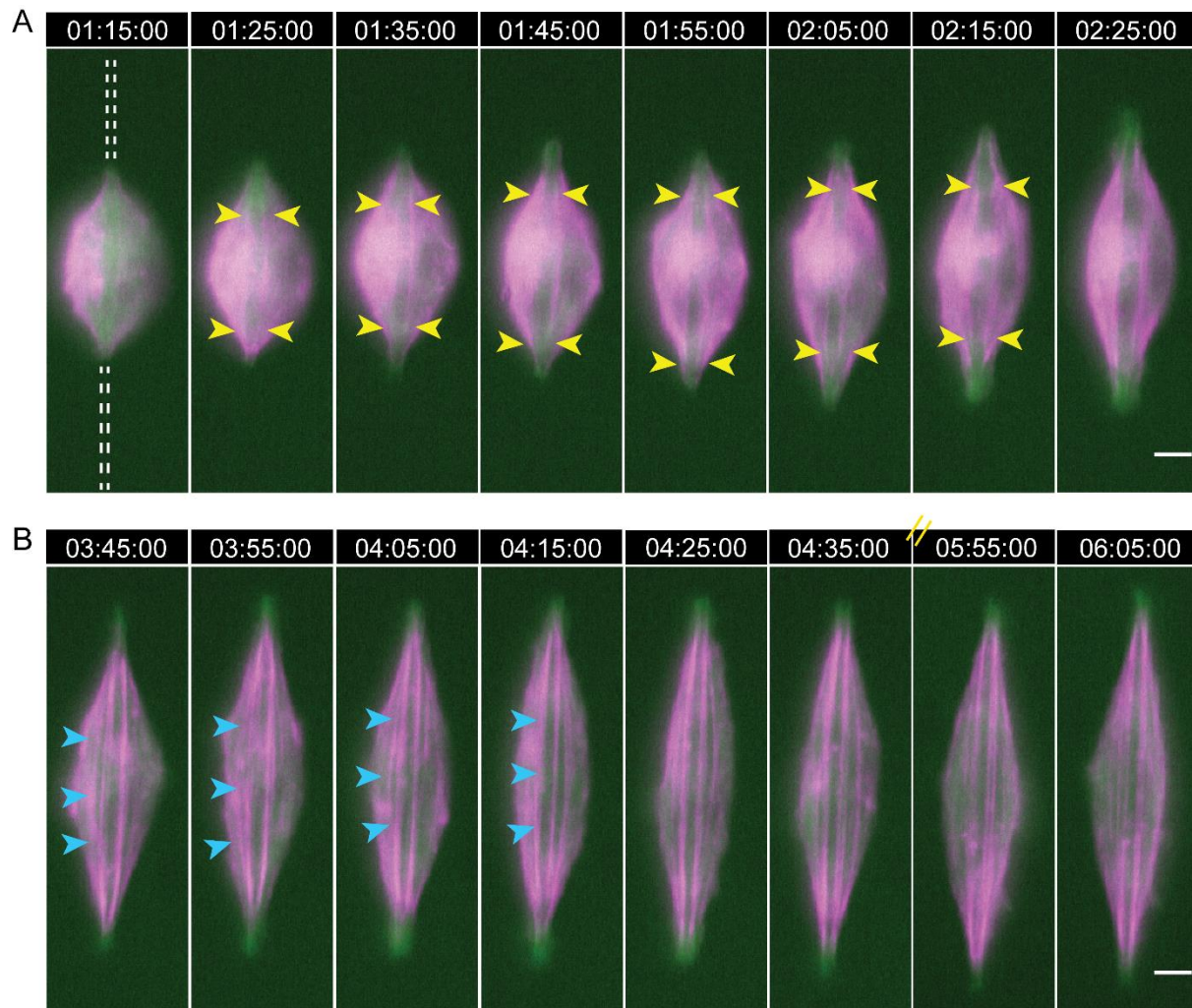
Figure S9. **Cells on 2 μm-wide microline patterns only form ventral SFs only**. (A) Images showing a NT U2OS cell at the early stages of spreading on a 2 μm microline. Magenta: Lifeact, green: paxillin. Dashed white line indicates pattern location. Yellow arrowheads point to two ventral SFs that elongate as the cell spreads along the pattern. (B) Images showing U2OS at later stages of spreading. Blue arrows indicate a ventral SF that flows toward the center of the cell. Time represents HH:MM:SS after initial seeding. Scale bar: 10 μm.
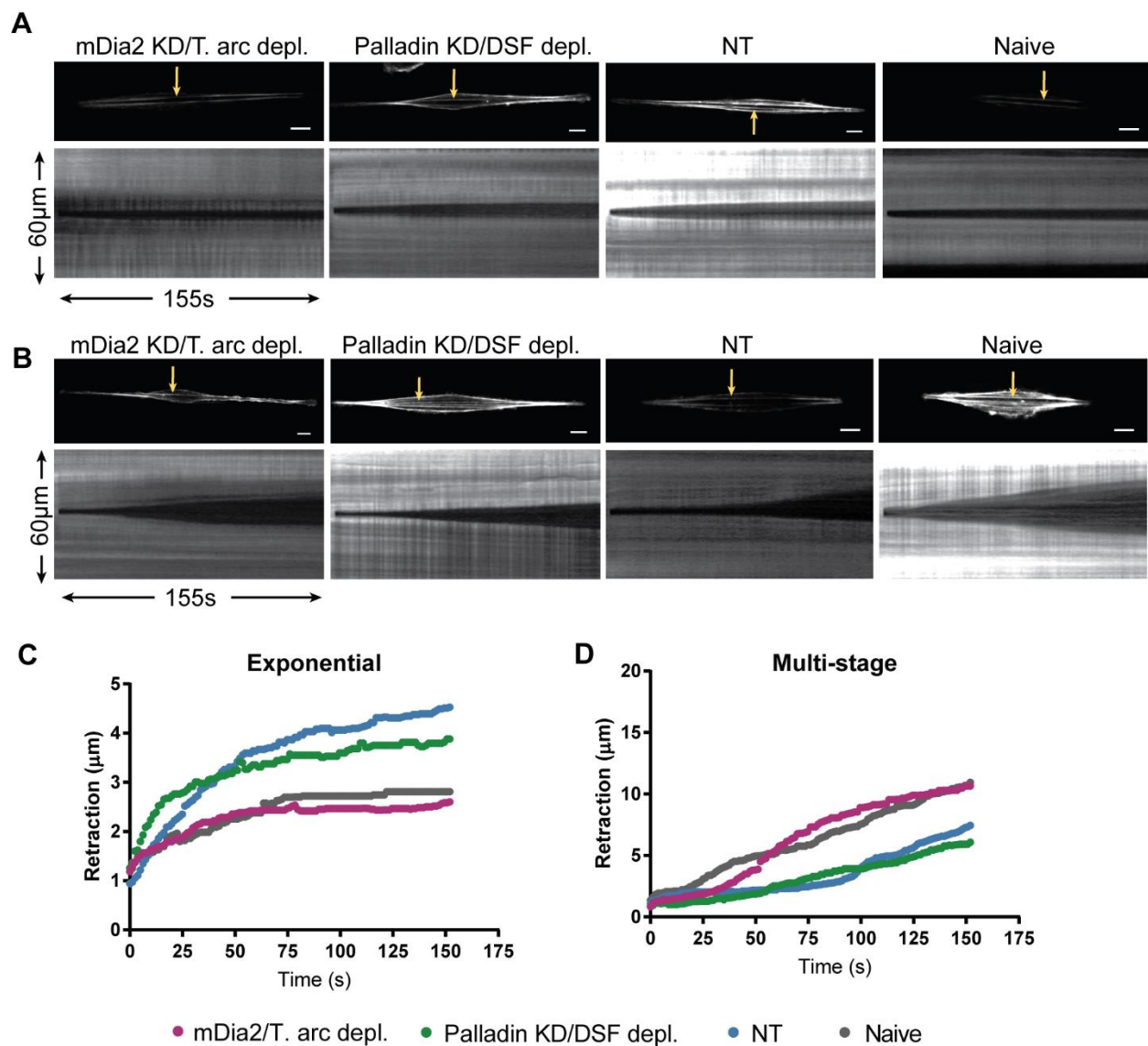
Figure S10. Example images of cells on 2 µm-wide microlines and corresponding kymographs of the ablated SF showing a mixed population of retraction profiles. (A) Representative exponential/KV retractions of ventral SFs in each cell line. (B) Representative multi-stage/non-KV retractions of ventral SFs from each cell line. For (A) and (B), the yellow arrow indicates the ablation site and the kymograph shows the retraction. (C) Measured retraction traces of the indicated fibers from cells in (A). (D) Measured retraction vs. time traces of the indicated fibers from cells in (B). Scale bar: 10 µm.
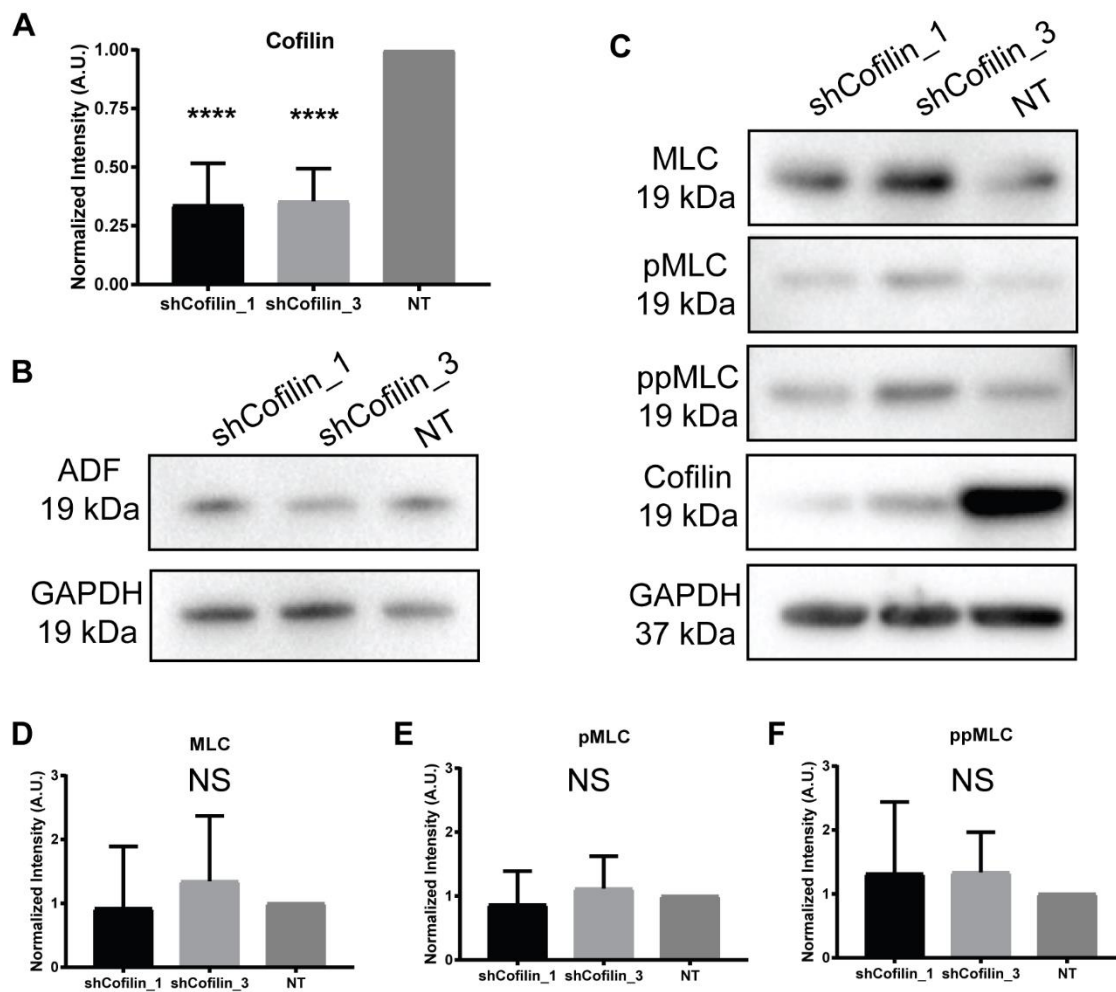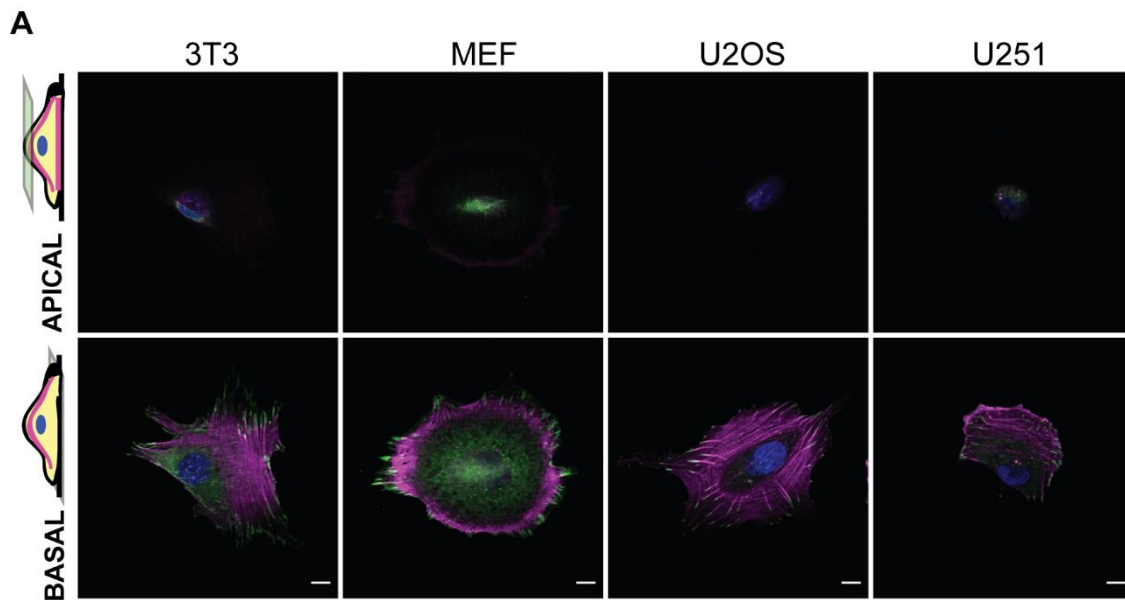
Appendix II. Supplementary Figures for Chapter 3

Figure S1. **Cofilin depletion does not affect ADF or phosphomyosin expression levels.** (A) shCofilin_1 and shCofilin_3 shRNAs reduce cofilin-1 expression by ~70%. Expression levels of cofilin were quantified and normalized to GAPDH loading controls. **** $p < 0.0001$, ANOVA, followed by post-hoc Holm-Sidak test. N = 7 independent experiments. (B) Western blot probing for ADF in cofilin-depleted cells. (C) Western blots probing for MLC, pMLC, ppMLC, cofilin, and loading control GAPDH. Average expression levels of MLC (D), pMLC (E), and ppMLC (F). NS: not significant; ANOVA. N = 6 independent experiments.

Appendix III. Supplementary Figures for Chapter 4

A

| | 3T3 | MEF | U2OS | U251 |

Figure S1. A population of cells in each of the cell lines do not display apical SFs. (A) Representative images of cells not displaying apical SFs. The apical (top row) and basal (bottom row) slices of 3T3, MEF, U2OS, and U251 cells stained for actin (phalloidin, magenta), vinculin (green), and the nucleus (Hoescht or DAPI, blue) are shown. Scale bars: 10 μm.
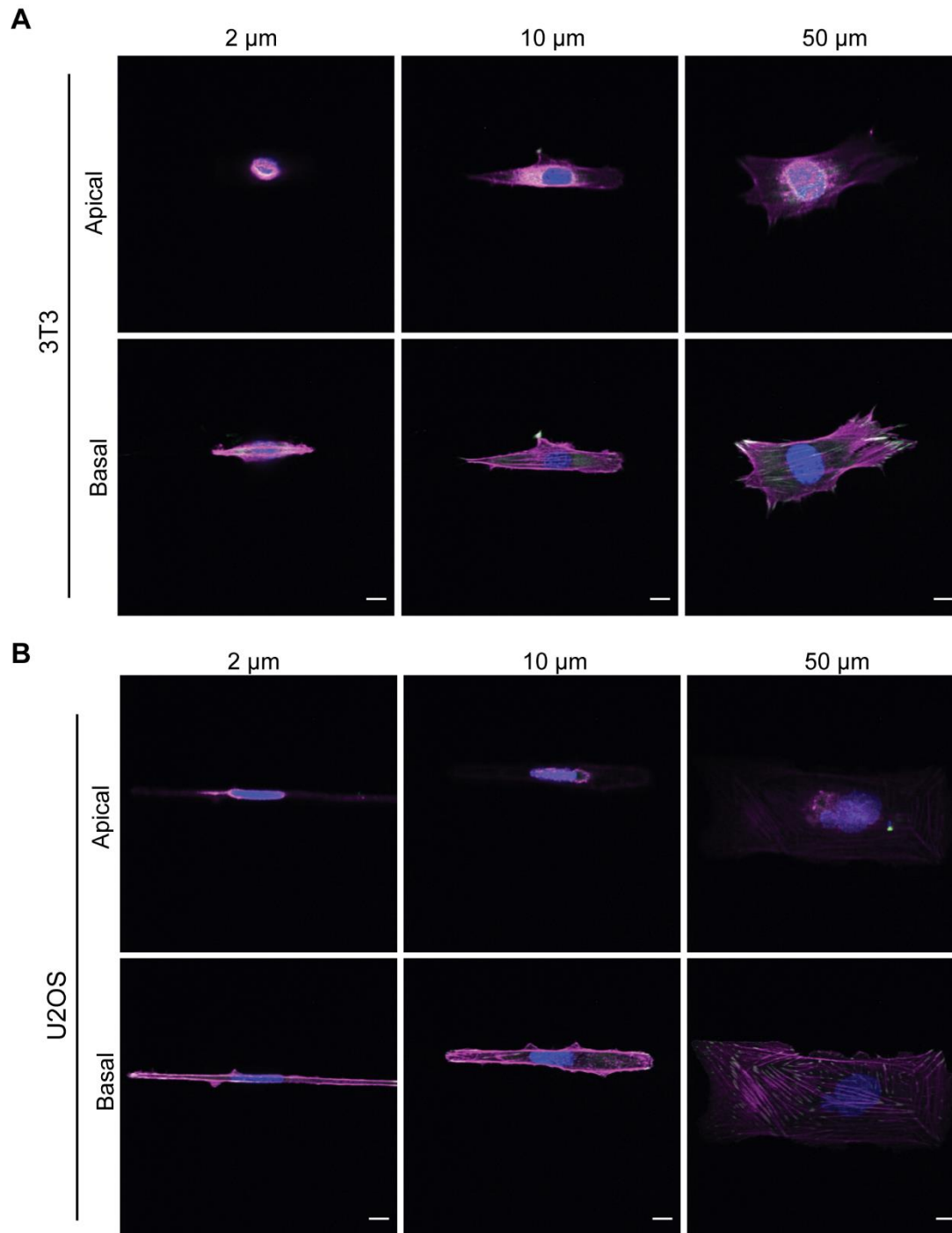
Figure S2. A population of cells in each of the cell lines do not display apical SFs when patterned on 2, 10, and 50 μm-wide fibronectin microlines. (A) Representative images of 3T3 cells not displaying apical SFs. The apical (top row) and basal (bottom row) slices of cells stained for actin (phalloidin, magenta), vinculin (green), and the nucleus (Hoescht, blue) are shown. (B) Representative images of U2OS cells not displaying apical SFs. The apical (top row) and basal (bottom row) slices of cells stained for actin (phalloidin, magenta), vinculin (green), and the nucleus (Hoescht, blue) are shown. Scale bars: 10 μm.